NASA Contractor Report 195374

The Influence of Finite-Size Sources in Acousto-Ultrasonics

Brian N. Pavlakovic and Joseph L. Rose
The Pennsylvania State University
University Park, Pennsylvania

August 1994

Prepared for
Lewis Research Center
Under Contract NAG3–1365

National Aeronautics and
Space Administration

The Pennsylvania State University
Department of Engineering Science and Mechanics

THE INFLUENCE OF FINITE-SIZE SOURCES IN ACOUSTO-ULTRASONICS

A Technical Report
Grant Number NAG3-1365
June 3, 1994

Submitted by

Brian N. Pavlakovic
Joseph L. Rose
Penn State University
114 Hallowel Building
University Park, PA 16802

Submitted to

Director, HITEMP Program
NASA Lewis Research Center
Cleveland, OH 44135

Table of Contents

List of Figures

List of Tables

Chapter 1
Motivation and Methods

Acousto-Ultrasonics (AU) combines acoustic-emission (AE) reception techniques and normal incidence ultrasonic surface loading to determine the distributed damage state in a composite materials (as opposed to macro-defects such as large delaminations or cracks). Although researchers have been able to show that the AU technique can describe the decline in material properties associated with increased porosity or reduced inter-laminar shear strength, the scientific community has not universally welcomed AU because a strong theoretical basis does not yet exist for the method. This technical report addresses this lack. It models the Acousto-Ultrasonic stress waves as Lamb Wave modes so that the effect of the size of the transducer can be studied. This work provides a better physical understanding of the wave propagation principles involved in AU, so that the technique can be used most effectively.

Need

When AU was first used, most analyses relied on empirical results that neglected frequency and guided wave effects. The results were not extremely conclusive because the mechanics of the chosen features were not well understood. Stress Wave Factors (SWF's) were developed to try to quantify the material attenuation, assuming that the internal damage increases the attenuation. Many different time-domain SWF's have been used, for example the counts above threshold (Vary, 1978), average time to arrival (Kautz, 1990), the integrated time-domain signal after passing the signal through a filter (Kautz,

1985), the signal amplitude (Das, 1993), or the integrated square of the time-domain signal (Das, 1993).

Currently, most researchers base their SWF's on the frequency (or power) domain of the signal. Some of the common SWF's in this class are the area under the power spectrum (Reis, 1993), the first moment of the power spectrum, the center frequency (Horne and Duke, 1993), pattern recognition routines (Thomsen and Lund, 1990, Barton, 1993, Hinton, 1993) or the area under the power spectrum within certain frequency bounds (Kautz, 1990). By basing their SWF's in the frequency-domain, these researchers are able to approximate the amount of energy contained in the signal, just as was done in the time-domain. In addition, the behavior of the different frequency components can be compared.

To gain more insight into the differences between the frequency components and create wavestructures that are more sensitive and accurate, many researchers are treating the stress waves as Lamb Waves (Tang, 1988, Alleyne 1991, 1992, Ditri 1993b, 1992, Rose 1993, Costley and Berthelot, 1993). Generating specific modes provides a much stronger theoretical basis. However, the physical understanding of AU's unique wave propagation characteristics is still far from complete. In addition to the inhomogeneous nature of composite materials, normally incident transducers are a limiting wave propagation case that has not yet been fully explored.

Little work has been done on the generation of waves by finite-sized transducers. Viktorov (1967), Pursey (1957), Fulton and Sneddon (1958), and Nikiforov and Kharitonov (1981) began work in this area. Most recently Ditri et al. (1993) and Rose et al. (1993a) have continued this work. However, most of the work to date has concentrated on the "wedge" technique, which can allows the angle of incidence to be adjusted so the phase of the desired mode can be matched. Very little work has been done that studies the finite source influence

on the generation of Lamb waves at normal incidence. Rose et al. (1993a) qualitatively showed a frequency shift that is associated with changing the transducer's size in composite layers. Ditri et al. (1993) derived the time-harmonic solutions due to axisymmetric normal surface loading (which models AU).

Although the currently used SWF's work well for determining porosity or microstructure cracking, they can only compare samples to a known set, and they cannot separate the effects of different types of defects or the effects associated with the experimental setup such as the couplant, the contact pressure, or transducer parameters. This incomplete physical understanding restricts the researchers' ability to apply results from one specimen and one transducer to another. Studying the influence of the source can significantly narrow the gap between experiment and theory. It will also help determine which modes and frequencies can be used most effectively to detect certain types of damage.

Goals and Elements of This Report

The goal of this thesis is to gain a better physical understanding of the wave propagation principles used in Acousto-Ultrasonic non-destructive evaluation. By enhancing the physical basis and understanding of AU, inherent limitations can be recognized and adjustments can be made to compensate for these limitations or even take advantage of them. This will help researchers develop sophisticated defect analysis methodologies and allow AU to become a very powerful method of NDE.

This work builds upon recent investigations of frequency effects and the time-harmonic wave solutions by closely examining the influence that the source and the plate thickness have on transient loadings of an isotropic layer. It

concentrates on the generation of guided waves via transient normal axisymmetric surface loading.

A FORTRAN program was created that generalizes the time-harmonic solutions to simulate realistic transient solutions. Using this program and experimental results, the following questions were addressed:

- How does the size of the transducer affects mode generation
- How does a finite source modify the frequency-thickness normalization
- How does the pressure distribution and shape of the wavepacket affect mode generation

Physical interpretations and practical guidelines for the generation of guided waves using Acousto-Ultrasonics are given for each of these areas.

Methodology

In order to find the wave propagation principles that control the effect of the transducers size, three methods are used. These methods include discussion of the time harmonic solutions proposed by Ditri et al., computer modeling via linear superposition of the time harmonic solutions, experimental data, and a general discussion of the physical concepts involved.

Time Harmonic Solutions

Ditri et al. propose the guided isotropic plate wave solutions due to loading by an axisymmetric normal surface load, which models the AU technique. Although the solutions are derived for an isotropic plate, which allows the stress waves to be considered as Lamb Waves, the general principles derived from them will also apply to anisotropic plates (and composite plates) as long as only one direction is considered. Previous work has shown that this a valid conclusion because composite structures can support waves that behave in the same manner

as Lamb waves propagating in isotropic materials (Tang and Henneke, 1988, Kautz, 1993).

The time-harmonic solutions that are derived take into account the size of the transducer (as well as the pressure distribution) for the limiting case of normally incident waves. The mathematics of the solution helps build an understanding of the underlying physical principles.

The rest of this section summarizes the derivation of the time-harmonic solutions that were developed by Ditri (1993a) and that form the basis for this study. A complete derivation of the solution can be found in Appendix A.

The problem of normal incidence pressure loading of a linearly elastic, homogeneous, isotropic layer is investigated for the coordinate axes that are shown in figure 1.1. From the theory of elasticity, it can be determined that the displacement field, $\mathbf{u}(\mathbf{r},t)$, will satisfy Navier's equation of motion,

$$\mu\nabla^2\mathbf{u} + (\lambda + 2\mu)\nabla\nabla\cdot\mathbf{u} = \rho\frac{\partial^2\mathbf{u}}{\partial t^2} \tag{1.1}$$

for all $\mathbf{r}$ interior to the layer (where ρ is the mass density of the material and λ and μ are its Lamé constants).

The AU technique uses normal incidence longitudinal wave transducers, which tend to apply only normal tractions to the surface of the plate because shear stresses cannot be effectively transmitted across the oil film that couples the transducer to the plate. To model this situation, the following boundary conditions are used,

$$\begin{aligned}
&\sigma_{zz}(r,z=d/2,t) = \begin{cases} f(r)e^{-i\omega t} & 0<r<a \\ 0 & r>a \end{cases} \\
&\sigma_{zz}(r,z=-d/2,t) \equiv 0 \\
&\sigma_{rz}(r,z=d/2,t) = \begin{cases} g(r)e^{-i\omega t} & 0<r<a \\ 0 & r>a \end{cases} \\
&\sigma_{rz}(r,z=-d/2,t) \equiv 0
\end{aligned} \tag{1.2a-d}$$

where $f(r)$ and $g(r)$ are the normal and transverse traction distributions applied to the surface of the plate. As indicated by equations (1.2), the surface loading is assumed to be time-harmonic and axisymmetric, applied over a circular region of radius a.

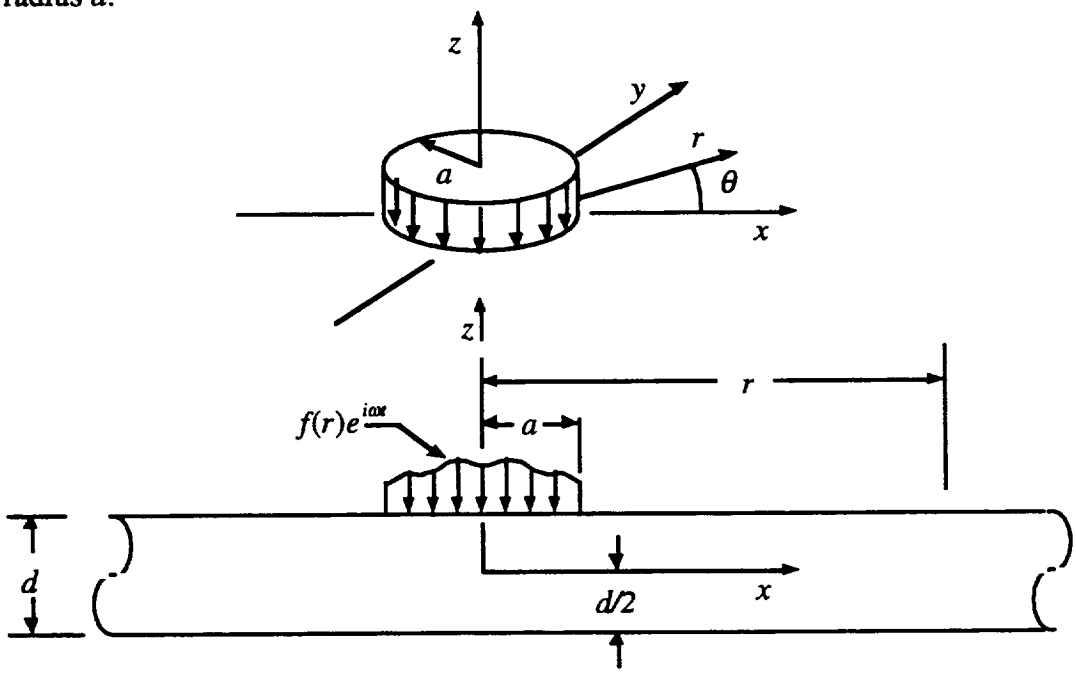

Figure 1.1 The upper surface of a layer is subjected to a time-harmonic axisymmetric normal traction loading in the circular region $r \equiv \sqrt{x^2 + y^2} < a$

The displacement field is uncoupled into irrotational and equivoluminal parts using the Helmholtz decomposition. The Hankel transform is then applied and the boundary conditions are satisfied. After solving for the unknown amplitudes in the general solution, the inverse Hankel transform is applied, using residue calculus to evaluate the resulting integrals. This procedure yields the

following results for the symmetrical (s) and anti-symmetrical (a) components of the in-plane (r) and out-of-plane (z) particle displacements, $u_{r,z}^{s,a}$:

$$u_r^{s,a}(r,z) = i\frac{\pi}{2\mu}\sum_{\xi_{s,a}} F^0(\xi_{s,a},a)\xi_{s,a}\frac{\Gamma_m^s(\xi_{s,a})}{\Delta'_{s,a}(\xi_{s,a})}H_1^{(1)}(\xi_{s,a}r) \qquad r>a \qquad (1.3a)$$

$$u_z^{s,a}(r,z) = i\frac{\pi}{2\mu}\sum_{\xi_{s,a}} F^0(\xi_{s,a},a)\xi_{s,a}\frac{\Gamma_m^s(\xi_{s,a})}{\Delta'_{s,a}(\xi_{s,a})}H_0^{(1)}(\xi_{s,a}r) \qquad r>a \qquad (1.3b)$$

where the solution is summed over $\xi_{s,a}$, the wavenumber roots of the symmetric and anti-symmetric dispersion equations, $\Delta_{s,a}$. $\Delta'_{s,a}$ represents the derivative with respect to wavenumber of these dispersion equations. F^0 is the zero order Hankel transform of the normal pressure distribution, $f(r)$, and $H_n^{(1)}$ is the Hankel function of the first kind of order n. The $\Gamma_{an}^{s,a}$ terms are defined in Appendix B. A description of the significance of each of these terms is given below.

The summation sign in the problem solution indicates that every propagating mode contributes to the solution. For a given circular frequency, ω, the function is evaluated at all of the roots of the symmetric and anti-symmetric Rayleigh-Lamb dispersion equations, which correspond to the wavenumbers at which each mode propagates. This result follows directly from the residue calculus used to solve the problem. The denominator of the solution (before the residue calculus is used to evaluate the integral) is either the symmetric or anti-symmetric dispersion equation, for $u_{r,z}^s$ and $u_{r,z}^a$ respectively. So the poles of the solution coincide with the roots of dispersion equation. Later, the solution will be generalized so that a range of frequencies (as opposed to a single frequency) is excited. In this case, the summation over the modes becomes integration over the dispersion curves.

The source term, F^0, is the Hankel transform of the normal pressure distribution $f(r)$, defined in the boundary conditions. This term accounts for the interference effects across the face of a finite source. For a point source (which

does not experience this type of interference) the Hankel transform has a constant value with respect to the transform variable, ξ, which is also the wavenumber. Exciting every wavenumber equally means that every frequency and phase velocity are also excited equally since $\xi = \omega / v_{ph}$ for a planar wavefront. For a finite source, the value of the Hankel transform of the pressure distribution will fluctuate at high wavenumbers (low phase velocities), and approach a maximum value ($-0.5Pa^2$ for the piston case) as the wavenumber goes to zero (and the phase velocity goes to infinity). Ditri (1993a) showed that the solution may be generalized to include the Hankel transform of any axisymmetric time-harmonic pressure distribution.

The material response term, $\Gamma^{s,a}_{\alpha\beta} / \Delta'_{s,a}$, is a function of the material properties (bulk longitudinal and shear wave velocities), the wavenumber and the frequency-thickness product. It represents what wavestructures the plate can support and still satisfy the zero traction boundary conditions. If the material response term includes the wavenumber term that appears immediately before it, it represents the system's response to a point source, which decays to zero as the phase velocity approaches infinity. However, this wavenumber term has been pulled out so that the material response is dependent on the frequency-thickness product instead of being dependent on the frequency and thickness independently. By separating the wavenumber in this manner, the finite-size effects are separated and the material response better indicates the modes' behavior at infinite phase velocities (tending to be infinitely excitable or unexcitable). Expressions for gamma and delta can be found in Appendix B.

The wavenumber that has been pulled out from the material response term is first introduced to the solution by the Hankel transform to account for its cylindrical nature. Although the Hankel transform operates on only one variable, r, it is actually a two dimensional transform. The implied integration over the

angle, θ, leads to a constant value times r since the function is assumed to be axially symmetric, not varying with θ. Physically, this phenomenon can be related to the dissipation of energy as a wave packet moves away from the source and spreads over a greater region. At times in this thesis, the wavenumber term is included in the source term because the energy considerations can be related to the finite nature of the source. Including the wavenumber as a part of the source term concentrates all of these finite-size source effects in the source term and allows the material response to be independent of the frequency (and dependent on the frequency-thickness product instead). However, the material response term may also be multiplied by the wavenumber term, so that the material response term reflects the response of the system to a point source.

The radial term, $H_0^{(1)}(\xi_{s,a}r)$ or $H_1^{(1)}(\xi_{s,a}r)$, describes how the wave behaves as the distance from the source increases. The distance between consecutive local maxima (the radial "wavelength") decreases as the separation from the source increases, which will affect the group velocity and interference effects. In the large radius limit, however, the Hankel function behaves more traditionally, fluctuating with a near constant wavelength.

$$H_p^{(1)}(x) \approx \sqrt{\frac{2}{\pi x}} \exp\left(+i\left(x - \frac{\pi}{4} - p\frac{\pi}{2} \right) \right) \qquad (1.4)$$

$$x >> 1$$

In this limit, the expression relating the wavenumber to the frequency and phase velocity approaches what it would be for a planar wavefront ($\xi = \omega / v_{ph}$).

Computer Model

The solution technique explained above assumes a time-harmonic source (continuous wave). However, before it can be applied to realistic circumstances, the solution needs to be expanded to include transient sources. In order to do this,

the solution needs to account for the excitation of waves over a portion of the frequency spectrum, as opposed to excitation at one specific frequency.

The various components of the frequency spectrum are combined by simple linear superposition. In practice, the complex Fourier transform of the source is used as a weighting function (replacing the constant pressure amplitude function P with $p(\omega)$). The complex transform is used so that the phasing information of each of the frequency components can be conserved. Because the governing equation is a hyperbolic differential equation, causality is "built in" and does not need to be explicitly added. The superposition of sources suffices.

From the frequency spectrum, the time domain signal can be generated by two techniques. The first method, the harmonic summation method, multiplies each term by $e^{-i\omega t}$, integrates over the dispersion curves in the region of interest, and then repeats the process after incrementing the time. The solution may also be obtained by taking the inverse Fourier transform of the complex frequency response of the system. The inverse FFT technique is much faster and yields identical results. However, the harmonic summation method must still be used to obtain a cross sectional profile (through the plate thickness), since, by definition, the inverse Fourier transform transforms a frequency spectrum to the time domain. The inverse transforms are unique as long as the functions are continuous, as they are in this case.

A FORTRAN program was created to implement this transient solution. The program was created to run under VS FORTRAN in Penn State's VM environment. Its code is approximately 1500 lines long, and it takes anywhere from five seconds to twenty five minutes to run, depending on the task and the present load on the system. The data files were downloaded to a Quadra 900 and graphed using Microsoft Excel. The computerized solution allows each of the factors which affect the wave propagation to be studied separately. It also takes

into account the changes in phase velocity and excitability that occur because a portion of the frequency spectrum, and not a single frequency, is excited.

Experimental Testing

Experimental results are used to confirm the analytical ones. For comparison, three different size Gamma transducer pairs (6.35 mm, 12.7 mm, and 25.4 mm) from Krautkramer-Branson and a tone burst generator setup (HP3441A and HP8166 Function Generators, MATEC 350 Amplifier, and a LECROY 9310 digital oscilloscope) are used.

The experimental setup can be seen in figure 1.2. A Hewlett Packard 3314 function generator created a continuous wave at the desired center frequency. This signal lead to a Hewlett Packard 8116A function generator which modulated the signal so that each burst contained 20 cycles. This modulated tone-burst technique allows the center frequency of the pulse to be controlled regardless of the frequency characteristics of the individual transducers. A MATEC model 350 tone burst amplifier was coupled to an attenuator to increase the signal voltage to 20 volts. The amplification was linear for all signals whose center frequency was between one and ten megahertz for a pulse repetition setting of 10 ms, as witnessed by propagating the wave through a PMMA delay block. The matched transmitting and receiving transducers were coupled to the aluminum plates using Krautkramer Branson Ultrasonic Couplant. Surface tension between the transducer and the couplant was used to hold the transducers on the plate, so that shear tractions would not be induced on the plate. The signal was analyzed by a LECROY 9310 digital oscilloscope with a 2 ns accuracy. Two thousand points were sampled at 50 ns intervals (100 μs total) and transferred to a NCR computer that was running Lab Windows, where standard IMSL routines were used to find the frequency spectrum of the signal. All of the graphing was done using Microsoft Excel on a Macintosh Quadra 900.

These test methods are used to evaluate the effect that the transducer's size has on AU wave propagation which is described in the rest of this report.

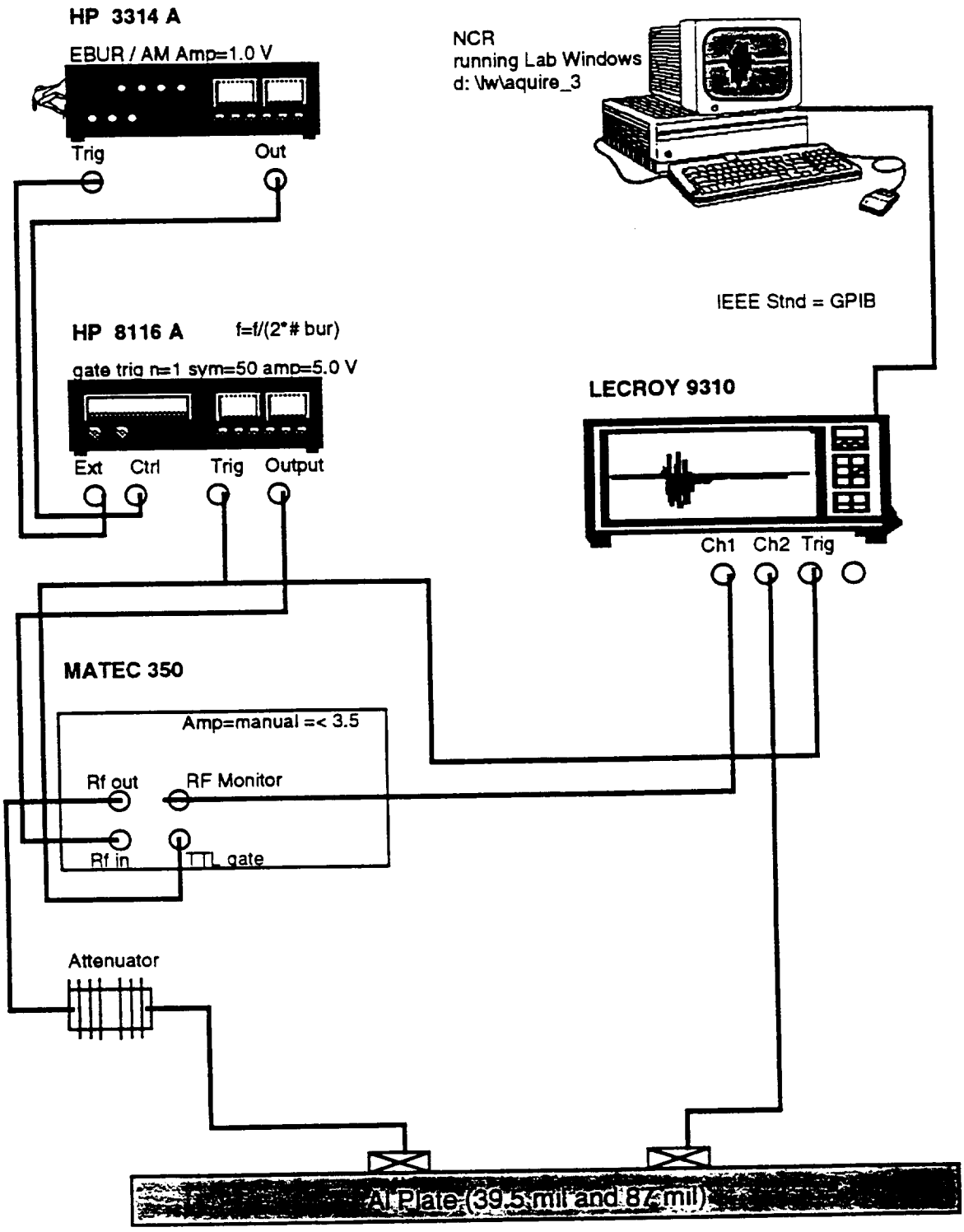

Figure 1.2 The experimental configuaration used to create tone burst signals. This set-up allows the center frequency of the source to be controlled so optimum frequencies can be chosen.

Chapter 2
General Considerations in Acousto-Ultrasonic Wave Propagation

This chapter addresses some general principles that will be used in the rest of this thesis. It begins by explaining the concept of excitabilities and how they are related to the wavestructure. The pressure distribution across the face of the transducer and the effect of the pulse shape are also discussed.

Excitabilities and Cross Sectional Profiles

In plates, waves can only propagate at certain frequency-phase velocity combinations that correspond to the roots of the Rayleigh-Lamb dispersion equations. Where these roots would fall for an aluminum plate is shown in figure 2.1. Each of these roots has a certain excitability associated with it that represents how easily that mode can be generated. This excitability is related to the wavestructure of that root (point on the dispersion curve) and is generally defined as the ratio of the normal component of the particle velocity on the surface of the plate to the total power carried by the mode. The out-of-plane and in-plane particle velocity components change for each of the points on the dispersion curve, causing certain points to be more excitable than others.

Near the Cutoff Frequencies

In AU, the mode's excitability at its cutoff frequency is extremely important. The cutoff frequency corresponds to the frequency at which the mode's wavenumber is zero and the frequency below which a mode is evanescent. (Table 2.1 lists the theoretical values of the cutoff frequencies for an aluminum plate.) Since the wavenumber is zero at these points, the phase velocity is infinite. Consequently, AU will tend to generate modes at these frequencies, since

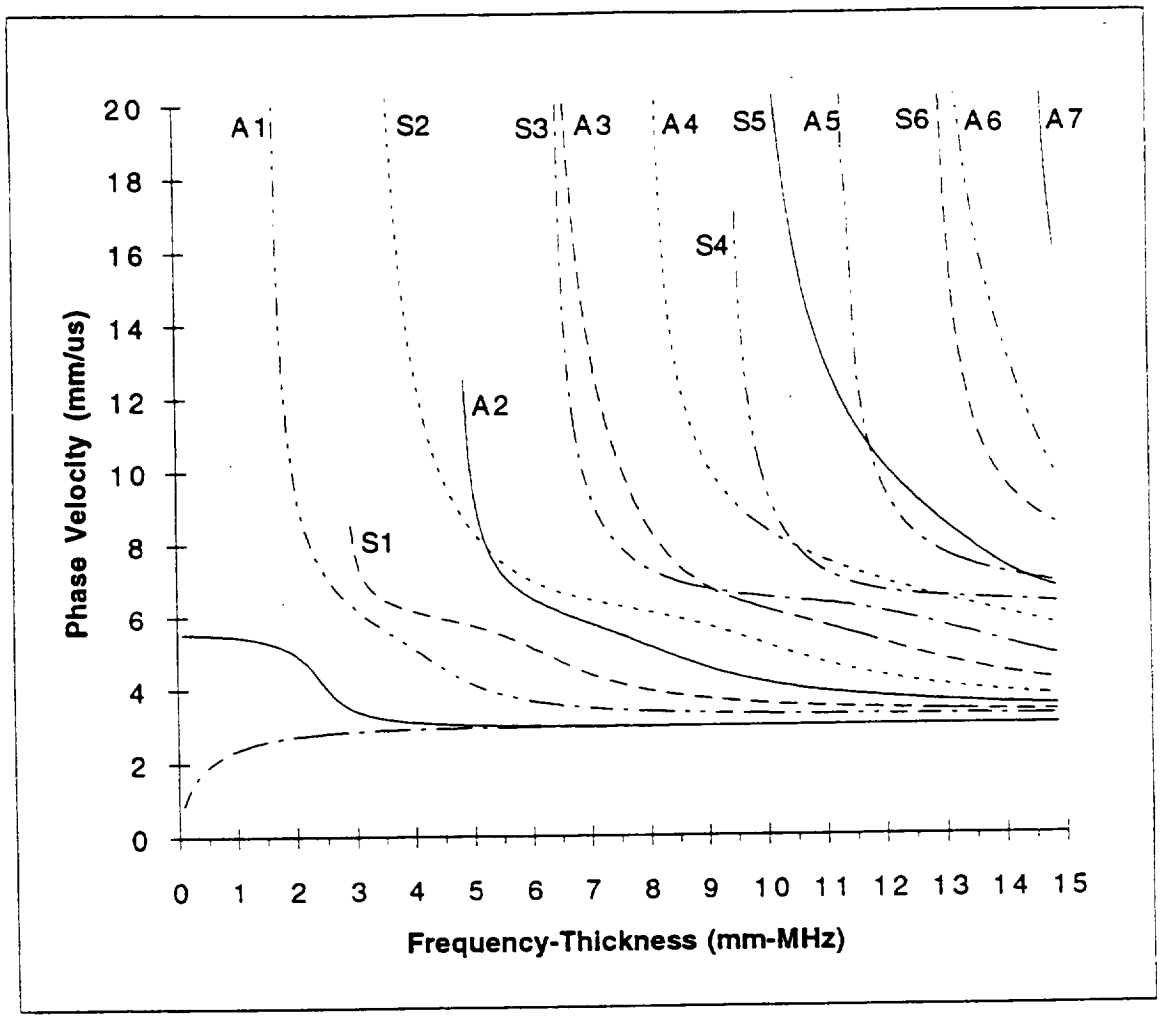

Figure 2.1 Dispersion curves for a traction free plate, whose bulk wave speeds are Vl = 6.3 mm/us and Vt = 3.2 mm/us (aluminum). Only real roots are shown, which accounts for the apparent ends of modes S1, A2, and S4.

Table 2.1 Cutoff Frequencies for a one mm thick traction free plate, whose bulk wave speeds are Vl = 6.3 mm/us and Vt = 3.2 mm/us (aluminum).

Order	*Symmetric Modes*	*Antisymmetric Modes*
First (1)	3.15	1.6
Second (2)	3.2	4.8
Third (3)	6.4	6.3
Fourth (4)	9.45	8
Fifth (5)	9.6	11.2
Sixth (6)	12.8	12.6

normally incident waves tend to generate plate waves with very high phase velocities. This is the limiting case of the "wedge" technique, which generally allows the experimenter to vary the angle of incidence so that the ultrasonic wavefront travels down the surface of the plate and preferentially excites a plate wave with a phase velocity that matches the wavefront's delay.

As the mode approaches its cutoff frequency, the particle velocities will become either entirely out-of-plane or entirely in-plane. (Auld 1990, p.84., Vitkorov 1969) As a result, the modes that have entirely out-of-plane particle velocities at their cutoff frequency become infinitely excitable, and the modes with only in-plane particle velocities become completely unexcitable.

The excitabilites cannot be directly derived from the time-harmonic solutions presented in this thesis. However, the material response term contains similar information, combining information about both the excitabilities and the wavestructure. This term is shown in figure 2.2, a plot of the out-of-plane displacement component of the material response as function of the frequency-thickness product and the phase velocity ($=\omega/\xi$, assuming the point of observation is far away from the source). The response of the second order symmetric mode (S2) and the third and fifth order anti-symmetric modes (A3 and A5) are increasing with the phase velocity, indicating that these modes are very excitable at high velocities. On the other hand, the responses of the third order symmetric (S3) and the fourth order anti-symmetric mode (A4) are quickly decreasing. As a result, the high phase velocities associated with a normally incident wave packet will not tend to excite these modes. In this manner, figure 2.2 can be used to indicate which modes can be efficiently generated using AU techniques.

When multiplied by the wavenumber, the material response term tells what particle displacements would be excited by a point source (that tends to excite all frequencies and phase velocities equally), as shown in figure 2.3. The

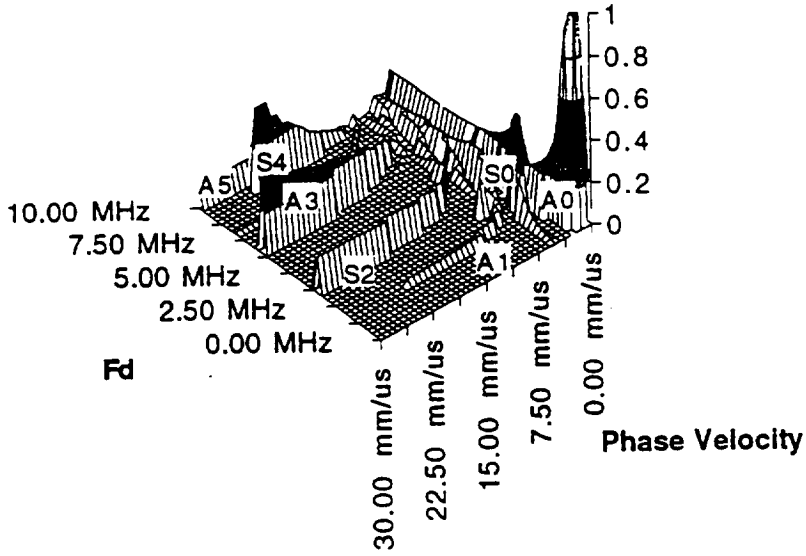

Figure 2.2 Out-of-plane displacement component of the material response as a function of the frequency-thickness product and the phase velocity. The responses of modes S2, A3, and A6 are increasing with the phase velocity, indicating that these modes are very excitable at high velocities. On the other hand, the material responses of modes S3 and A4 quickly decrease and the modes will therefore not be effectively excited by normal tractions.

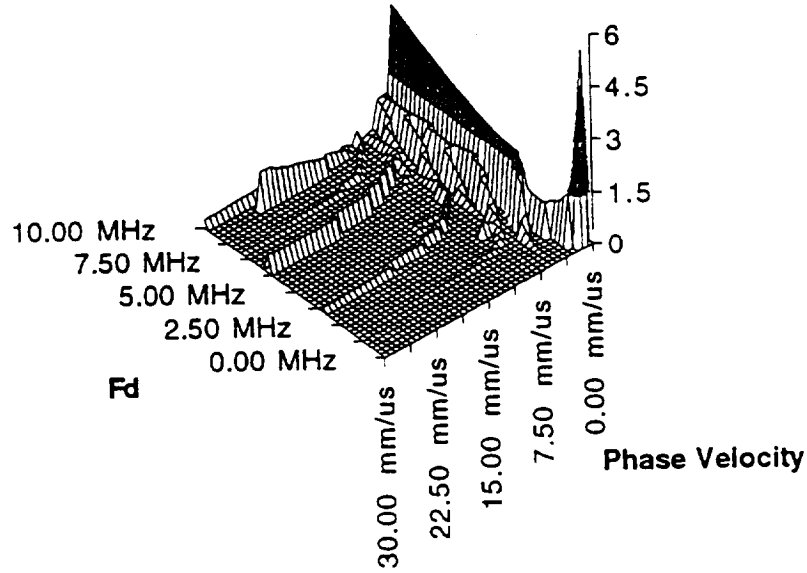

Figure 2.3 Out-of-plane displacement response to a point source, shown as a function of the frequency-thickness product and the phase velocity. Numerically, the response represents the material response term multiplied by the wavenumber. It decays to zero at infinite phase velocity, since a point source cannot generate an infinite amount of energy.

response to a point source decays for all modes as the phase velocity approaches infinity, indicating that the system contains a finite amount of energy. As for the material response term, it can be observed that modes S2, A3, S4, and A5 will be more strongly excited than modes A1, S1, A2, and S3 at high phase velocities.

Cross-Sectional Profile

The wavestructure relates to both how excitable a mode is and how sensitive it is to certain defects. The cross sectional profile of the out-of-plane normal stress, the out-of-plane displacement and the in-plane displacement, which are characteristics of the wavestructure, are shown in figure 2.4. The solid lines represent the symmetric modes and the dashed lines represent the anti-symmetric modes. There are large out-of-plane displacements on the surface of the plate when the frequency-thickness product (fd) is both 3.4 mm-MHz (where S2 dominates) and 6.4 mm-MHz (where A3 dominates). As a result, these modes can be efficiently generated by a normal traction. On the other hand, the 5.0 mm-MHz frequency-thickness products plots (figures 2.4b,e,h) are dominated by the A2 mode which is transverse (all in-plane displacements) at its cutoff frequency (at fd=4.8 mm-MHz). Although the in-plane displacements are not very large, the out-of-plane displacements are almost zero making the mode very difficult to excite via normal traction.

The differences in wavestructure can be exploited for defect detection and characterization. For example, the second order symmetric mode (S2) at fd=3.4 mm-MHz has a large in-plane displacement near the plate's surface allowing it to find critical surface cracks effectively, in addition to having a large out-of-plane displacement component. The A3 mode at 6.4 mm-MHz, on the other hand, has a maximum in-plane displacement approximately one third of the way through the plate and has a very small in-plane displacement on the surface. Since the A3

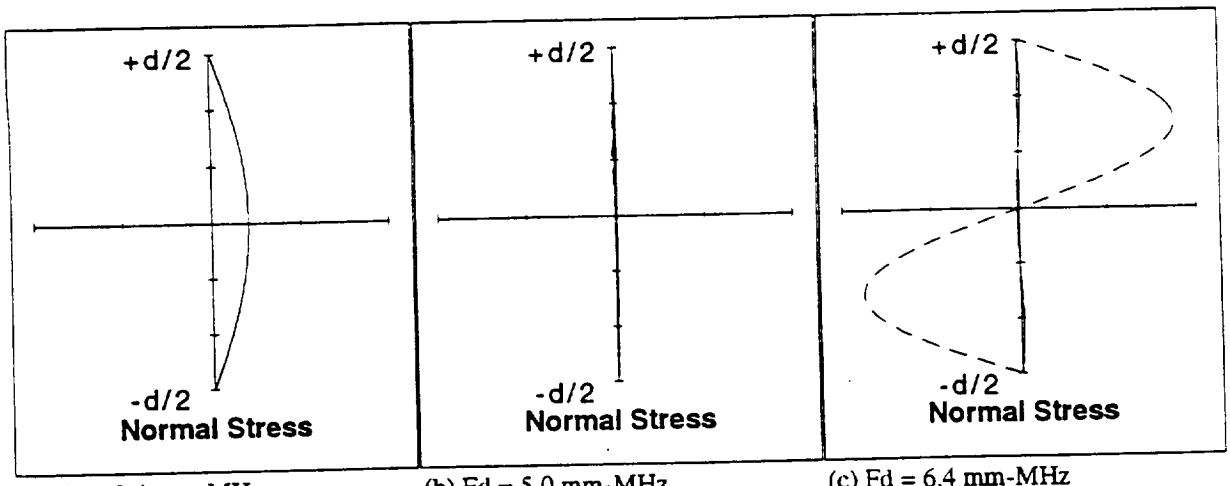

(a) Fd = 3.4 mm-MHz (b) Fd = 5.0 mm-MHz (c) Fd = 6.4 mm-MHz

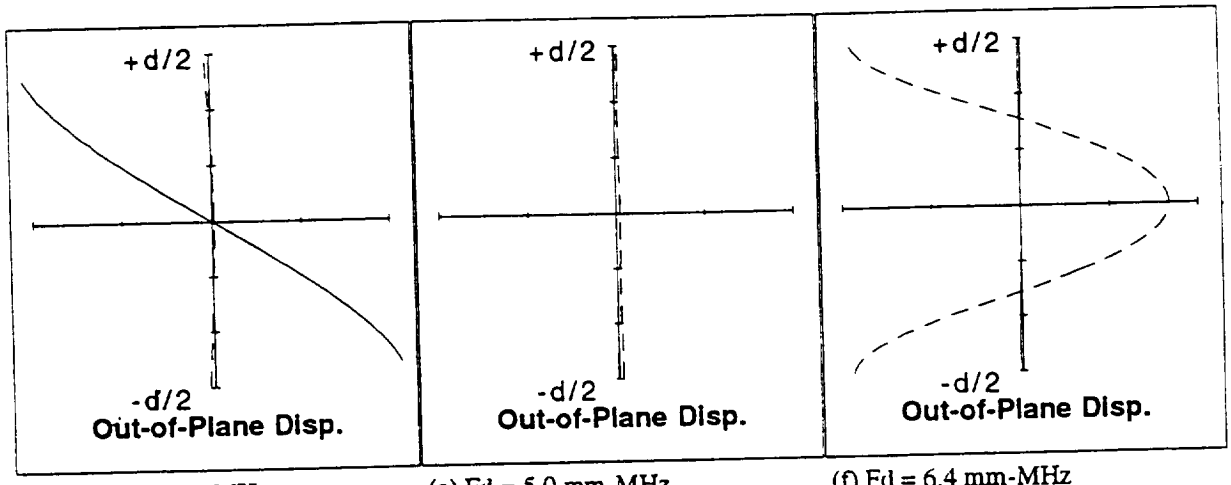

(d) Fd = 3.4 mm-MHz (e) Fd = 5.0 mm-MHz (f) Fd = 6.4 mm-MHz

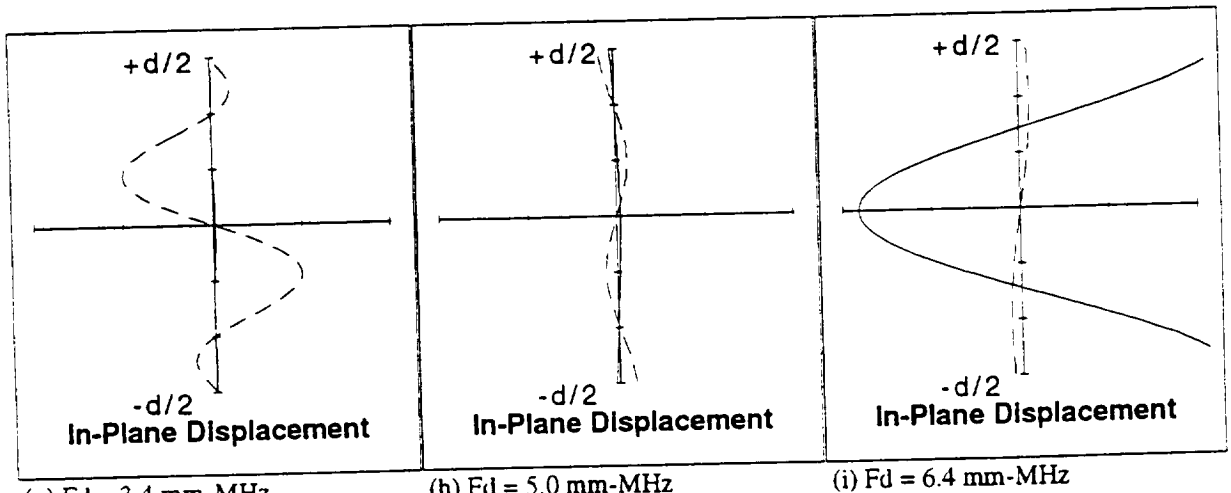

(g) Fd = 3.4 mm-MHz (h) Fd = 5.0 mm-MHz (i) Fd = 6.4 mm-MHz

Figure 2.4 Out-of-plane normal stress, out-of-plane displacement, and in-plane displacement as a function of depth for three different frequency-thickness products. The solid lines represent symmetric modes and the dashed lines represent antisymmetric modes. Differences in wavestructure determine how excitable a certain mode is and how sensitive it will be to certain types of defects.

mode's maximum in-plane displacement occurs at a location where the S2 mode has no in-plane displacement, the difference in the propagation characteristics of the two modes can be exploited to help characterize defects such as cracks or pores.

Effect of the Varying the Pressure Distribution

When angle beam transducers are used, the experimenter can effectively control which area of the dispersion curves are generated by controlling the transducer's center frequency, the frequency bandwidth, and the angle of incidence. However, in Acousto-Ultrasonics, all of the experiments are conducted at normal incidence, which limits the control that the experimenter has over which modes are generated. To regain some of this control, other characteristics of the transducer, such as its pressure distribution, must be adjusted.

The pressure distribution is affected by many factors, including the electrical contacts, the pulse shape, the backing material, the type of piezo-electric, and the physical shape of the housing and the transducer construction. Although many of these parameters cannot be changed after the transducer is manufactured, they should be considered when the transducer is designed. Different distributions favor different phase velocities, which may be chosen so that the transducer can excite a particular mode more effectively. Special transducers can also be created that target a specific mode by using discontinuous faces or sequencing. Laser generated ultrasound will allow these special distributions to be easily changed and adapted depending on the desired applications.

Most theoretical studies model a piston-like source since it is the simplest one to describe (being constant below the transducer and zero everywhere else). However, the discontinuities at the edge of the transducer are unrealistic and they

unnecessarily complicate the mathematical results. High-frequency components appear that are not present in continually distributed sources such as the parabolic distribution. Comparing the simulated and experimental results indicates that the parabolic distribution does model the realistic situation more closely.

The Hankel transform technique can be used to model any axisymmetric time-harmonic pressure distribution, although numerical integration may be needed to compute the result for a complicated distribution. For example, a more realistic pressure distribution may be a "mixed" parabolic-piston source, which behaves like a piston source near the center of the transducer, but declines towards the edge as a parabolic source would. This distribution could be represented by the following equation:

$$Press = \begin{cases} 0 & r > a \\ 1 - \left(\frac{r-b}{r-a}\right)^2 & a > r > b \\ 1 & r < b \end{cases}$$

where a is the radius of the transducer and b is the transition point (for example 2/3 of a).

Pulse Shape Influences

One of the easiest ways to control the frequency spectrum of the source is modifying the shape of the wave packet (including its frequency, duration, and modulation). In both the experimental set-up and the simulation, "tone burst" techniques were used, in which 20 cycle packets of a certain frequency are square or sine-modulated. The experimental set-up that was used for all of the experiments is shown in figure 2.5. This set-up allows the center frequency of the transducer to be controlled, although the transducer will retain some of its frequency characteristics and generate frequencies near its natural frequency more strongly than other frequencies.

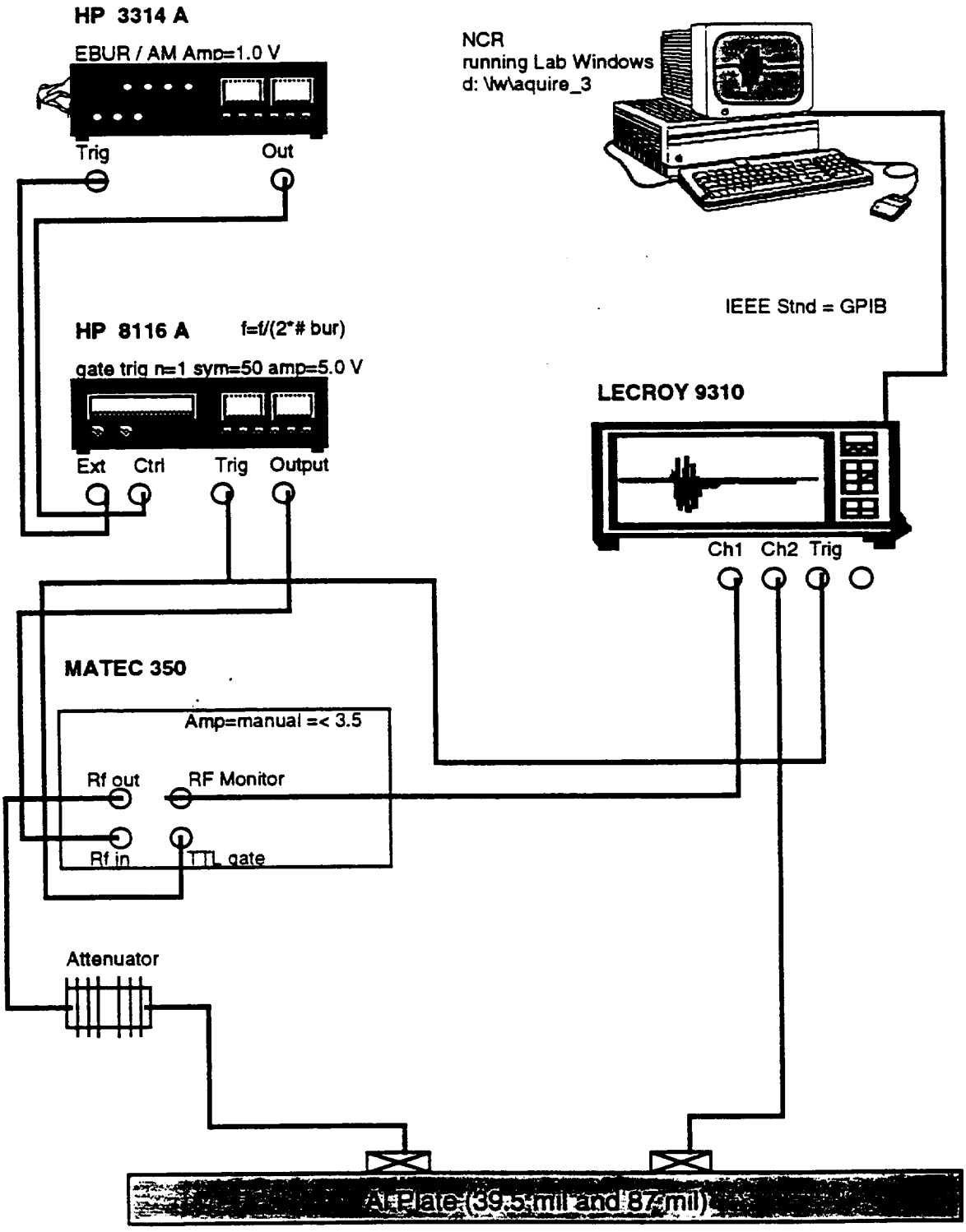

Figure 2.5 The experimental configuaration used to create tone burst signals. This set-up allows the center frequency of the source to be controlled so optimum frequencies can be chosen.

The number of cycles in the pulse greatly affects the frequency bandwidth, which in turn affects the ability to excite a mode. Figure 2.6 shows the experimental waveform for signals of 10 and 80 cycles. Figure 2.7 shows the frequency spectrums of these signals. The frequency peaks are much narrower for the 80 cycle pulse, since the extra cycles reduce the frequency bandwidth of the source. This causes modes to only be excited when the center frequency is very close to the mode's cutoff frequencies. The 10 cycle pulse, on the other hand, excites each mode over a broader frequency range. It is also able to excite more modes (for example A1 at fd=1.6 mm-MHz), since its frequency bandwidth is larger. Figure 2.8 shows the simulated maximum RF amplitude as a function of center fd for signals with three different number of pulses, 2, 10, and 30. From this figure, it is clearly evident that frequency peaks associated with the cutoff frequencies are broadened when less cycles are included in a wave packet. As a result, if many cycles are used, the test procedure can be much more selective. However, this will reduce the range of possible wavestructures.

The modulation envelop of the wave packet does not appear to have a large effect on the amplitude of the received wave packet, as figure 2.9 of the simulated maximum RF amplitude shows. However, the frequency response and the RF waveform do change considerably, as can be seen in figures 2.10 and 2.11. The sudden increase at the edge of the square modulated signals causes higher order harmonics to be generated that result in large "side lobes" in the frequency response. The interference caused by the different frequency components attributed to these side lobes complicates the received signal because more modes (with different group velocities) are generated. As a result, it is more difficult to extract useful defect analysis information.

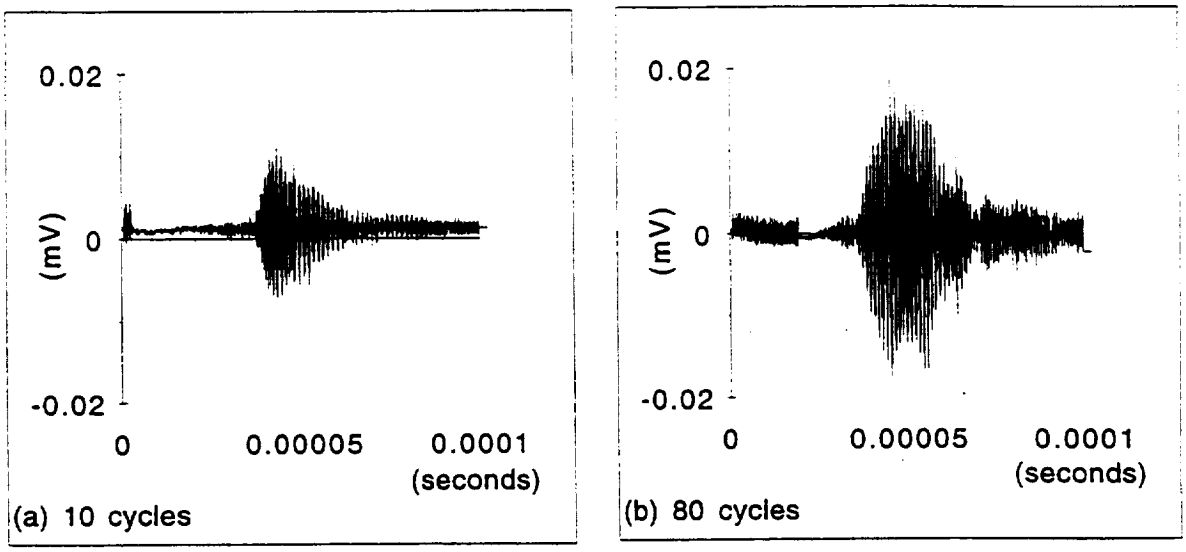

Figure 2.6 The experimental waveform obtained from (a) 10 cycle and (b) 80 cycle sine-modulated pulse using the AU technique. A half inch transducer was driven at 4.8 MHz on a 40 mil (1.016 mm) aluminum plate.

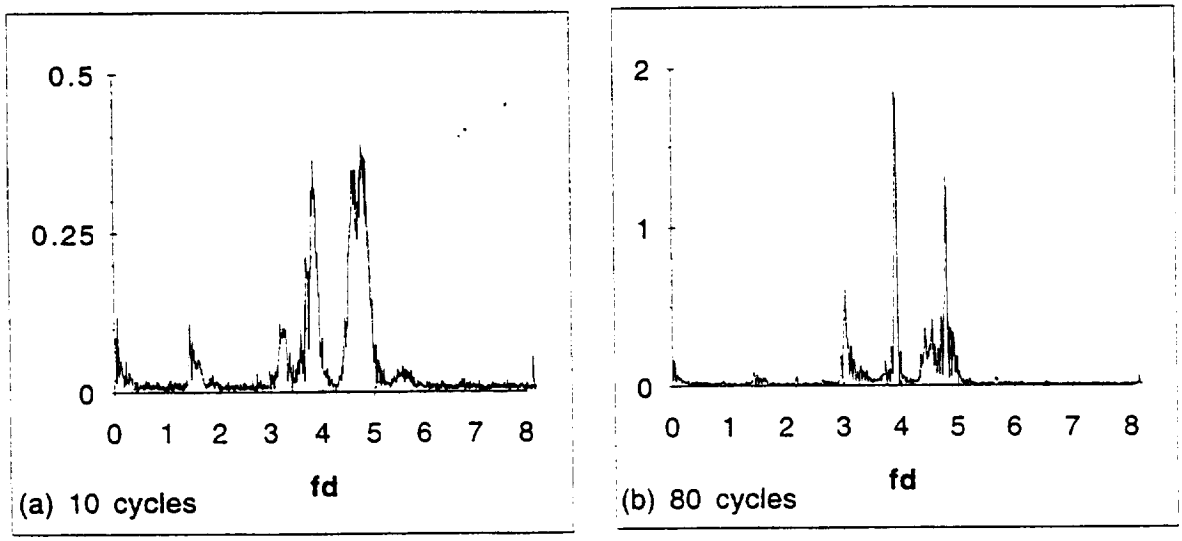

Figure 2.7 The experimental frequency response of (a) 10 cycle and (b) 80 cycle sine-modulated pulse, showing that the 80 cycle pulse has a much more narrow frequency bandwidth.

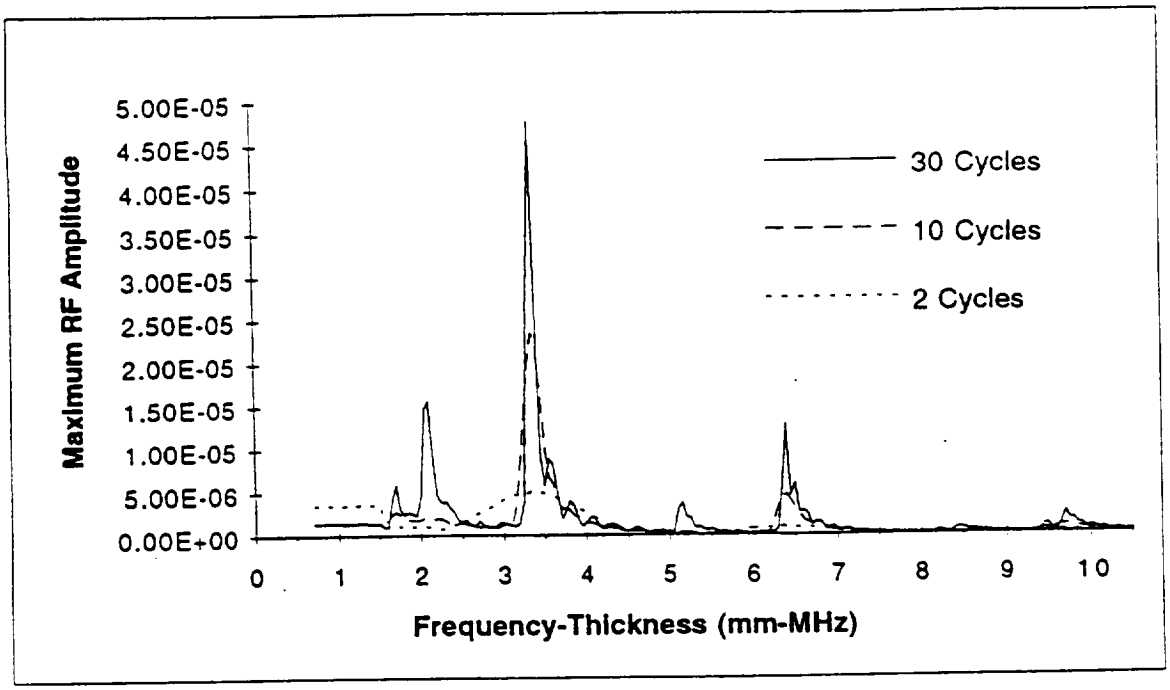

Figure 2.8 Simulated maximum RF amplitude vs center frequency-thickness for a sine-modulated signal consisting of 2, 10, and 30 cycles, propagating in a 1 mm Al plate. A longer wave packet has a narrower frequency bandwidth associated with it. As a result, modes are only generated near their cutoff frequencies.

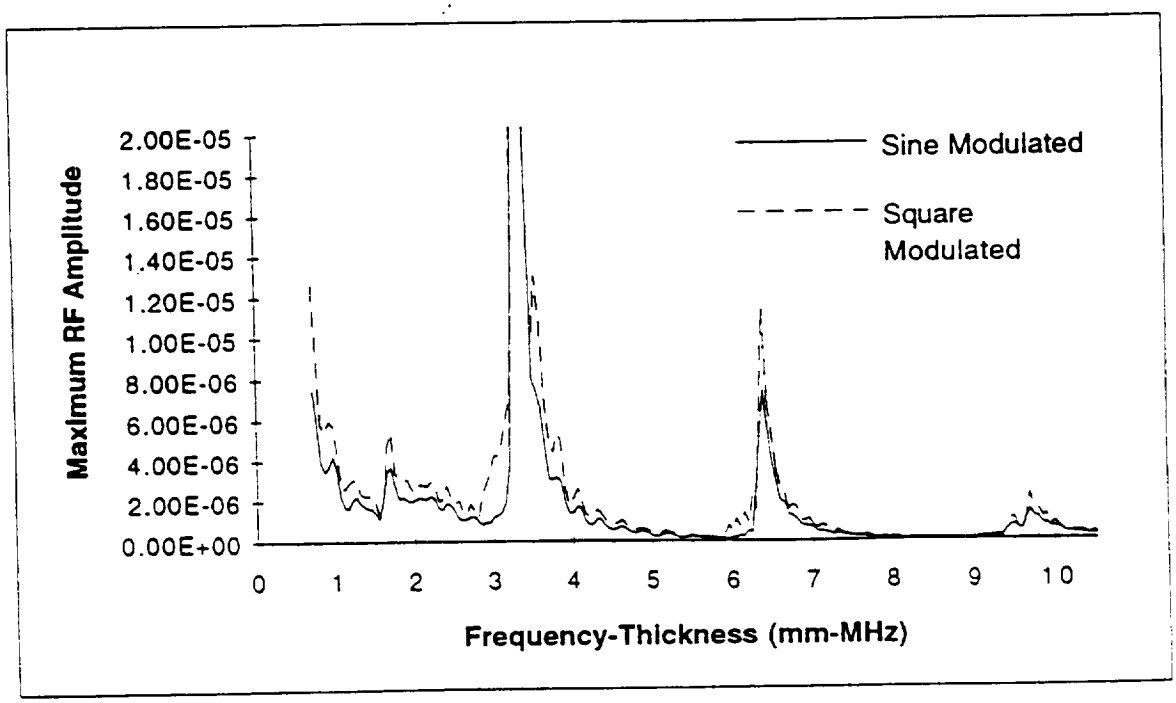

Figure 2.9 Simulated maximum RF amplitude vs center frequency-thickness for a sine and square modulated signal. (Parabolic pressure distribution, 10 cycles, on a 1 mm Al plate)

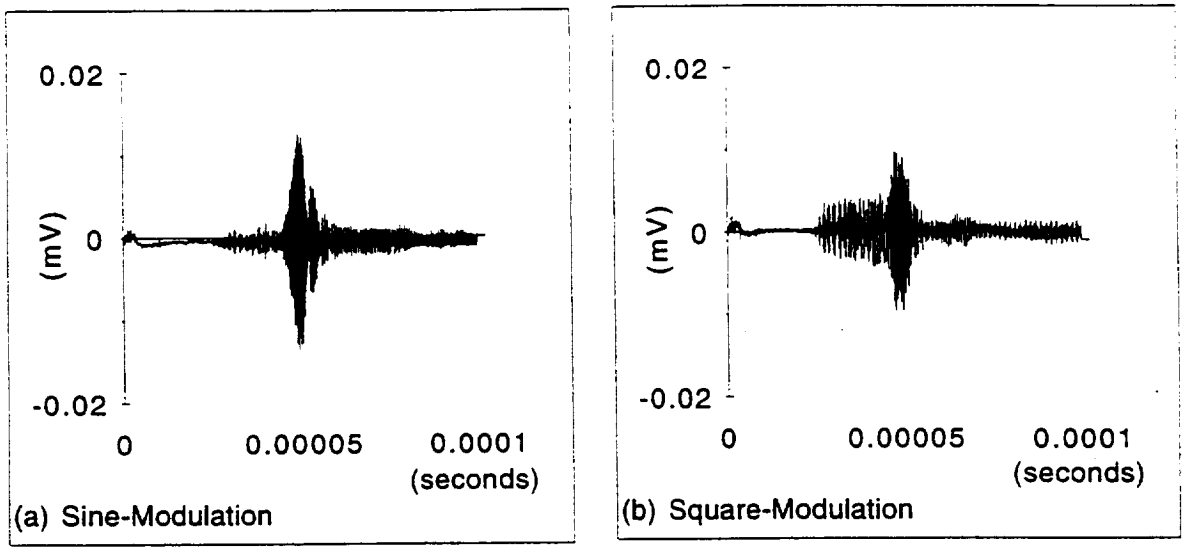

Figure 2.10 The experimental waveform obtained from (a) sine-modulated and (b) square-modulated 20 cycle pulse. A half inch transducer was driven at 3.43 MHz on a 40 mil (1.016 mm) aluminum plate.

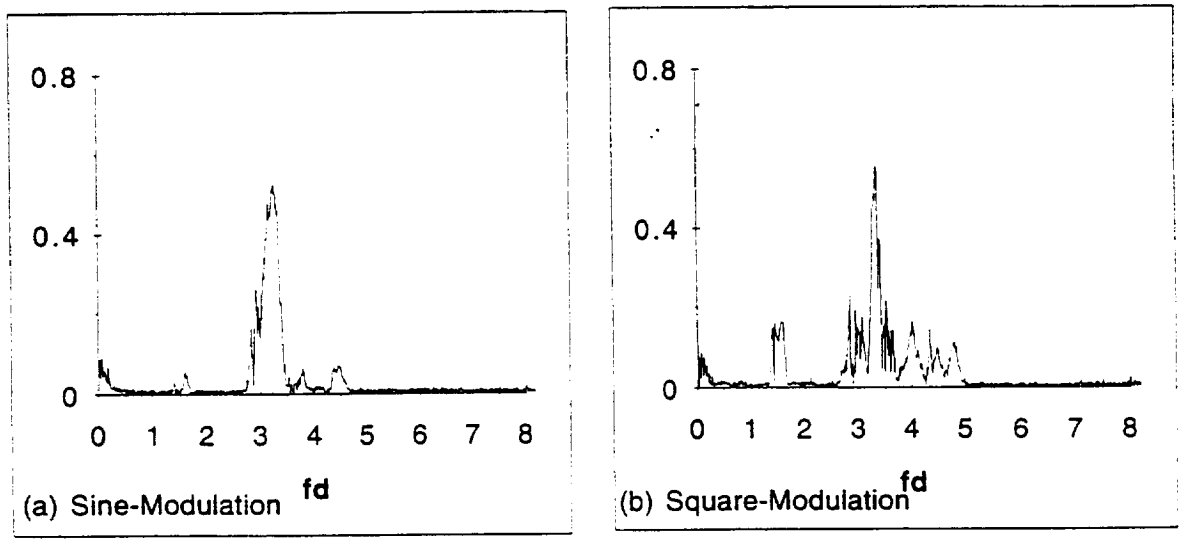

Figure 2.11 The experimental frequency response of (a) sine-modulated and (b) square-modulated 20 cycle pulse, showing the side-lobes and wider frequency range associated with a square modulated signal.

Chapter 3
The Effect of the Transducer's Size

Traditionally, the transducer's size is dictated primarily by the physical constraints of the testing location, the amount of power that needs to be put into the sample, and the center frequency of the transducer (since higher frequency ceramic transducers need to be thinner.) However, the effect that the size of the transducer has on what modes can be generated and on the phase velocities of the generated modes has frequently been neglected.

In AU, since the angle of incidence cannot be changed (as it can in the wedge technique) to select a certain phase velocity, the size of the transducer becomes the principle means that the experimenter has to control the phase velocity at which the wave is generated. Transducers placed normal to a plate's surface tend to generate plate waves with very high phase velocities. As the size of the transducer is increased, this effect becomes stronger and the preferred phase velocity also increases. So, by changing the size of the transducer, the phase velocity can be controlled, affecting which modes are generated.

Physical Understanding

In AU, modes tend to be generated at infinite phase velocities because the entire wavefront hits the material sample simultaneously. On the other hand, when an angle beam transducer is used the wavefront progresses down the material surface. By selecting an angle, a specific phase velocity can be selected by matching phases (Snel's law). However, because AU always uses normally incident transducers, it loses this ability to select any phase velocity, tending to generate waves at very high phase velocities.

The phase velocities at which modes can be generated is dictated by interference effects. Following Huygens' Principle, waves are generated simultaneously from all points on the transducer's face. These waves then interfere with each other. Waves that have short wavelengths (less than the transducer radius) corresponding to low phase velocities (the frequency is assumed to be constant = the frequency of the forcing function) experience more interference because they have a larger phase difference across the face of the transducer. This interference causes the response to fluctuate rapidly as the phase velocity changes. Longer wavelengths (higher phase velocities) mean that fewer wavelengths are created across the face of the transducer and the fluctuations occur less rapidly, because a greater change in wavelength is needed to transition from completely destructive to completely constructive interference. When half of the wavelength is approximately larger than the transducer diameter the response no longer fluctuates rapidly, because only one part of one wavelength is affected. All higher phase velocities are very excitable. As the phase velocity and wavelength continue to increase, the phase difference across the face of the transducer continues to decrease. The source's contribution reaches its maximum value when the phase velocity is infinite and each portion of the transducer creates a wave that has the same phase.

An infinitely large transducer will only generate waves at infinite phase velocities, while a point source will tend to generate every phase velocity. Finite sources fall in between these limits. In general, as the transducer diameter is increased, the phase velocities at which a wave is generated also increase because there will be a larger phase difference across the face of a larger transducer, increasing the wavelength and phase velocity above which the response no longer fluctuates and reaches a value near its maximum value. The practical consequence of this effect is that a transducer whose diameter is smaller than the wave packet's wavelength will be able to reach down into the lower phase velocities effectively, but a larger transducer will only effectively excite high phase velocities. At low phase velocities, a large transducer's response fluctuates rapidly.

Mathematical Modeling

The relationship between the transducer size and the phase velocity is clearly demonstrated by the solution to the time-harmonic problem. The source-dependent term of the solution is defined as the Hankel transform of the pressure distribution. In the piston case, for example, the source term becomes $-aPJ_1(\xi a)/\xi$, where a is the transducer's radius, ξ is the wavenumber, and J_1 is the first order Bessel function. As can be seen from this term, larger diameter transducers cause the source term to fluctuate more rapidly than smaller diameter sources do. This has two consequences. At low phase velocities (corresponding to high wavenumbers) the source term changes more rapidly for larger sources. The consequence of this effect will be discussed below. Also, the wavenumber at which the source term reaches its first null is larger for a smaller source. This first null corresponds to the phase velocity beyond which the source term no longer fluctuates. So, a small source will reach down to lower phase velocities than a larger source (or reach up to higher wavenumbers since the wavenumber is related to the phase velocity, as $\xi = \omega/v_{ph}$, far enough away from the source). Figures 3.1 and 3.2 show these effects. Figure 3.1a shows the value of the source term (essentially a Bessel function) at one MHz vs. the wavenumber for the piston source. Figure 3.1b shows the same information plotted against the phase velocity, demonstrating how smaller sources can excite lower phase velocities than large sources. A parabolic pressure distribution displays the same type of behavior, as seen in figure 3.2.

Since the wavenumber term helps account for energy considerations associated with finite-size sources, it is helpful to lump the source and wavenumber terms together and study the response. Although the source term by itself reaches a maximum value when the phase velocity is infinite (figure 3.1), the value of the source-wavenumber term fluctuates rapidly at lower phase velocities, reaches a maximum value at a finite phase velocity, and then decays asymptotically to zero at infinite phase velocity (figure 3.3).

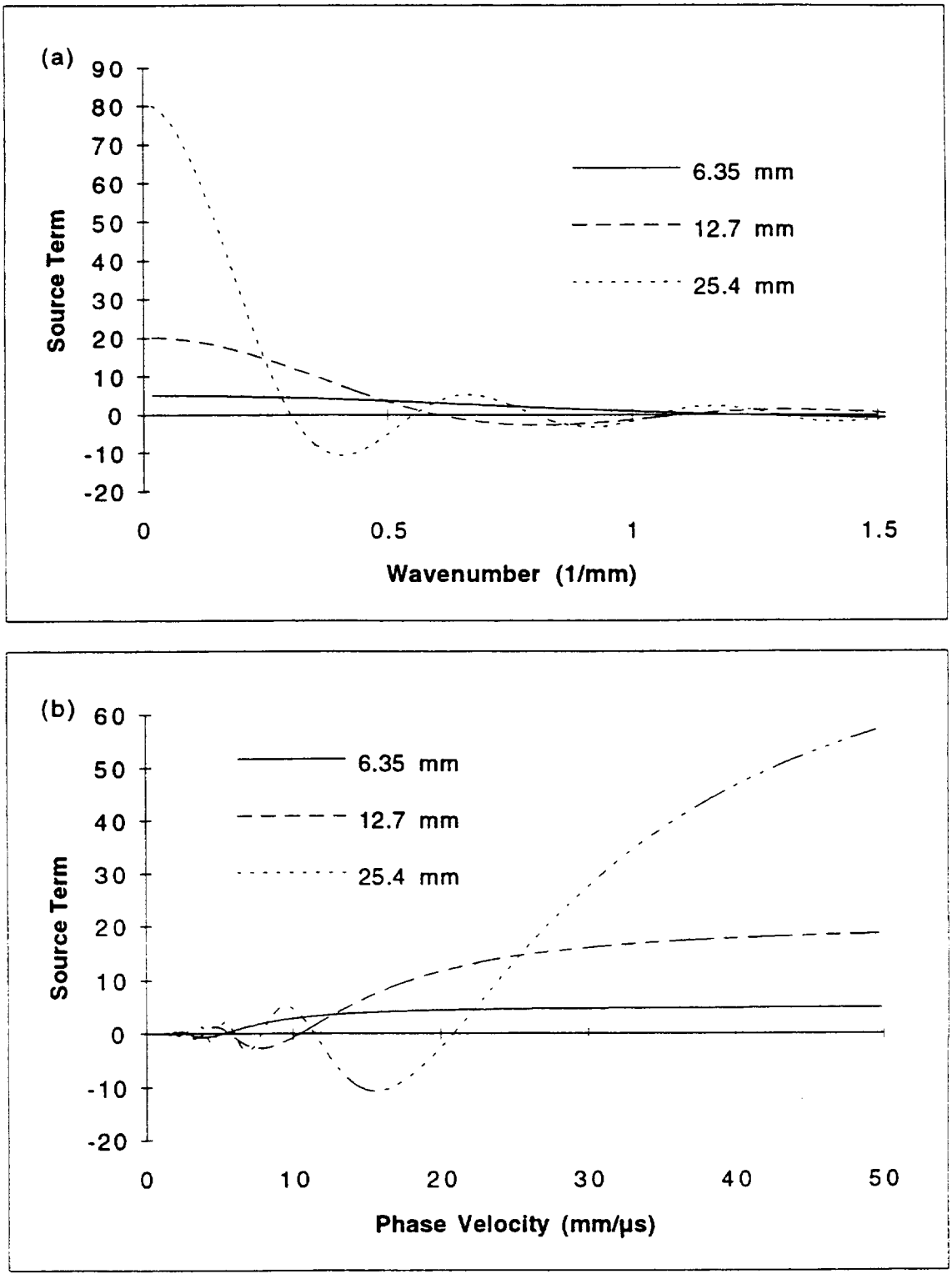

Figure 3.1 The source term for three different diameter PISTON sources as a function of (a) wavenumber and (b) phase velocity, showing that normal surface loads tend to generate waves with infinite phase velocities and zero wavenumbers

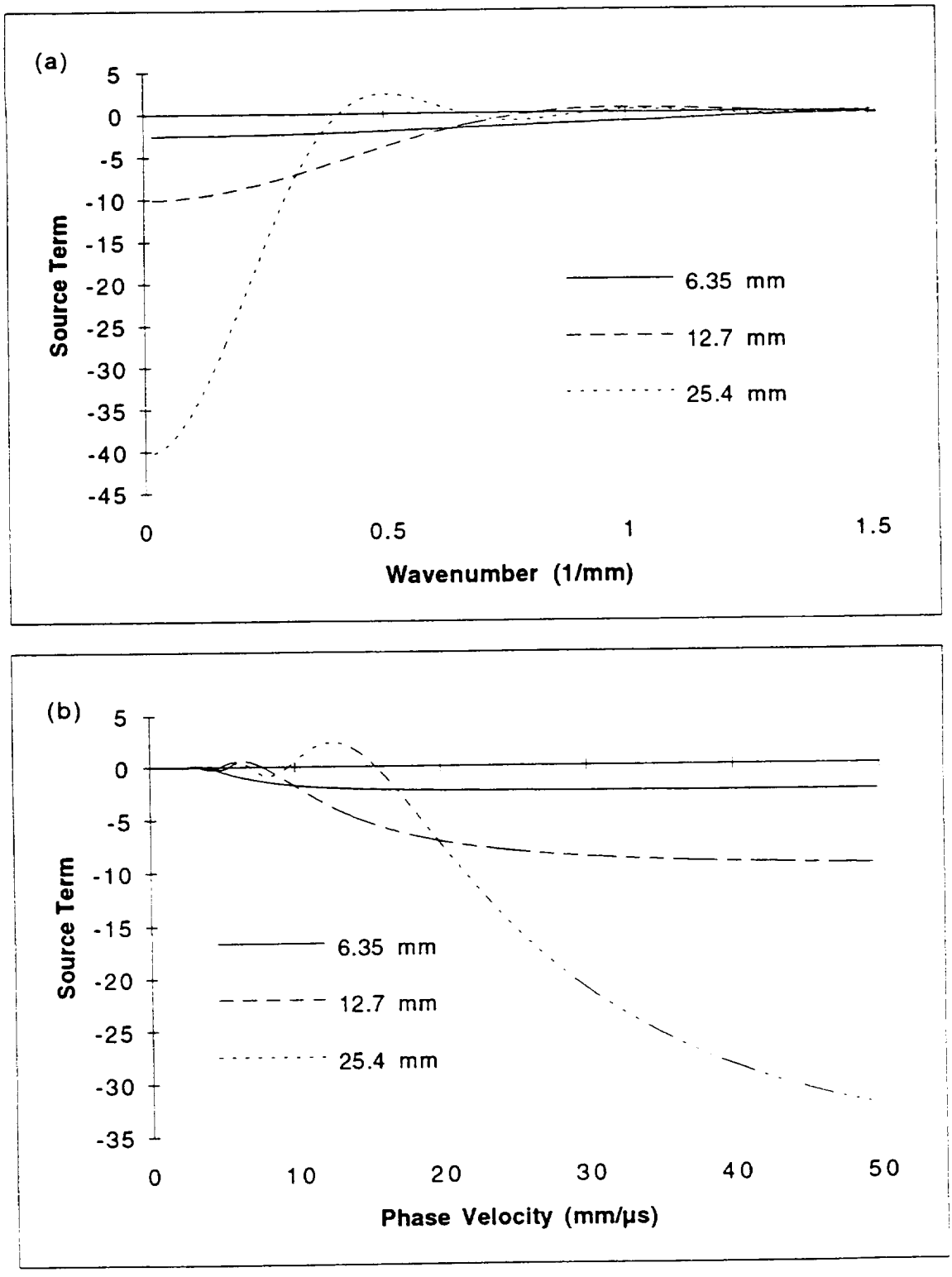

Figure 3.2 The source term for three different diameter PARABOLIC sources as a function of (a) wavenumber and (b) phase velocity, showing that normal surface loads tend to generate waves with infinite phase velocities and zero wavenumbers

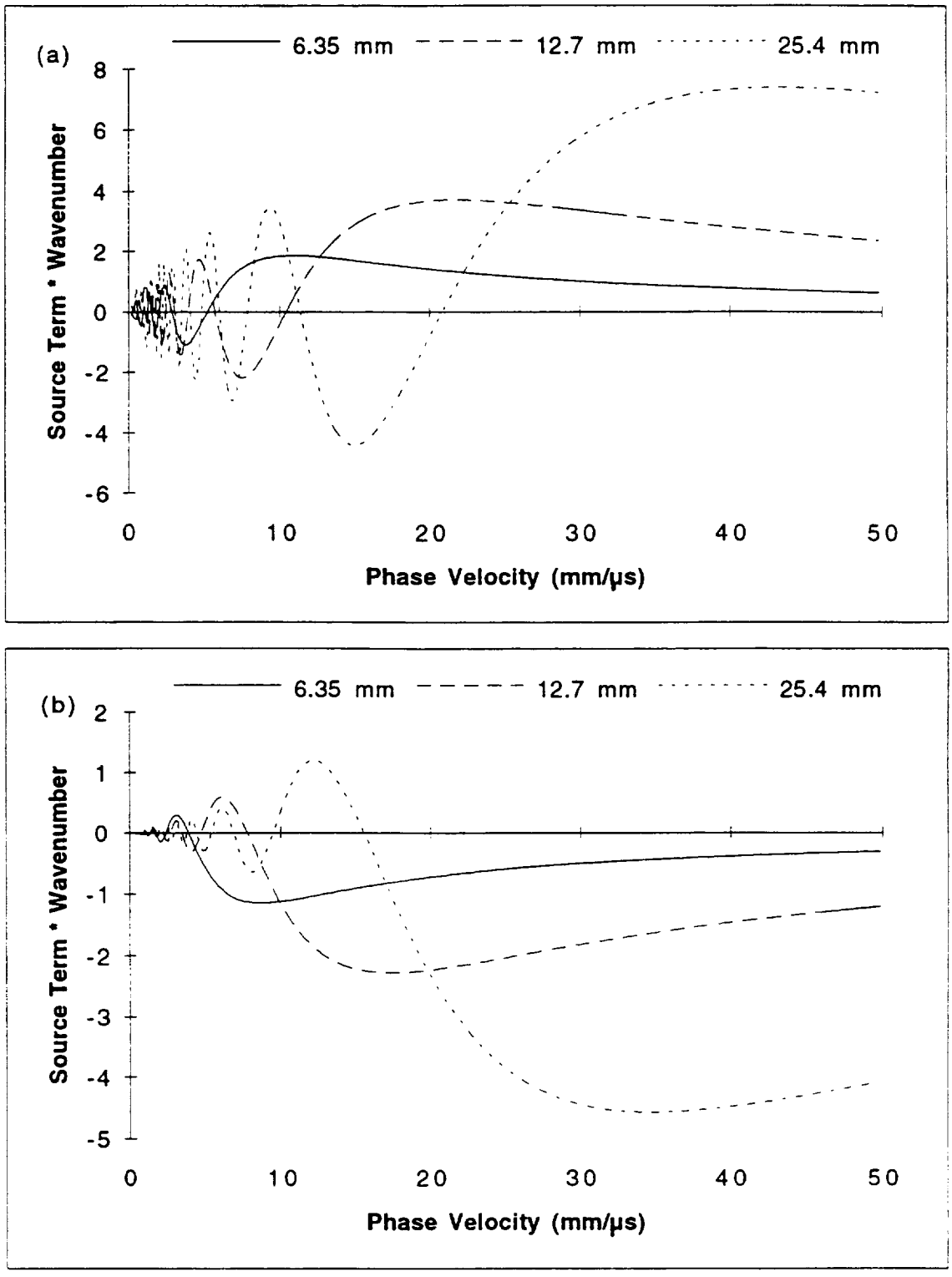

Figure 3.3 The source term multiplied by the wavenumber for three different diameter (a) PISTON (b) PARABOLIC sources, showing the "far field" phase velocity after which the term decays due to energy considerations

This creates a profile that closely resembles the amplitude profile that describes the near/far field of a transducer impinging on a bulk material (which is another expression of Huygens' Principle). Because of the minima that occur before the "far field" phase velocity, modes with low phase velocities at that particular frequency may or may not be generated, just as a defect very close to a transducer may or may not be seen.

The decay in the total response as the phase velocity becomes infinite can be interpreted physically. As the phase velocity and wavelength increase, the transducer drives a smaller portion of the wave. This causes the wave's energy to be distributed over a wider range of frequencies. However, because of the plate's boundaries, only certain frequencies that correspond to Lamb waves are "allowed" at a particular phase velocity. As a result, once, less energy is transferred into a mode as the phase velocity increases. The radiation condition also requires that the response decays to zero as the phase velocity goes to infinity. Otherwise, a finite source would need to create an infinite amount of the energy. In addition to these two energy conditions, wave propagation principles indicate that infinite phase velocities cannot be generated by a finite source. A mode's group velocity is zero at every point on the dispersion curve where the phase velocity is infinite (corresponding to the cutoff frequencies). As a result, the waves with infinite phase velocities do not propagate.

An expression for the location of the "far field" phase velocity can be found by solving for the first maximum of the wavenumber-source term and then converting the result to phase velocity. The first maximum of $J_1(z)$ occurs at $z = 1.84118$ (Abramowitz and Stegun, 1972), therefore, assuming that the material response is constant, the phase velocity at which a mode tends to be most strongly excited by a piston source is,

$$v_{ph} = \frac{2\pi fa}{1.84118} \tag{3.1}$$

and for the parabolic source, the maximum will occur near

$$v_{ph} \approx \frac{2\pi fa}{2.300} \tag{3.2}$$

where f is the frequency and a is the transducer's radius. These values are only approximate because they do not take into account that each mode's material response is also function of wavenumber. This will cause the "far field" phase velocity to be different for each mode. For example, the A3 mode should be excited at higher phase velocities than the S2 mode, because it's material response (out-of-plane surface displacement) increases more dramatically with increasing phase velocity.

The "far field" phase velocity value can be used to determine what phase velocities are sure to be excited. For example, equation (3.2) indicates that a 4 mm diameter source can generate the fundamental symmetric mode (S0) consistently at 1.0 MHz, but at 3.0 MHz, the source would need to be smaller than 1 mm in diameter. Although this small of a transducer is not very practical with conventional techniques, laser generated ultrasound may be able to generate a wave efficiently at a low enough diameter. However, if such a small transducer is used, not only the fundamental mode, but also all of the higher order modes that exist at that frequency will be generated, since the value of the source term decays very slowly as the phase velocity is increased. As a result, the signal will be complicated by the many modes propagating in the plate.

To fully understand which modes will be generated, the total response of the system must be considered. Neglecting the constants and the radial wave term, this total response is equal to the source term multiplied by the wavenumber and the material response. Figure 3.4 shows the source term in fd-phase velocity space and figure 3.5 shows the total response obtained by multiplying figure 3.4 and figure 2.3, the response to a point source. The 0.77 mm source, shown in figure 3.5a, has very few nulls and can generate almost any mode. As the size of the transducer is increased, however, more nulls appear and certain parts of the dispersion curve become impossible to generate. If high enough phase velocities were examined, it would be seen that each of the modes (except those that become complex) reach a maximum response at some phase velocity and then they decay. This maximum can be seen in the response of the 6.35 mm source.

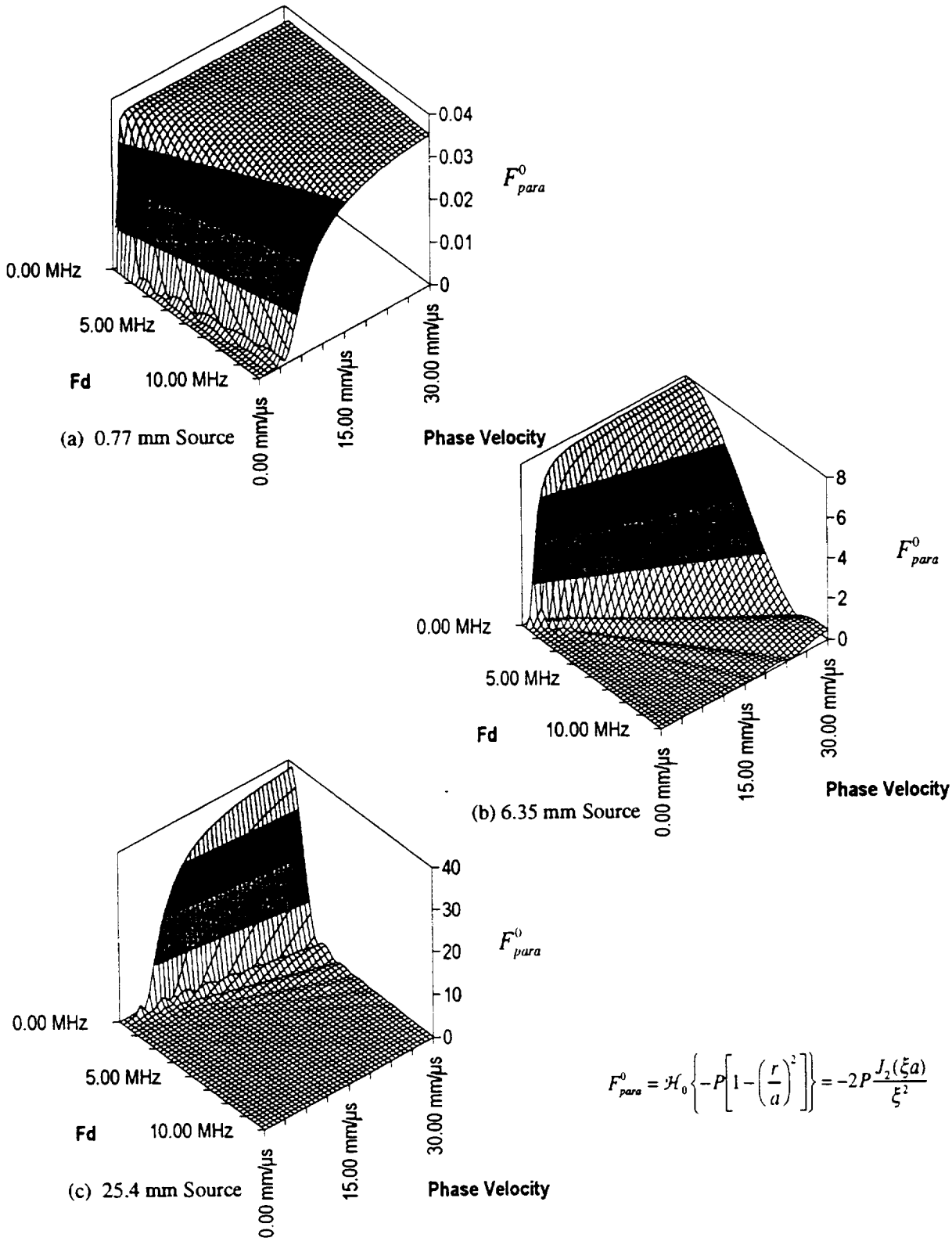

Figure 3.4 Absolute value of the source term for a (a) 0.77 mm, (b) 6.35 mm, and (c) 25.4 mm diameter source with a parabolic pressure distribution, shown in frequency-thickness-phase velocity space. The source term is equivalent to the Hankel Transform of the normal pressure distribution of the source, which reaches a maximum value when the wavenumber is zero.

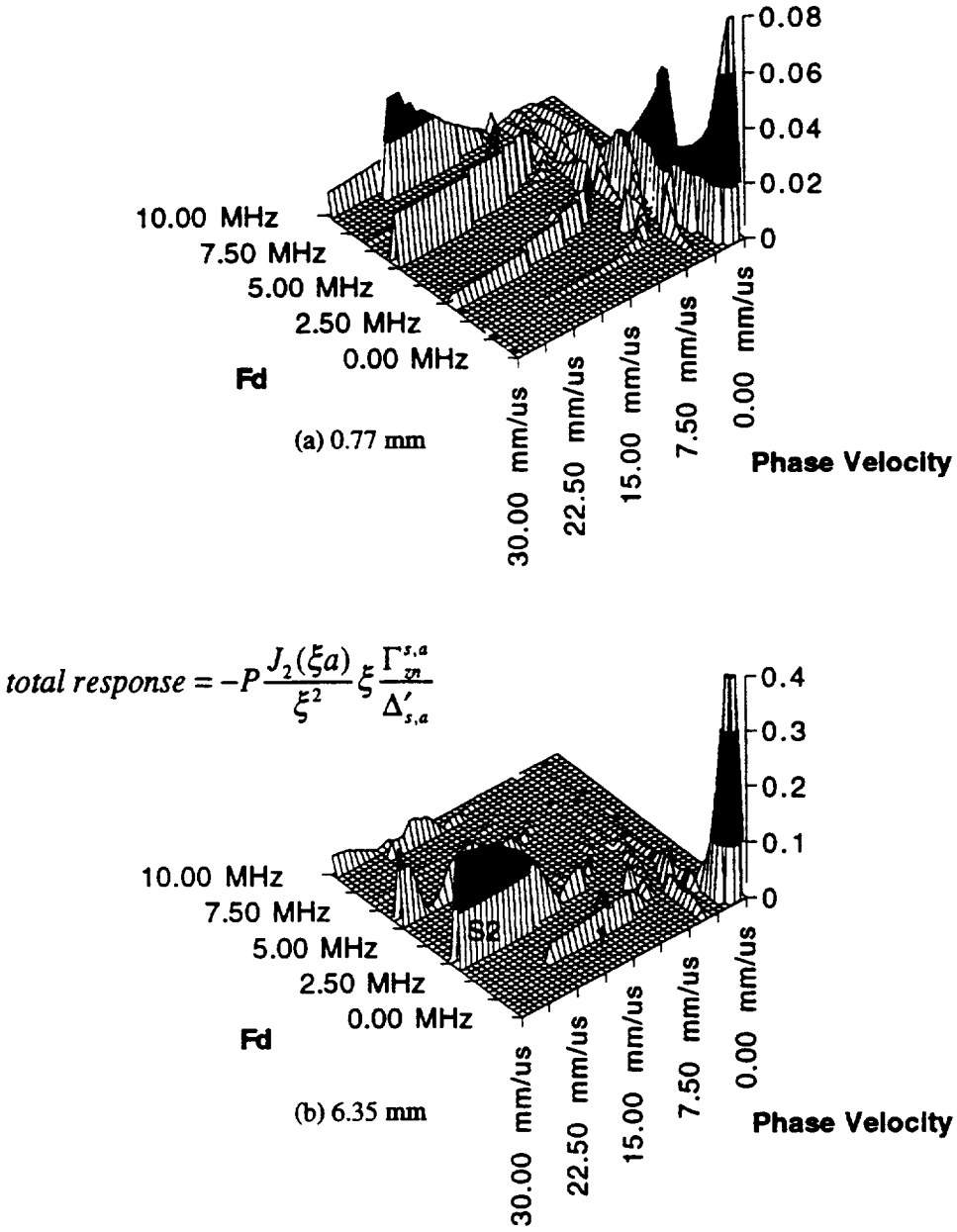

Figure 3.5 The total response (source, wavenumber, and material response) in fd-phase velocity space for (a) 0.77 mm, (b) 6.35 mm, (c) 12.7 mm, and (d) 25.4 mm parabolic source on a simulated aluminum plate.

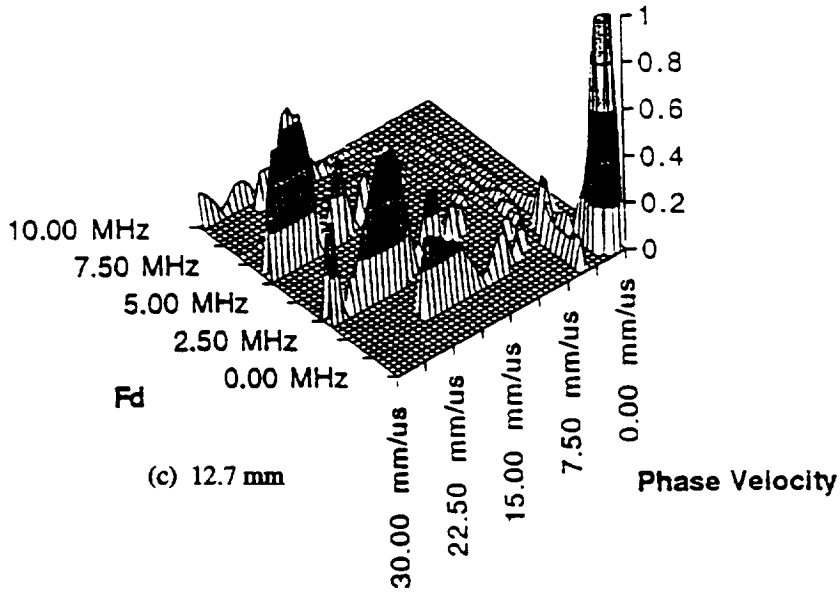

(c) 12.7 mm

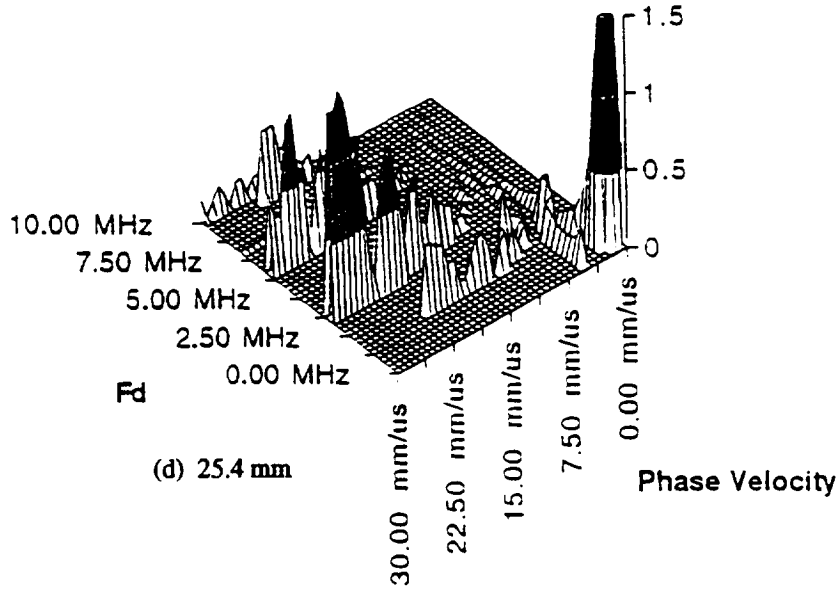

(d) 25.4 mm

Figure 3.5 (cont)

The value of the A1 mode peaks around 12 mm/μs and then begins to decay as the phase velocity continues to increase. The S2 mode, which is much larger than the surrounding peaks, is just about to reach its maximum. The phase velocities shown are not high enough to detect the maximum values for the 12.7 mm or the 25.4 mm sources. These maxima should occur near 70 and 150 mm/μs respectively. The erratic behavior of the modes in this low phase velocity region explains the "hit or miss" nature of generating modes at low phase velocities by normal surface tractions.

Pressure Distribution

Figure 3.3 allows the comparison of the values of the source-wavenumber term for piston and parabolic pressure distributions. By comparing figure 3.3a and b, it can be seen that the parabolic profile reaches its maximum amplitude at a lower phase velocity that the piston does, as predicted by equations (3.1) and (3.2). Sample RF signals and for the two types of sources (piston and parabolic) at 1 MHz are shown in Figure 3.6. The rapid fluctuation of the source term at low phase velocities accounts for the large change in the signals, as described below.

Comments on Fundamental Modes

Figure 3.7 shows how the simulated frequency response and RF signal of a system changes for three typical transducer diameters (f = 1 MHz, d = 1 mm, 10 cycle sine modulated parabolic source). The width of the main envelop of the received frequency spectrum is primarily dependent on the frequency spectrum of the source and the material response. However, since a range of frequencies are excited, interference causes minima to occur in the received frequency spectrum. The exact interference pattern is hard to predict for the fundamental modes since the source profile varies so rapidly at low phase velocities. However, in general, the number of minima will increase as the size of the transducer is increased because there will be a larger phase difference

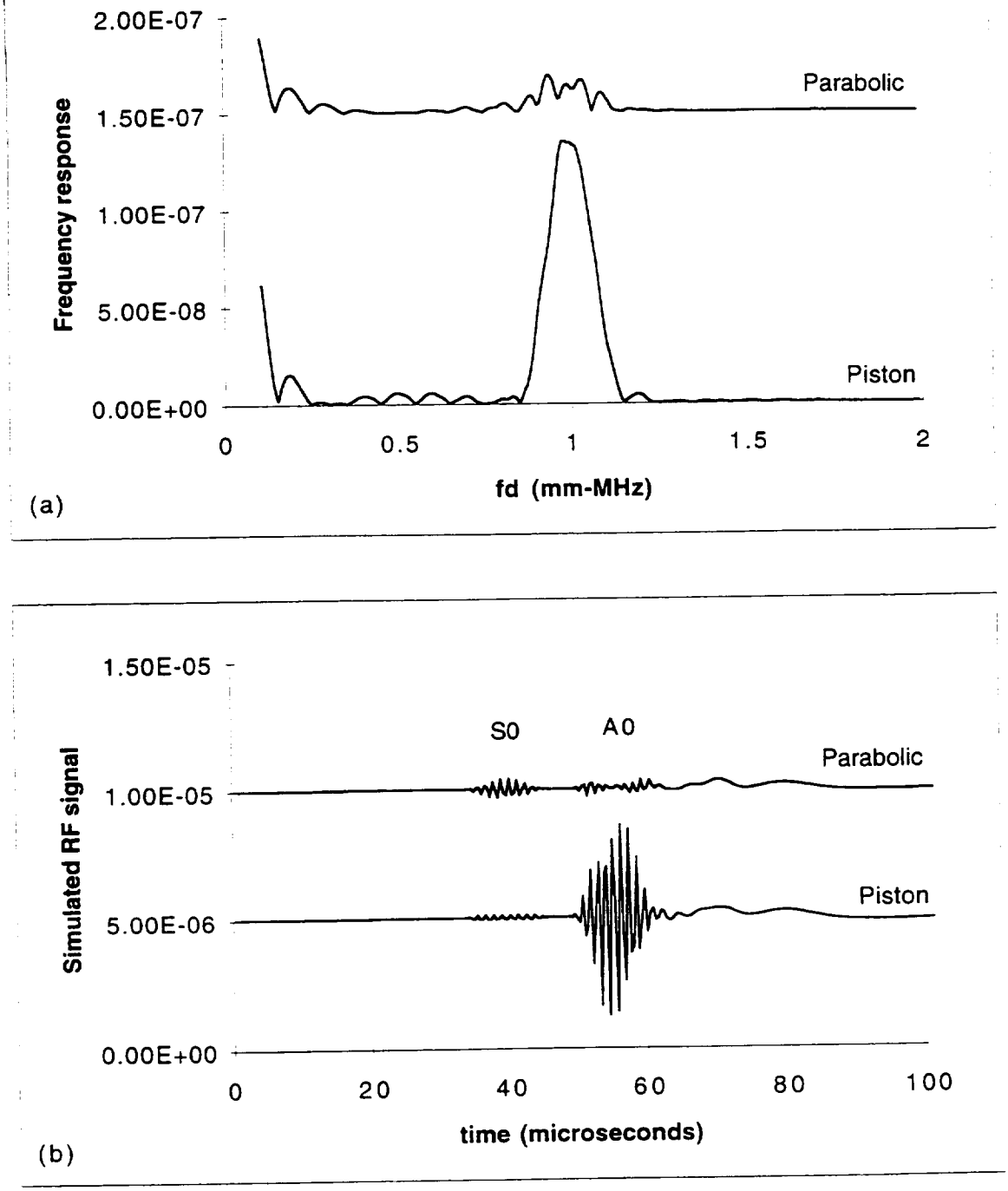

Figure 3.6 The (a) simulated frequency response and (b) simulated RF signal for a 12.7 mm source with two different pressure distributions. The results represent a 10 cycle pulse propagating in a 1 mm Al plate at fd=1.0 mm-MHz. The large change in the signals shows how erratically the system behaves and what a large effect the pressure distribution can have at low phase velocities.

across the face of the transducer, resulting in more points of destructive interference. In figure 3.7, the size of the transducer is of the same order of the magnitude as the thickness of the plate (the diameter/wavelength ratios are approximately 1.2, 2.3, and 3.8 for the quarter, half and one inch transducers respectively), causing relatively strong minima. As a result, small changes in the material or the transducer properties have a large effect on the received signal. The solutions only become stable for modes whose phase velocities are larger than the "far field" phase velocity given by equations (3.1) and (3.2).

The simulated RF signal (figure 3.7b) shows that the A0 mode (with the lowest phase velocity and a slower group velocity) dominates the signal from the 6.35 mm source, while S0 dominates the 12.7 mm source and the two fundamental modes are excited equally by the 25.4 mm source. However, figure 3.8 demonstrates how erratic this behavior is. These two figures show the frequency response and the simulated RF waveform for a 1.1 MHz source. The 0.1 MHz-mm change drastically modified the interference pattern and the system's response.

In figures 3.7a and 3.8a (simulated FFTs of a 1 MHz and a 1.1 MHz transducer), it can be observed that only the fundamental modes (S0 and A0) are generated, since the next highest mode, the second anti-symmetric mode (A1), does not propagate below fd = 1.6 mm-MHz. Because the phase velocities of the zero modes are always finite the small transducer is able to generate these modes more efficiently than the larger transducers. As a result, the absolute magnitudes of the RF signals from the different size sources in Figures 3.7b and 3.8b are approximately equal although the largest transducer's contact area is 16 times greater than the smallest transducer. This has significant practical effects. Using a larger transducer will not increase the power transmitted to the fundamental modes, as long as the pressure density (proportional to driving voltage) remains the same.

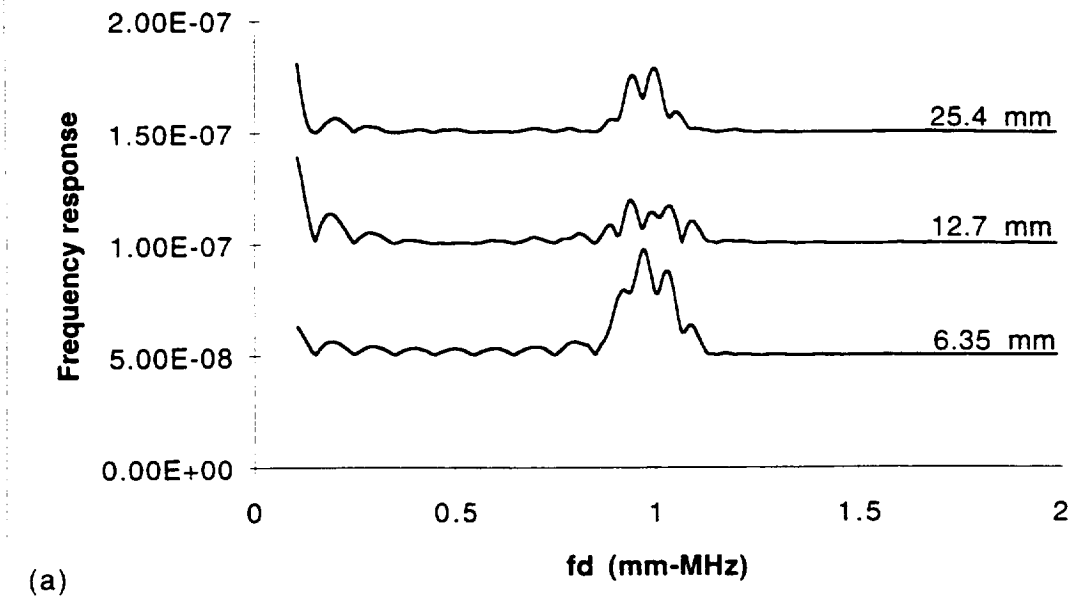

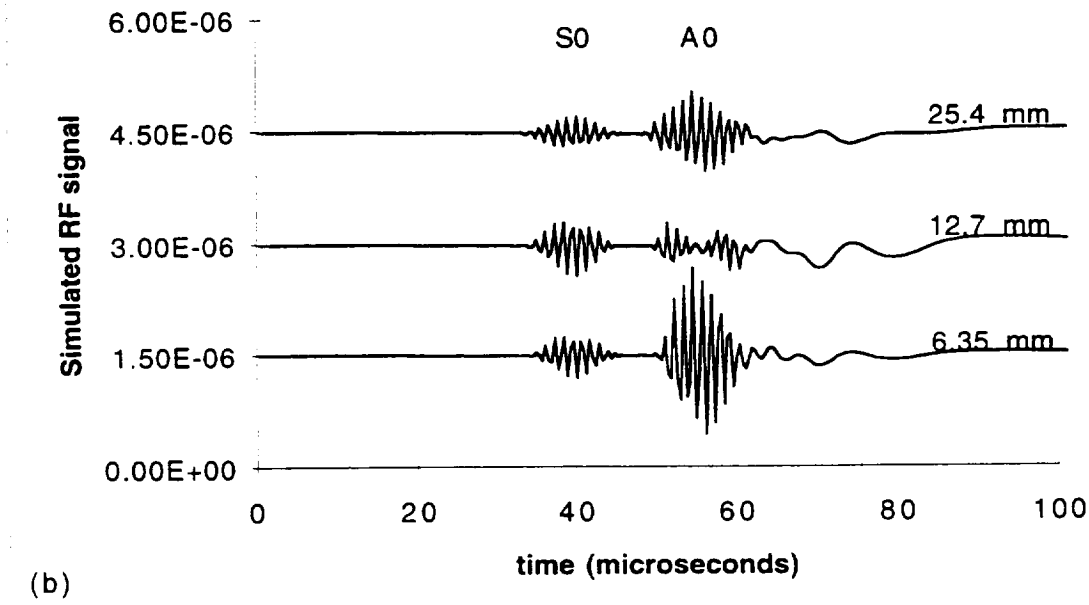

Figure 3.7 The (a) simulated frequency response and (b) simulated RF signal for three different size parabolic sources on a 1 mm Al plate at fd=1.0. The amplitude of the RF signal from the 6.35 mm source is greater than the signal from the larger sources because the smaller transducer is able to excite lower phase velocities and therefore "reach down" to the fundamental modes. There is also a change in the ratio of the modes as the size of transducer is changed.

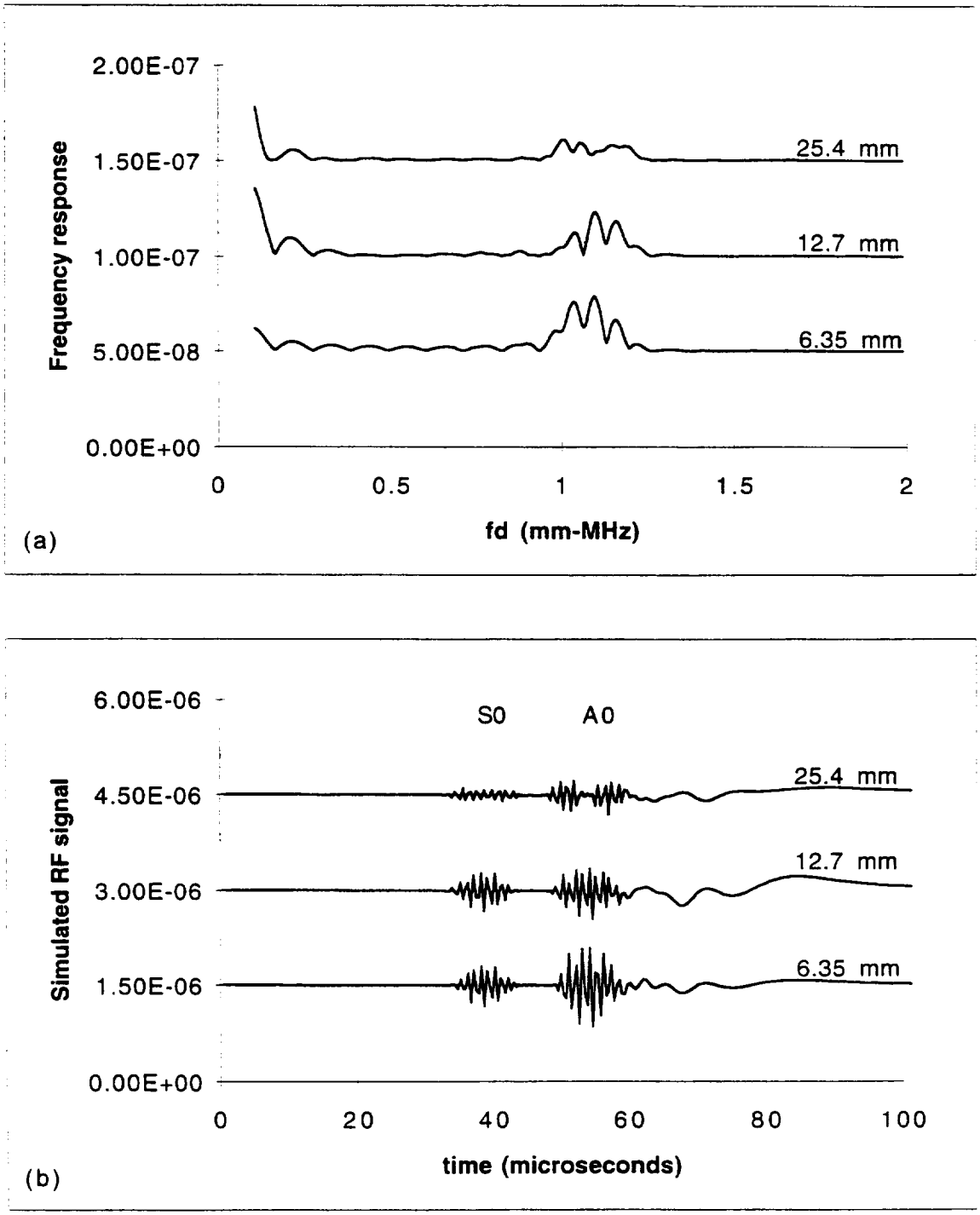

Figure 3.8 The (a) simulated frequency response and (b) simulated RF signal for three different size parabolic sources on a 1 mm Al plate at fd=1.1. Comparing these results with the results obtained at fd=1.0 shows how erratically the system behaves at low phase velocities.

Higher Order Modes

Although the fundamental modes can be generated using Acousto-Ultrasonics, unless a small transducer or very low frequency is used, the received signals are generally weak. To avoid complicated signal processing routines and to take advantage of different wavestructures, higher frequencies can be used to generate higher order modes at their cutoff frequencies. Modes that have predominately longitudinal displacements at these points (for example, S2, A3, S6) are extremely excitable.

Figures 3.9 demonstrates how strongly the cutoff frequency peaks influence the excitability of a wave for three different size transducers. Each point on the graphs represents the maximum amplitude of a simulated time-domain waveform for a source that is centered on that fd and has a fixed fd bandwidth. Plots are shown for a quarter, half, and one inch transducer. As expected, the larger transducers have much larger peaks at the cutoff frequencies. At other frequencies, almost no wave propagates. However, the smaller sources, which generate waves at lower phase velocities are not as influenced by the high excitabilities at modes' cutoff frequencies and show a more even distribution over changing frequency ranges.

Experimental Results

Figure 3.10 compares simulated and experimental results. Figure 3.10a is similar to figure 3.9a, the simulated maximum RF amplitude vs center fd for three different size transducers, except that the simulated frequency response was multiplied by the magnitude spectrum of the transducer used in the experiments, to account for its frequency characteristics. Figure 3.10b, which contains the experimental data, was created by directly measuring the maximum time-domain voltage from a LECROY 9310 digital oscilloscope. Krautkramer-Branson Gamma (narrow band) transducers were driven by a modulated 20 cycle pulse and oil coupled to a four by six foot 87 mil

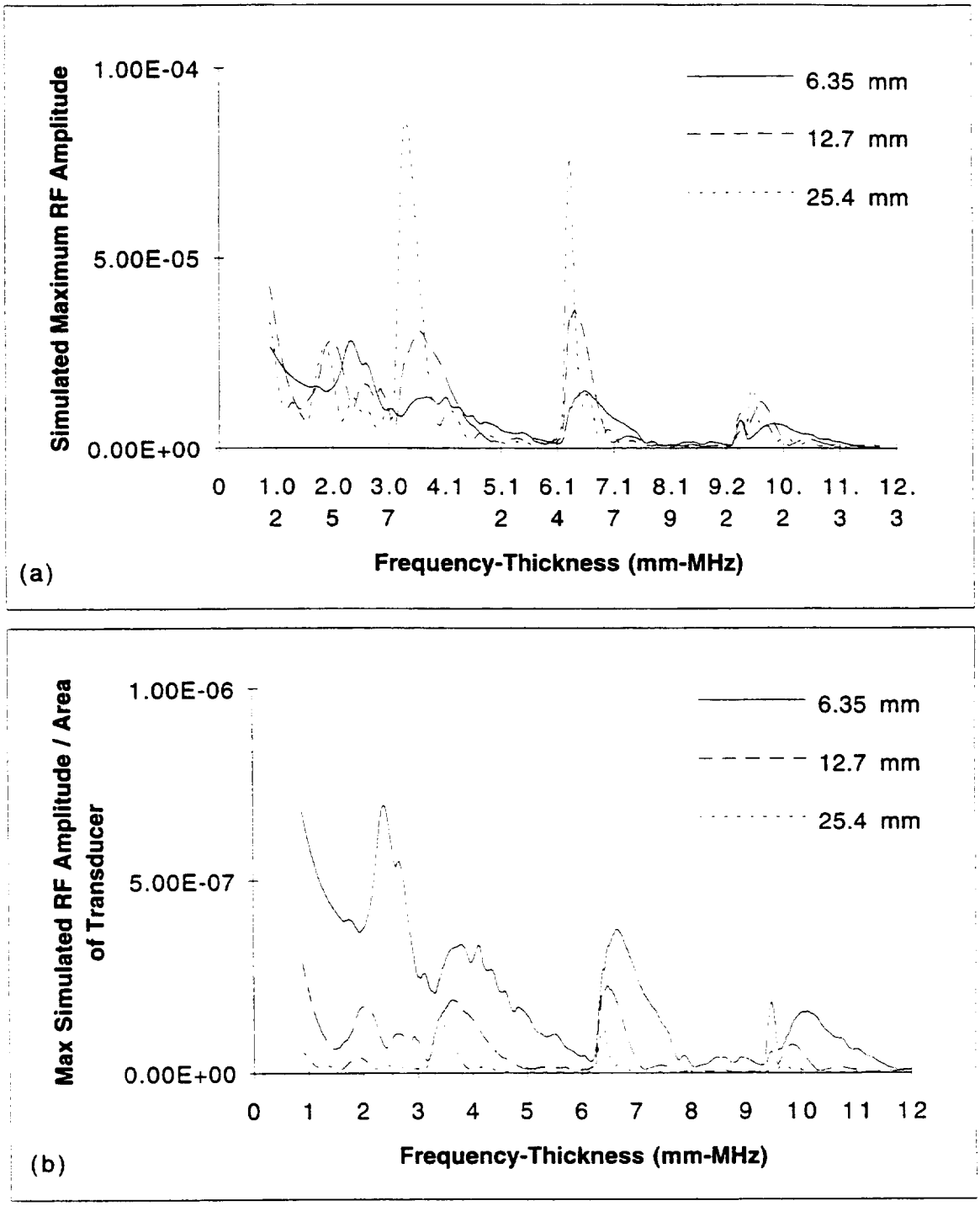

Figure 3.9 The (a) simulated maximum RF amplitude and (b) the maximum simulated RF amplitude normalized by the area of the transducer, shown versus the center frequency-thickness for three different size transducers. (Assuming a 10 cycle sine-modulated signal created by a parabolic source on an 87 mil plate.) The 6.35 mm transducer is able to generate waves effectively at more frequencies than the 25.4 mm transducer because it can excite modes at lower phase velocities and is therefore not as affected by the modes' cutoff frequencies.

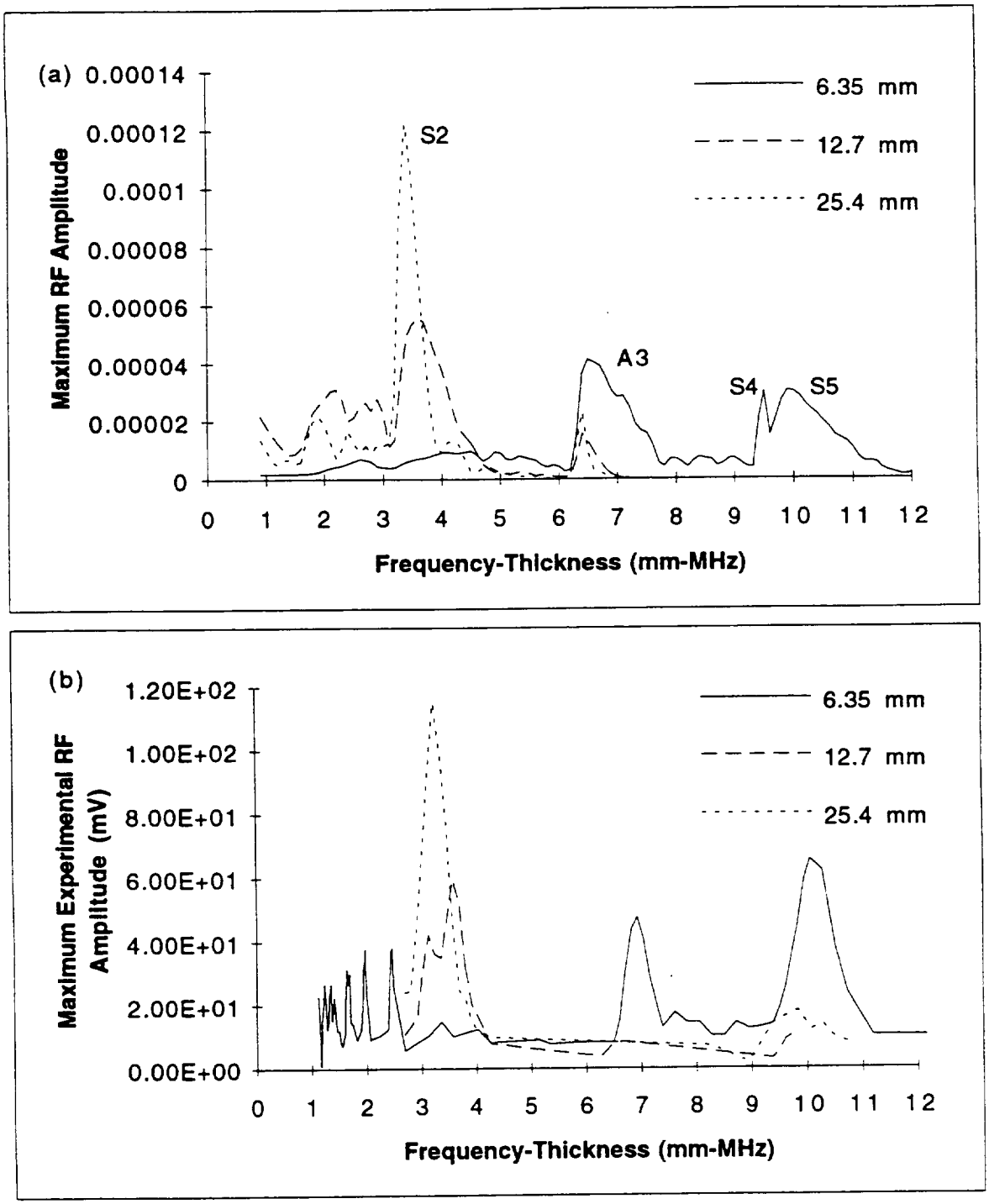

Figure 3.10 Comparison of (a) simulated maximum RF and (b) experimental maximum RF amplitude. (10 cycle sources on an 87 mil plate, two inch radial separation) The simulated max RF was multiplied by the frequency response of the experimental transducer

aluminum plate. Two one inch transducers were used, with 5.0 MHz and 2.25 MHz center frequencies. The quarter and half inch transducers both had 5.0 MHz center frequencies. Although he relative amplitudes of the three different size sources can not be directly compared because the pressure amplitude and the transmission through the couplant could vary, the qualitative trends of each of the curves should be accurate.

There is good qualitative correlation between the simulated and experimental results. At low fd's, the maximum RF amplitude fluctuates rapidly, as the simulation predicted. At higher fd's, the one inch transducer shows a much larger and steeper S2 peak (fd = 3.2) than the smaller transducers, after which it decays. The quarter inch transducer, on the other hand, peaks before the S2 mode even comes in (primarily due to the excitability of the fundamental modes). Its A3 (fd = 6.3) and S5 (fd = 9.6) peaks are as large as the S2 peak, as opposed to the larger transducers, which generate the S2 mode much more strongly than any others, as the simulation predicted. These results show that the maximum RF amplitude plot can be used as a quick way of identifying frequencies that efficiently generate a mode and it also serves an easy way to compare the effects of certain parameters.

Application to Adhesive Bonding

The size of the transducer can have a large influence on many practical applications, for example in adhesive bond testing on aircraft. The bonding of reinforcement plates on the back of an aircraft's skin can be tested by sending a guided wave across the area where the reinforcement should be. If the reinforcement is well-bonded, some of the energy "leaks" into it, if it is poorly bonded the guided wave travels undisturbed. In essence, a well-bonded plate increases the thickness of the plate and changes the dispersion curves in that region. A small transducer will be less able to detect this difference than a large transducer because it is excitable at many frequencies and may be able to adapt to the new boundary conditions. The opposite may be true for

the evaluation of lap-shear joints. Since in that setup energy must be transferred from one sheet to another of similar thickness, a large transducer's (small bandwidth) signal may be unduly affected by the thin layer of adhesive. More work should be done to explore these effects. The reader may wish to refer to Rose (1994) or Rokhlin (1991) for more information on adhesive bonding evaluation.

Frequency Shift

The size of the transducer also affects the frequency at which a mode tends to be generated, as previous researchers have noted (Ditri 1992, Rose 1993). Since the phase velocity of all real outward propagating waves decreases as the frequency increases, exciting waves at a higher phase velocity (by a larger diameter probe) causes the frequency to decrease. Figures 3.11 and 3.12 show this effect. The frequency responses in figure 3.11 were taken at the frequencies and at which the time domain amplitude peaks (1.80, 1.60, and 1.50 MHz respectively). The responses in figure 3.12 were all taken at 1.5 MHz center frequency (fd = 3.35 mm-MHz). Figure 3.13 shows representative time domain signals for this region of interest.

It is interesting to note that in figures 3.11 and 3.12 the S1 peak (the short one at 1.4 MHz) stays at 1.4 MHz for all three size transducers, while the S2 peak (the big one) shifts to the left as the diameter of the transducer increases. The dispersion curves help explain this phenomenon. The S1 dispersion curve ends at a relatively low phase velocity (8.0), since at that point the wavenumber becomes complex, causing the wave to quickly attenuate. (See Mindlin (1960) p. 445 [219]) for more information on the development of the dispersion curves.) As a result, S1 will be excited at nearly the same frequency, regardless of the transducer's preferred phase velocity. Although the frequency stays constant, the size of the peak changes depending on the location and amplitude of the local maxima of the source term. The S2 dispersion curve, on the other hand, rises gradually as the frequency decreases. Consequently, the S2 peak shifts as it responds to

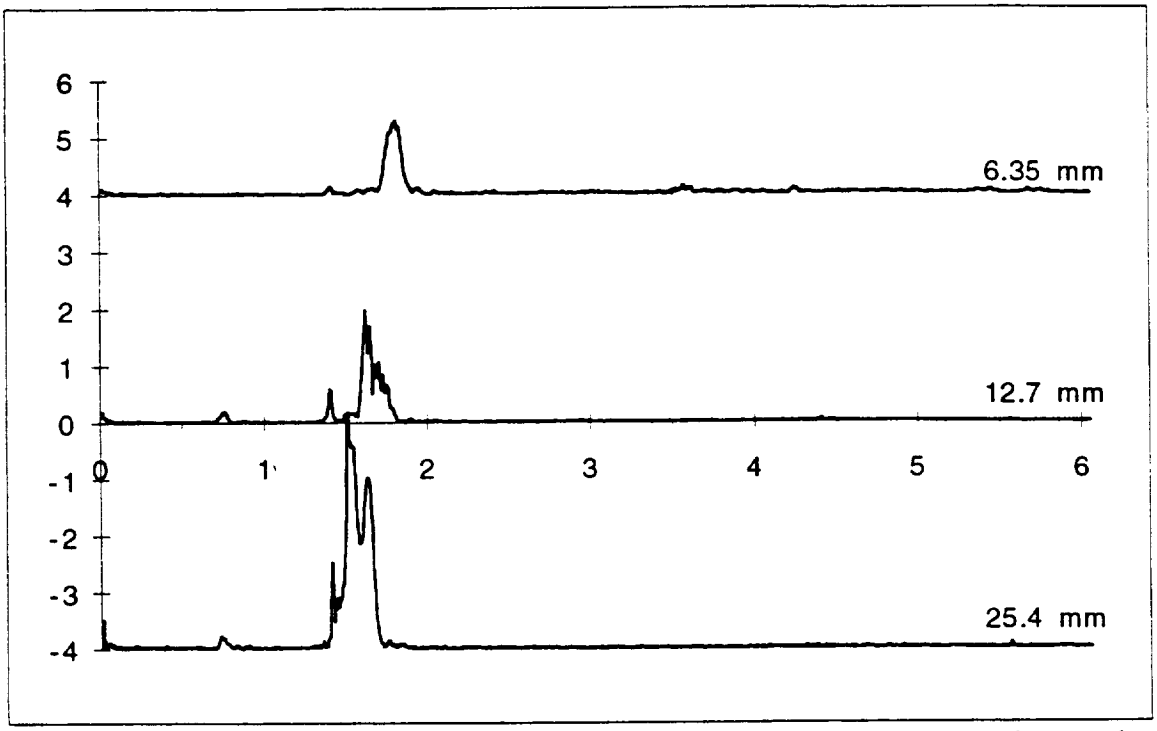

Figure 3.11 Frequency spectra of three experimental signals created by different size transducers at the frequency corresponding to the maximum RF amplitude of each of the transducers. (87 mil plate)

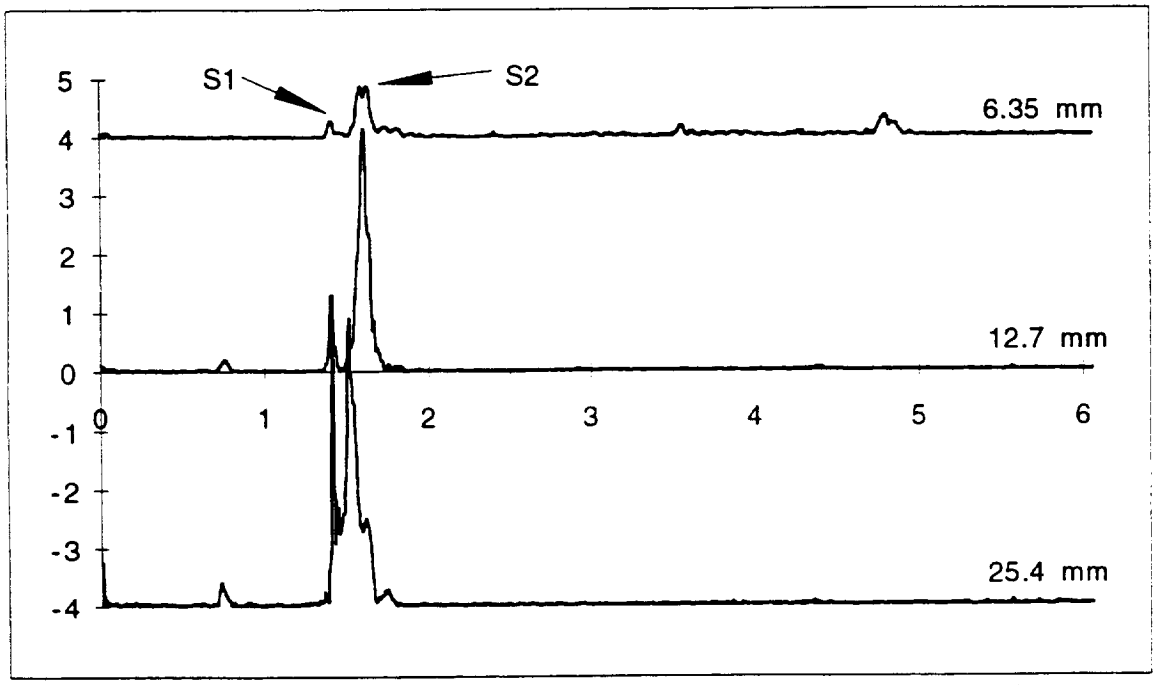

Figure 3.12 Frequency spectra of three experimental signals created by different size transducers at 1.5 MHz (3.35 mm-MHz) on an 87 mil plate. An change in the phase velocity at which the S2 mode is generated explains why the frequency peak associated with it shifts as the size of the transducer is changed. The S1 mode, on the other hand, is generated at the approximately the same phase velocity for all three source sizes so its corresponding frequency peak does not shift.

the change of phase velocity. This shift effect was also noted in anisotropic materials by Rose et al. (1993)

Concluding Thoughts on Power Transmission and Wave Generation

Exciting modes at their cut-off frequencies creates certain limitations. It has already been shown that certain modes exhibit only shear displacements at their cut-off frequencies (Pilarski et al (1993), Auld (1991), Vikortov(1969)). As a result, these modes will not be excited by a normal incidence transducer which only transmits longitudinal waves through the couplant.

Even for modes that are excitable at infinite phase velocities, normal incidence limits the amount of power transmitted, since normally incident waves excite plate waves at high phase velocities. As a result, unless the frequency is near a mode's cut-off frequency, very little energy is transferred to the medium. In addition, there is no directivity associated with a normal incidence transducer. The waves spread symmetrically in all directions, so only a small proportion is seen at the receiver, as opposed to angle beam probes which can direct their energy.

Often, larger transducers will be used to compensate for the loss of power transmission. (A bigger transducer will be able to push more.) However, if the frequency is not correctly chosen, a larger transducer will increase the phase velocity, only "see" the upper portion of the dispersion curves, and actually reduce the proportion of energy transmitted., (as was seen in figures 3.7 and 3.8).

If modes need to be generated at lower phase velocities, a smaller transducer must be used. In order to transfer the same amount of power to the structure as a larger transducer would, various tricks need to be explored. For example, a focusing element and a delay line may be added onto the transducer which could concentrate all of the energy within a smaller diameter. Laser generated ultrasound or special pressure distributions may also be used to concentrate more energy into lower phase velocities.

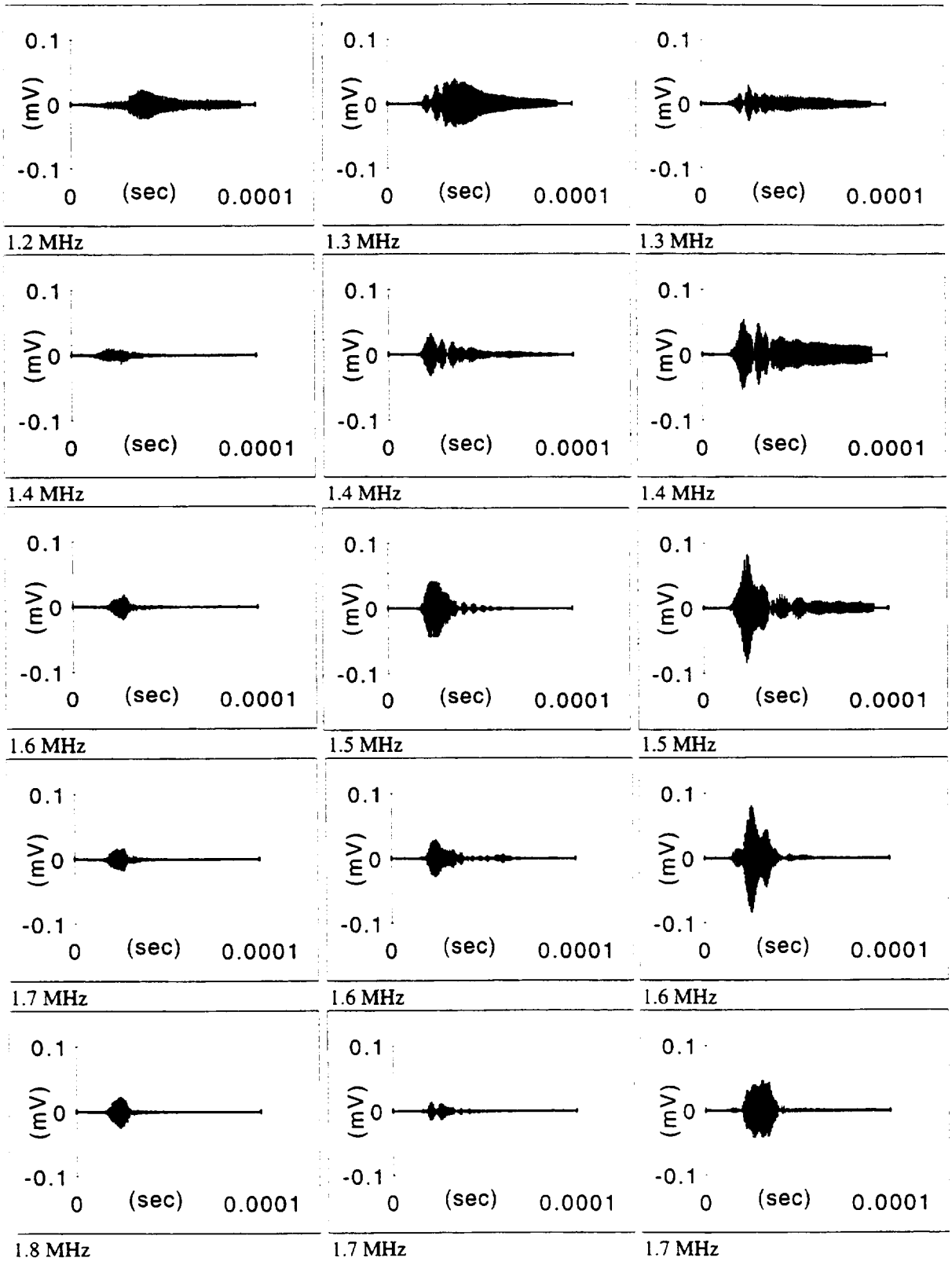

Figure 3.13 Representive experimental RF time-domain waveforms for three different size transducers on an 87 mil Al plate in the region near mode S2's cutoff frequency. The frequencies below each waveform indicate the frequency at which the transducer was driven (using a 20 cycle sine-modulated pulse).

Chapter 4
The Effects of Changing the Plate's Thickness

Lamb waves can only propagate at certain frequencies and phase velocities (Lamb 1917). These modes depend on the resonances formed across the thickness of the plate. By assuming a harmonic time dependence and solving the Rayleigh-Lamb equations, the phase velocity, group velocity, and excitabilities can be determined as functions of the frequency-thickness (fd) product.

However, the frequency-thickness normalization is not valid for finite-size sources. When a finite-size source is taken into account, the Lamb waves become functions of the frequency and the thickness separately instead of their product. As a result, different thickness plates display different excitabilities, interference patterns, and wave shapes, than would be expected if only the fd product was considered.

In a broad sense, the system's change in response is similar to the changes that occur when the size of the transducer is changed. The ratio between the size of the transducer and the thickness of the plate (which is related to the wave's wavelength) strongly influences what interference effects occur and what phase velocity the excited wave has. Increasing the thickness of the plate or shrinking the diameter of the source reduces this ratio and tends to excite waves at lower phase velocities. For waves to only be functions of the frequency-thickness product, the frequency-transducer radius product and the frequency-transducer separation product must also be held constant.

Parallels can be drawn to the effect of changing the transducer size that has already been explained by the simple physical principle that more of the surface is driven directly by a larger transducer, increasing interference effects.

Waves are generated simultaneously from all points on the transducer face. The waves generated by one part of the transducer interfere with those generated elsewhere (by Huygens' Principle). The shorter wavelengths that are associated with a thinner plate will have a much larger phase difference across the transducer face than the longer wavelengths will have. This stronger interference pattern reduces the frequency bandwidth of each peak. In addition, it tends to only excite waves at high phase velocities, since low phase velocities (short wavelengths) will interfere with each other. The only waves that are not interfered with are those which have an infinitely long wavelength, corresponding to an infinite phase velocity. However, as was shown for the size dependence, energy considerations and wave propagation rules cause the value of the excitability to reach a maximum at a certain phase velocity and then decay asymptotically to zero at an infinite phase velocity.

Physical Solution

The solution to the time-harmonic wave propagation problem clearly shows how thicker plates are able to excite waves at lower phase velocities. In this solution, the material response is only a function of the frequency-thickness product. However, when a finite source, instead of an infinite or point source, is considered the solution develops a dependence on the frequency and the thickness separately.

Material Response

As long as the point of observation is far away from the source and the wavenumber term is neglected, the material response is only a function of the fd product as can be seen from the following definition:

$$Material\ Response = \frac{\Gamma}{\Delta'} = \frac{\Gamma^s_{zn}}{\Delta'_s} \tag{4.1}$$

where (taking the symmetric out-of-plane example)

$$\Gamma^s_{zn} = k_{tl}\left\langle (k_{ts}^2 - \xi^2)\sin(k_{ts}d/2)\sin(k_{tl}z) + 2\xi^2\sin(k_{tl}d/2)\sin(k_{ts}z)\right\rangle \tag{4.2}$$

and

$$\begin{aligned}\Delta'_s = \xi(k_{ts}^2 - \xi^2)&\left\langle \begin{matrix} -8\cos(k_{tl}d/2)\sin(k_{ts}d/2) + (k_{ts}^2 - \xi^2) \\ \left\{ {}^{d}\!/_{2k_{tl}}\sin(k_{tl}d/2)\sin(k_{ts}d/2) + {}^{d}\!/_{2k_{ts}}\cos(k_{tl}d/2)\cos(k_{ts}d/2)\right\}\end{matrix}\right\rangle \\ &+ \xi\left\langle 8k_{tl}k_{ts} - 4\xi^2\left(\frac{K_{ts}}{k_{tl}} + \frac{K_{tl}}{k_{ts}}\right)\right\rangle \sin(k_{tl}d/2)\sin(k_{ts}d/2) \\ &+ 2\xi^3\left\langle k_{ts}d\cos(k_{tl}d/2)\cos(k_{ts}d/2) + k_{ts}d\sin(k_{tl}d/2)\sin(k_{ts}d/2)\right\rangle\end{aligned} \tag{4.3}$$

where Δ'_s represents the derivative with respect to the wavenumber of the Rayleigh-Lamb dispersion equation.

By using the following relations, (where c_t is the bulk shear wave speed and c_l is the bulk longitudinal wave speed)

$$\xi = \frac{\omega}{c_{ph}} \qquad k_{tl} = \sqrt{\left(\frac{\omega}{c_l}\right)^2 - \xi^2} \qquad k_{ts} = \sqrt{\left(\frac{\omega}{c_t}\right)^2 - \xi^2} = \omega\sqrt{\left(\frac{1}{c_t}\right)^2 - \left(\frac{1}{v_{ph}}\right)^2} \tag{4.4}$$

it can be shown that the resulting expression is only a function of the fd product (provided z is taken on the top surface (z = d/2).) After canceling fd products, both the gamma functions and the delta prime functions are of the order of ω^3 and the frequency dependence cancels. The value of the material response is shown as a function of the frequency-thickness and phase velocity in figure 2.2.

In the above derivation, for the frequency dependence to cancel, two assumptions are made. The observation point is assumed to be far from the source. This assumption allows the complicated cylindrical wavefront relationship of the wavenumber and phase velocity to be replaced by the relatively simple planar wavefront expression, $\xi = \omega/v_{ph}$. It was also assumed that the

wavenumber term, which was pulled out of the material response, could be neglected. If this term is included with the material response, the combined expression then becomes frequency (and thickness) dependent. However, because of the assumption of planar wavefronts ($\xi = \omega / v_{ph}$), the frequency dependence is not complicated. As long as the frequency-thickness product remains constant, the phase velocity is constant, so the wavenumber becomes linearly proportional to the frequency. The material response-wavenumber term would then also be linearly proportional to the frequency.

Source Influence

When the source and wavenumber terms are added, the displacement equation becomes a function of frequency and thickness separately instead of their product. Mathematically, the source term is given by the Hankel transform of the pressure distribution. For the piston source this becomes:

$$\int_0^{\infty} r f(r) J_0(\xi r) dr = -Pa \frac{J_1(\xi a)}{\xi} \tag{4.5a}$$

where

$$f(r) = \begin{cases} -P & r < a \\ 0 & r > a \end{cases} \tag{4.5b}$$

a is the transducer radius and J_n is the Bessel function of the first kind of order n. The wavenumber term in the Bessel function causes nulls in the simulated frequency response of the source, as seen in figure 4.1. Because the wavenumber is smaller for thicker plates, there are fewer nulls in the 5 mm plate than the 0.2 mm plate. Because there are fewer nulls caused by interference effects across the transducer's face, the shape of the received signal is more similar to the original shape in the thicker plate, as can be seen in figure 4.2.

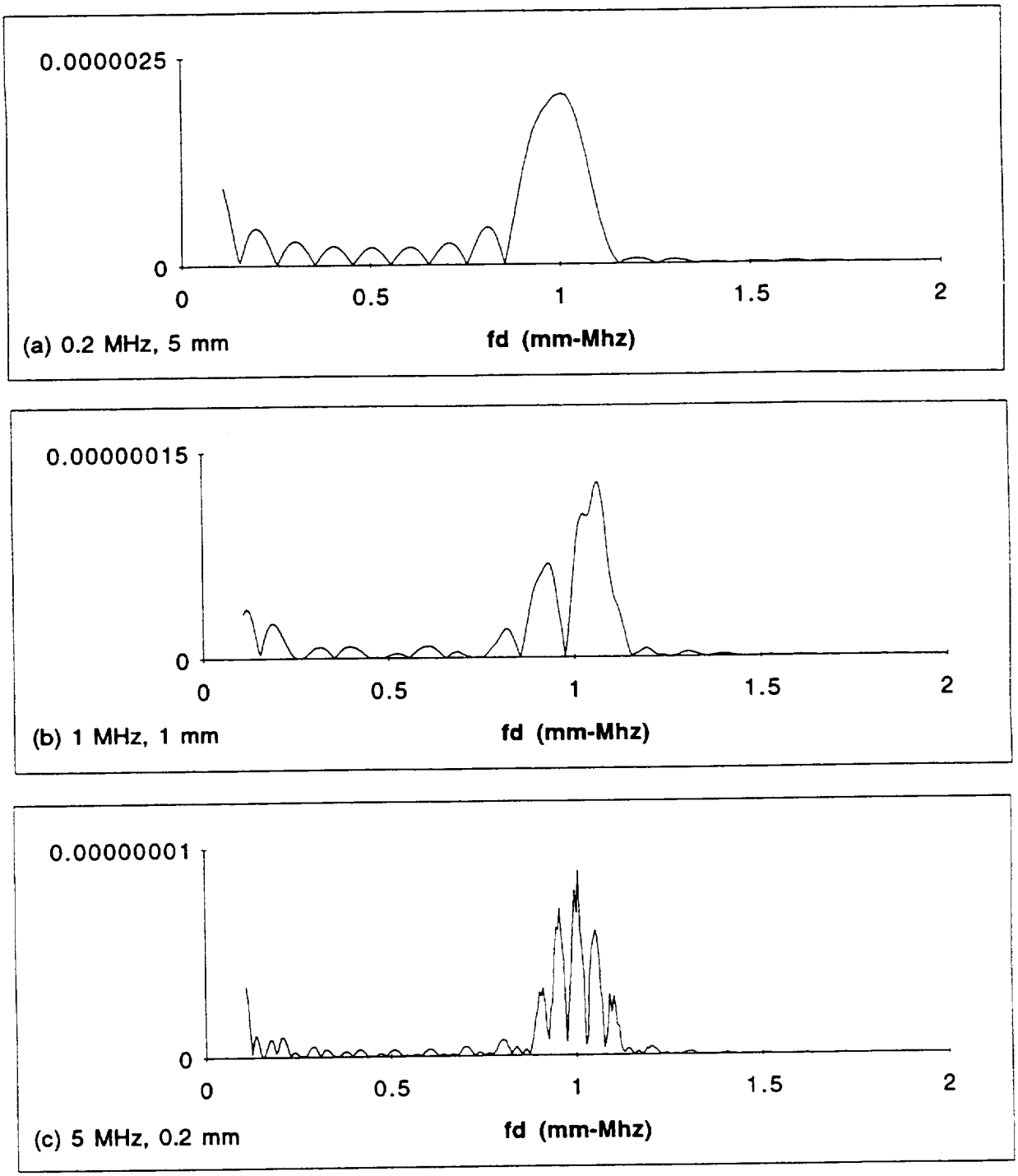

Figure 4.1 Frequency responses from three different frequency simulated transducers, (a) 0.2 MHz (b) 1.0 MHz (c) 5.0 MHz, at fd = 1.0 mm-MHz. The nulls, which are due to interference effects across the face of the transducer, occur more frequently in the frequency spectrums of the higher frequency sources.

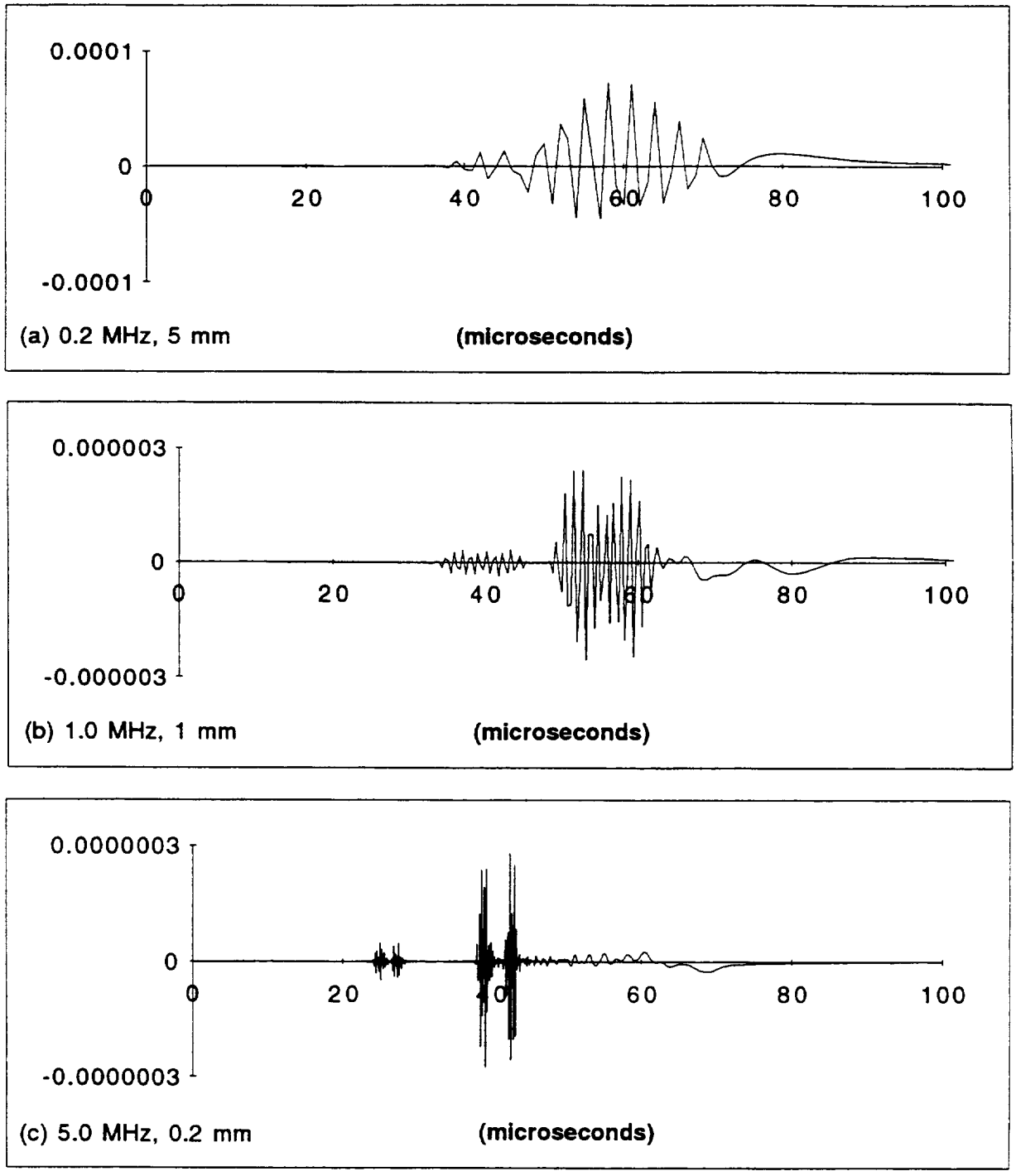

Figure 4.2 Simulated waveforms for three different thickness plates (a) 5 mm (b) 1.0 mm (c) 0.2 mm at fd=1.0 mm-MHz. A 12.7 mm, 10 cycle sine-modulated, piston source was modeled.

Radial Effects and Group Velocity

The radial displacement term ($H_0(\xi r)$ or $H_1(\xi r)$, for out-of-plane and in-plane displacements respectively) is also frequency-dependent. This term comes from the Hankel transform technique and represents the solution of the wave equation in circular cylindrical coordinates. For the same frequency-thickness product, a thinner plate propagates waves with higher wavenumbers since the wavenumber is equal to the circular frequency divided by the phase velocity and the frequency will increase while the phase velocity remains the same. The higher wavenumbers cause the Hankel function to fluctuate more rapidly in space as the transducers are spread apart, corresponding to a higher frequency.

Although the frequency and wavelength of the guided waves change as the thickness does, the group velocities of each mode generated stays approximately the same, as long as the frequency-thickness product (fd) is kept the same. Figure 4.3 shows simulated waveforms that correspond to two, four, and six inch transducer separations for two different thickness plates at fd = 1.0 mm-MHz. The group velocities calculated from these simulated signals are 5.4 mm/μs for the S0 mode and 3.4 mm/μs for the A0 mode. These results agree with the known group velocities for planar wavefronts, which are 5.25 mm/μs for S0 and 3.21 mm/μs for A0. The difference in group velocities can be attributed to mistakes in modeling the material and the assumption that the expression for planar wavefronts could be used.

Experiments confirm the simulated data. Figure 4.4 shows four RF waveforms that were obtained experimentally on two different thickness plates, at the same fd product. The group velocities are nearly the same except that the signal arrives a little earlier for the thicker plate as can be seen in the four inch separation plot (b,d). Figure 4.5 compares the frequency responses of the simulated data and the experimental data. Figures 4.5a and c are experimental

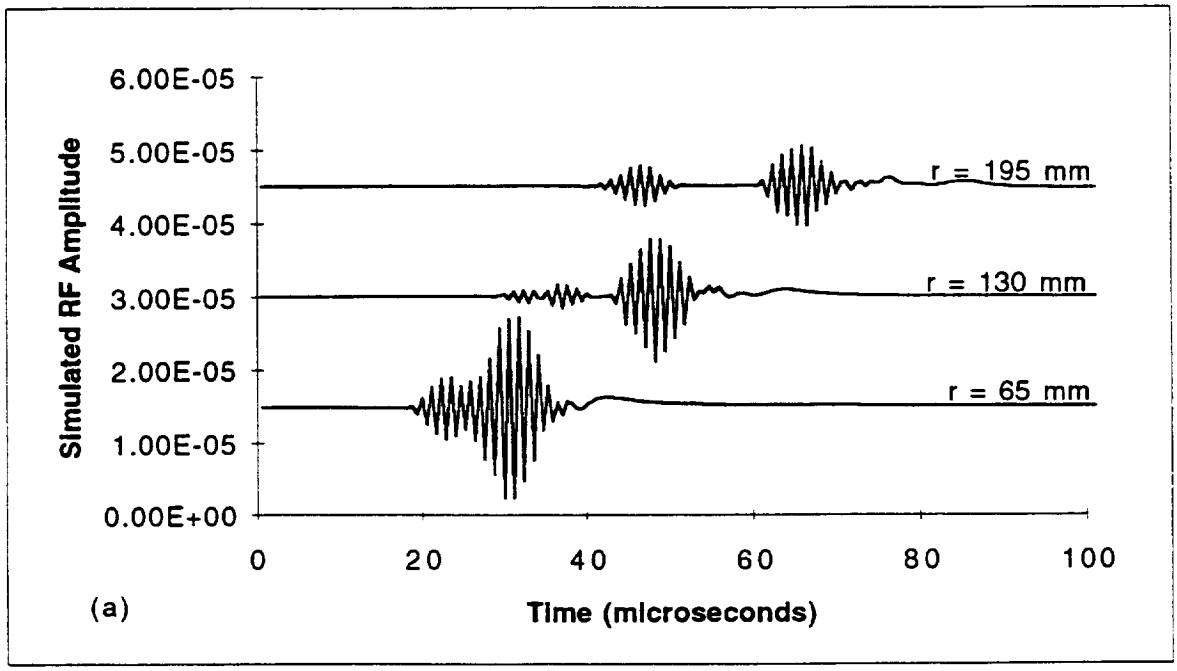

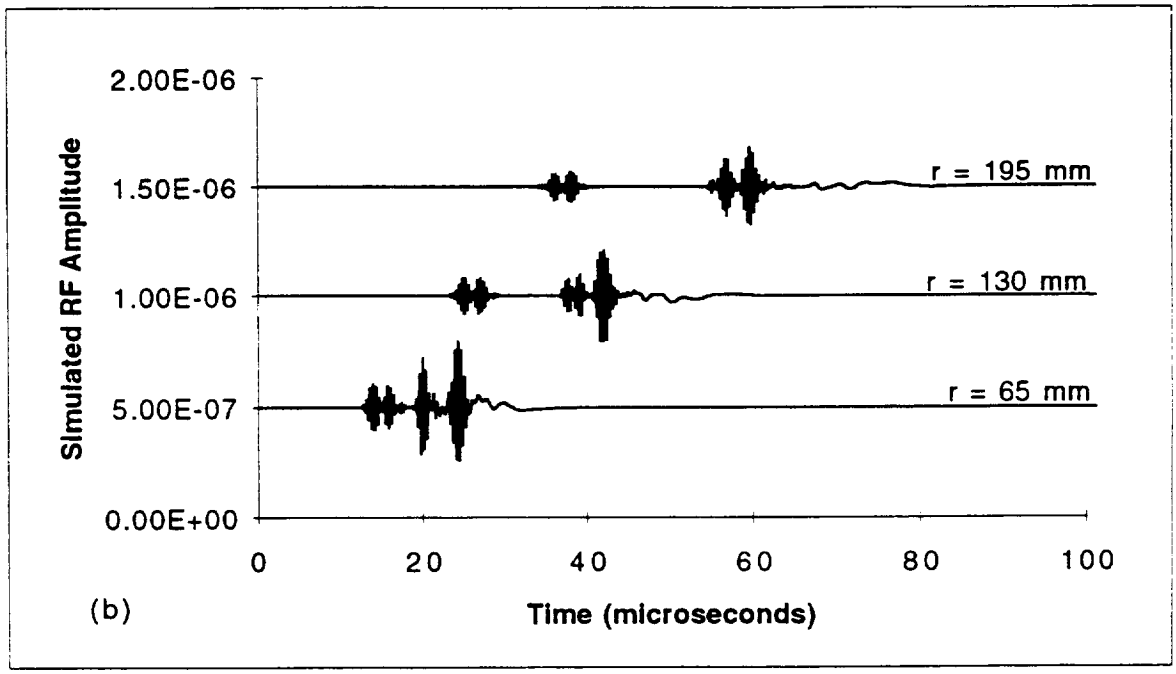

Figure 4.3 Simulated waveforms for two thicknesses of plates, (a) 1.0 mm and (b) 0.33 mm, and three different radial separation distances, 2, 4, and 6 inches. A 12.7 mm, 10 cycle, sine-moduated, parabolic source was simulated at Fd = 1.0 mm-MHz

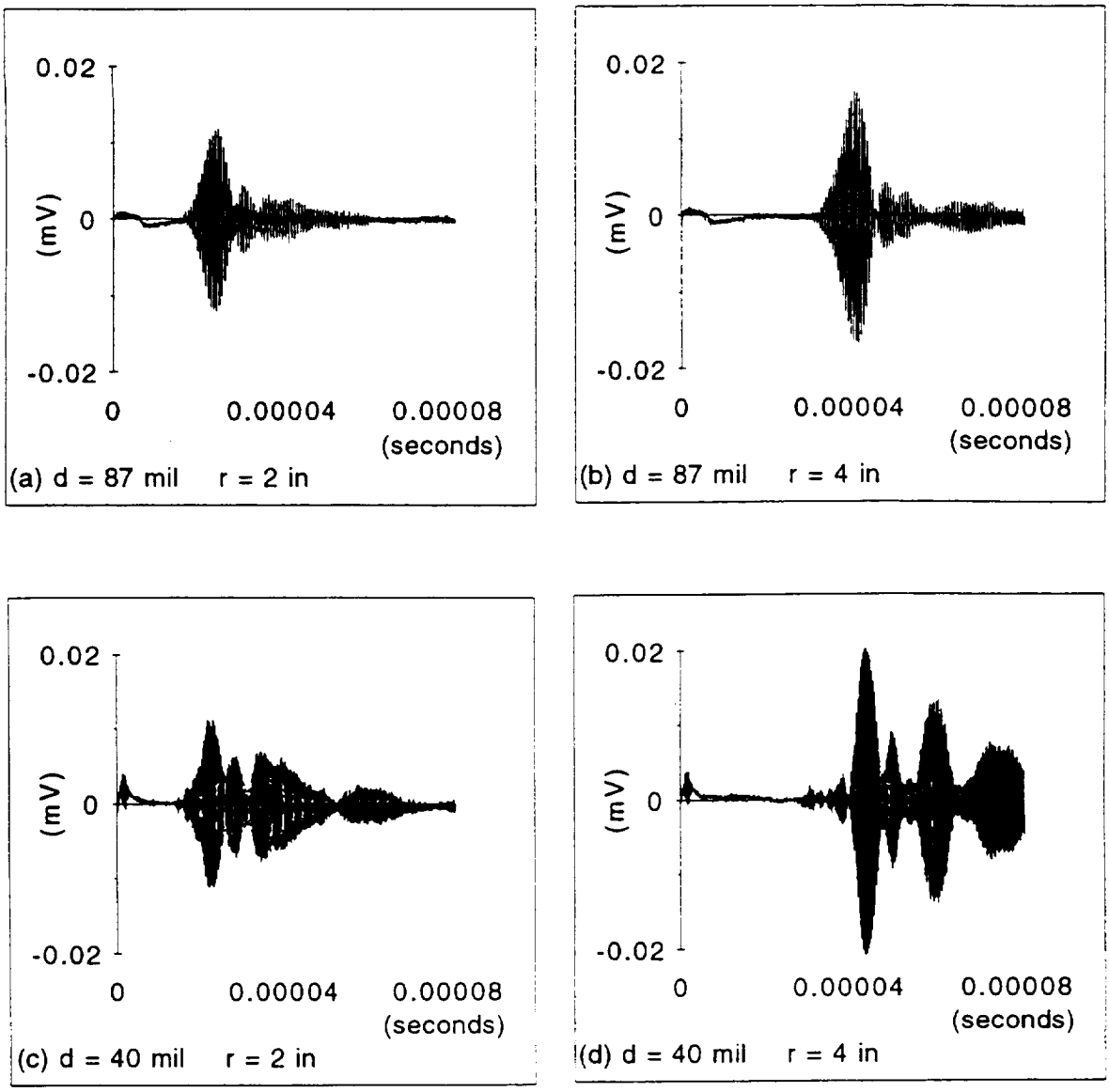

Figure 4.4 Four experimental RF waveforms taken at the same Fd = 3.5 mm-MHz on two thickness plates (40 and 87 mil) and at two separation distances (2 and 4 inches).

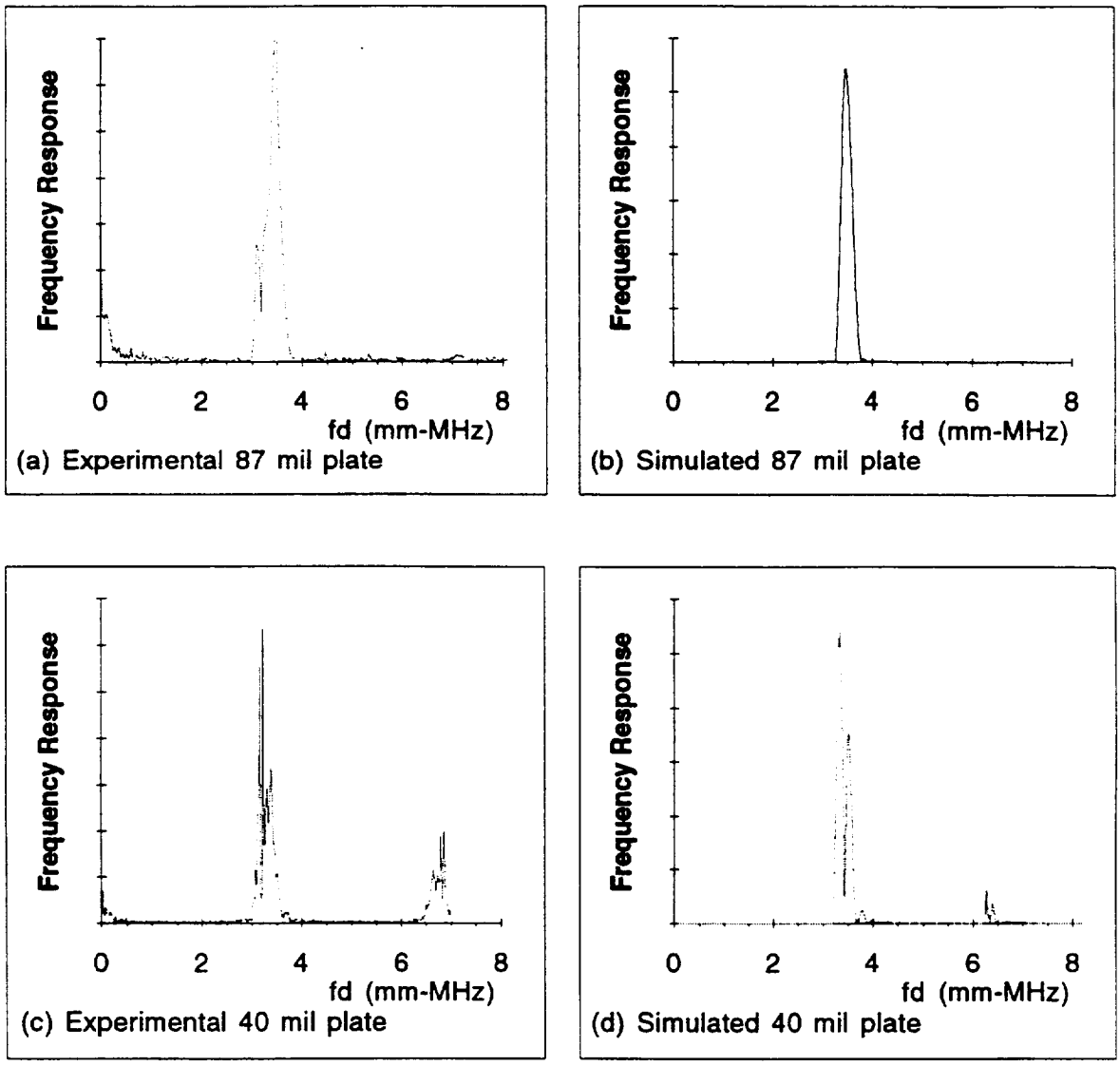

Figure 4.5 Comparison of experimental (a,c) and simulated (b,d) frequency responses for two thickness plates, 87 (a,b) and 40 (c,d) mil, excited at fd=3.5 mm-MHz, by a half inch transducer.

results and figures 4.5b and d are the simulated responses, taking into account the characteristics of the transducer. The general behavior is the same. However, subtle differences near the cutoff frequencies and non-exact models for the pressure distribution and material properties, cause differences, as can also be seen in the simulated time signals in figure 4.6. The experimental data has sharper peaks in the frequency domain (corresponding to generation of waves with higher phase velocities than the simulation could handle) that cause the experimental pulses to be more drawn out than the simulated signals.

Maximum RF Amplitude Profiles

Figure 4.7 represents the maximum RF amplitude that would be generated by a simulated 12.7 mm sine-modulated parabolic source as its center frequency was varied from fd = 1 to fd = 12. The results for a 1, 3, and 5 mm plate are shown. Combining the effects of the source and the material, they demonstrate how the amplitude of the out-of-plane displacement changes with the thickness of the plate.

Several traits of the graphs should be noted. The amplitude of the main peak (S2 fd ≈ 3.2) varies approximately as $1/\xi$ as indicated by the source term for a Parabolic source. Also, the bandwidths of the peaks increase as the thickness increases, as was discussed earlier. A more important physical consideration is the dramatic change in the ratio of the main S2 peak to the other modes which are also excited. In the three and five mm plates (figures 4.7b,c) there is a dramatic increase in the amplitudes of the S0, A0, S1, A1, S4, and A3 modes in comparison to the S2 peak. This indicates that the ratio of the transducer's size to the plate thickness should be kept small, if one these latter modes is desired.

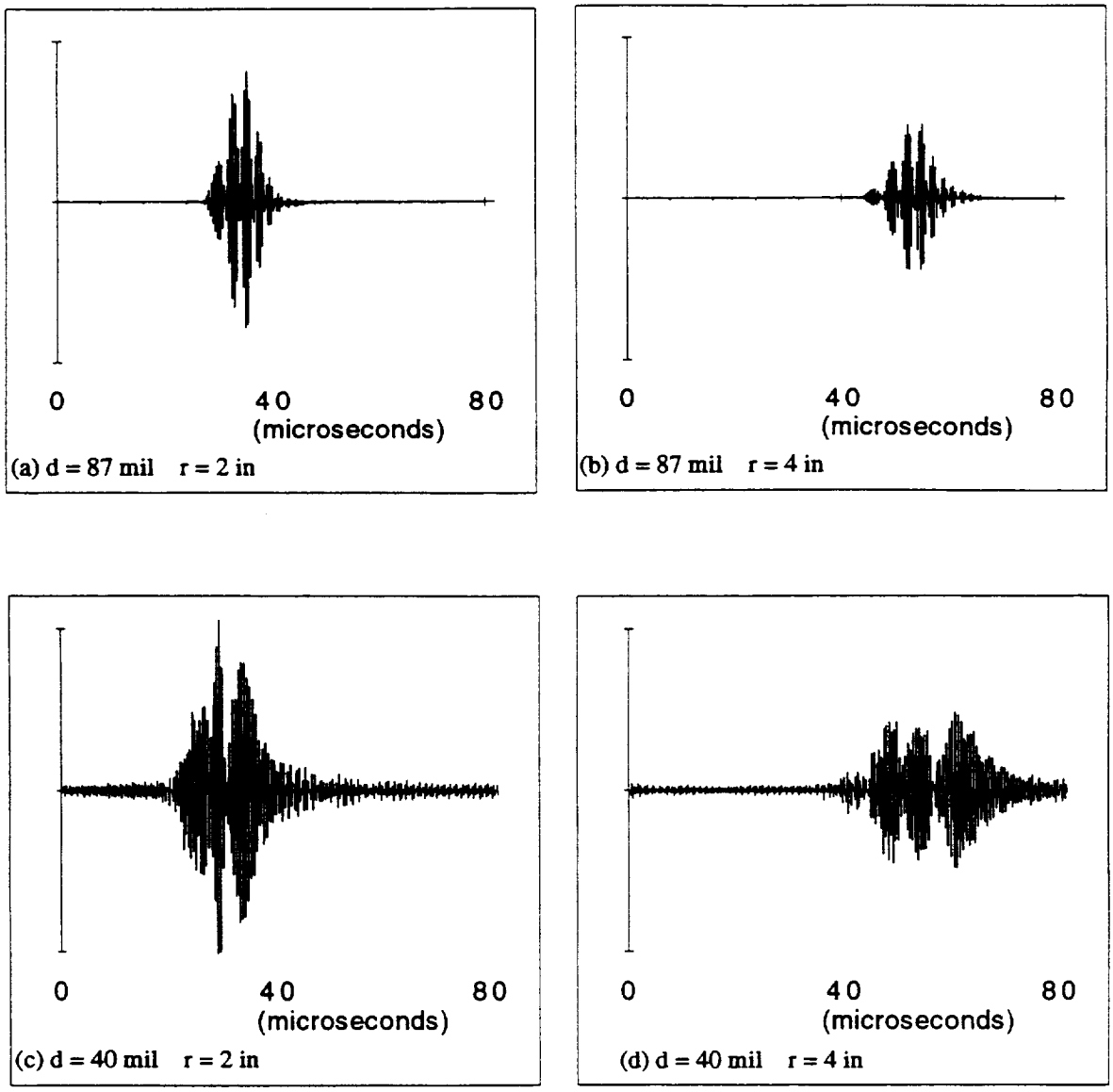

Figure 4.6 Four simulated RF waveforms created at the same fd=3.5 for two thickness plates (40 and 87 mil) and for two separation distances (2 and 4 inches). The signals were created with a half inch piston source, driven by a 20 cycle sine-modulated signal.

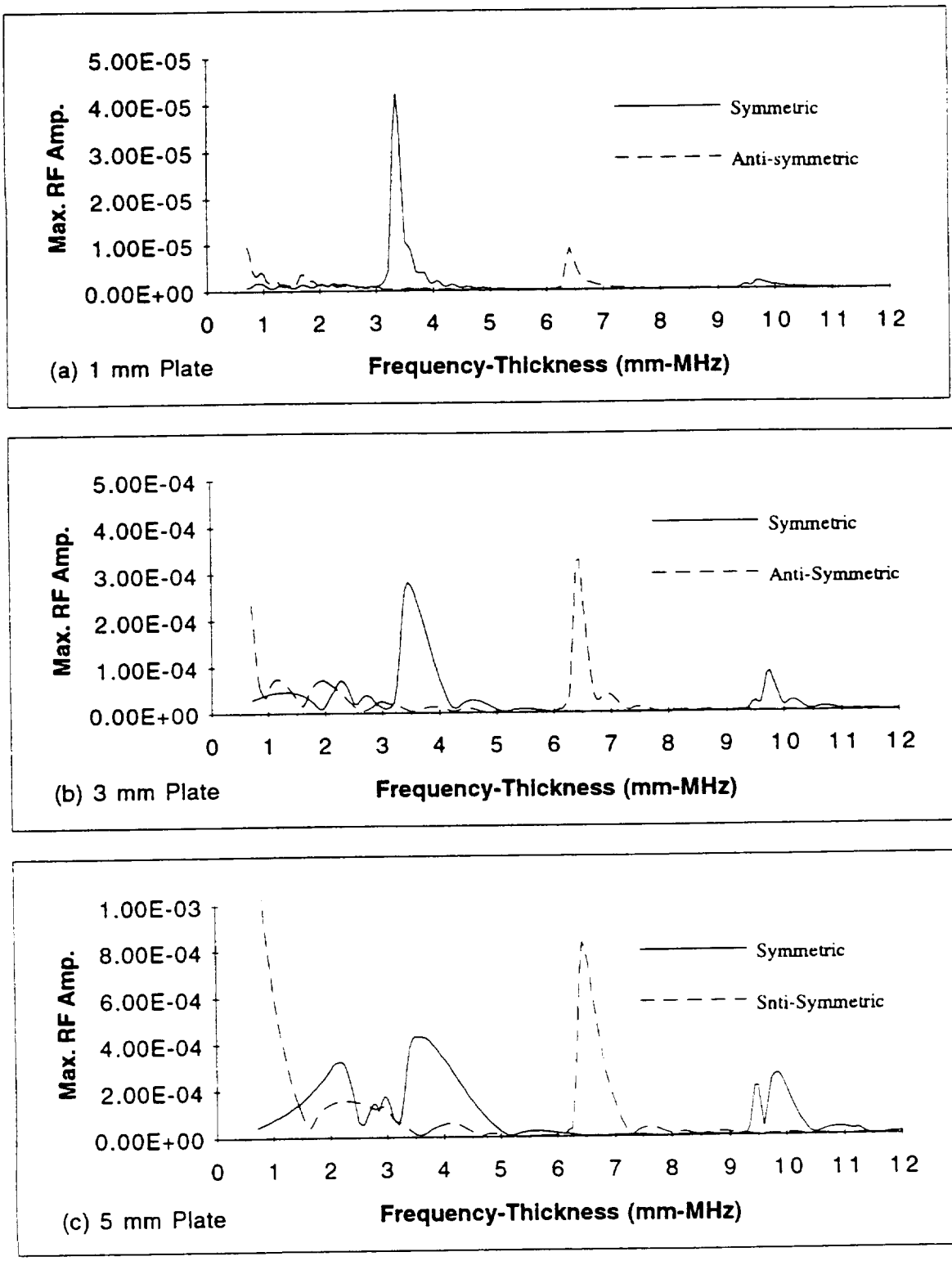

Figure 4.7 Simulated maximum RF amplitude response vs center frequency-thickness for three thickness plates, (a) 1 mm, (b) 3 mm, and (c) 5 mm. (Created for a 12.7 mm parabolic source on an aluminum plate.)

Experimental verification

A half inch, 5.0 MHz center frequency Krautkramer-Branson Gamma transducer was used to generate tone bursts on two different thickness plates (1.016 mm and 2.2352 mm). The results for when the fd product was kept constant at 3.5 mm-MHz (Figure 4.4) were already discussed. Each plate was also swept through a reasonable frequency range and the maximum experimental RF amplitudes were noted. Figure 4.8 shows the comparisons. The general trends are the same. For both the experimental and simulated case, the S2 peak is smaller, narrower , and at a lower frequency in the 40 mil plate.

Figure 4.9 shows a few representative waveforms in the S2 frequency cutoff region. In the 40 mil plate, the waveform, and the underlying wavestructure, is essentially constant throughout the entire region that the plate is very excitable. However, the 87 mil plate is excitable over a much wider range of fd, which allows the experimenter to choose a convenient waveform or wavestructure for the application. Figure 4.10 shows the frequency spectrum corresponding to some of the signals in figure 4.9. The bandwidth of the 87 mil peaks is much larger than the bandwidth of the 40 mil peaks. There is also a much larger change in the location and shape of the frequency spectrum (because a wave will propagate in a wider range of fd's in the thicker plate).

In the Large Thickness Limit

As the thickness increases in relation to the wavelength, the plate begins to act as a semi-infinite half space. The quantities k_{tl} and k_{ts} become large imaginary numbers, which bind the wave the near the surface. In this limit, the Lamb waves superimpose and behave as a single Rayleigh surface wave, which has a constant phase velocity and is consequently non-dispersive. As a result, the maximum RF amplitude becomes constant for all fd and the modes become inseparable. Auld (1990, p.88) gives more information on the Rayleigh wave solution.

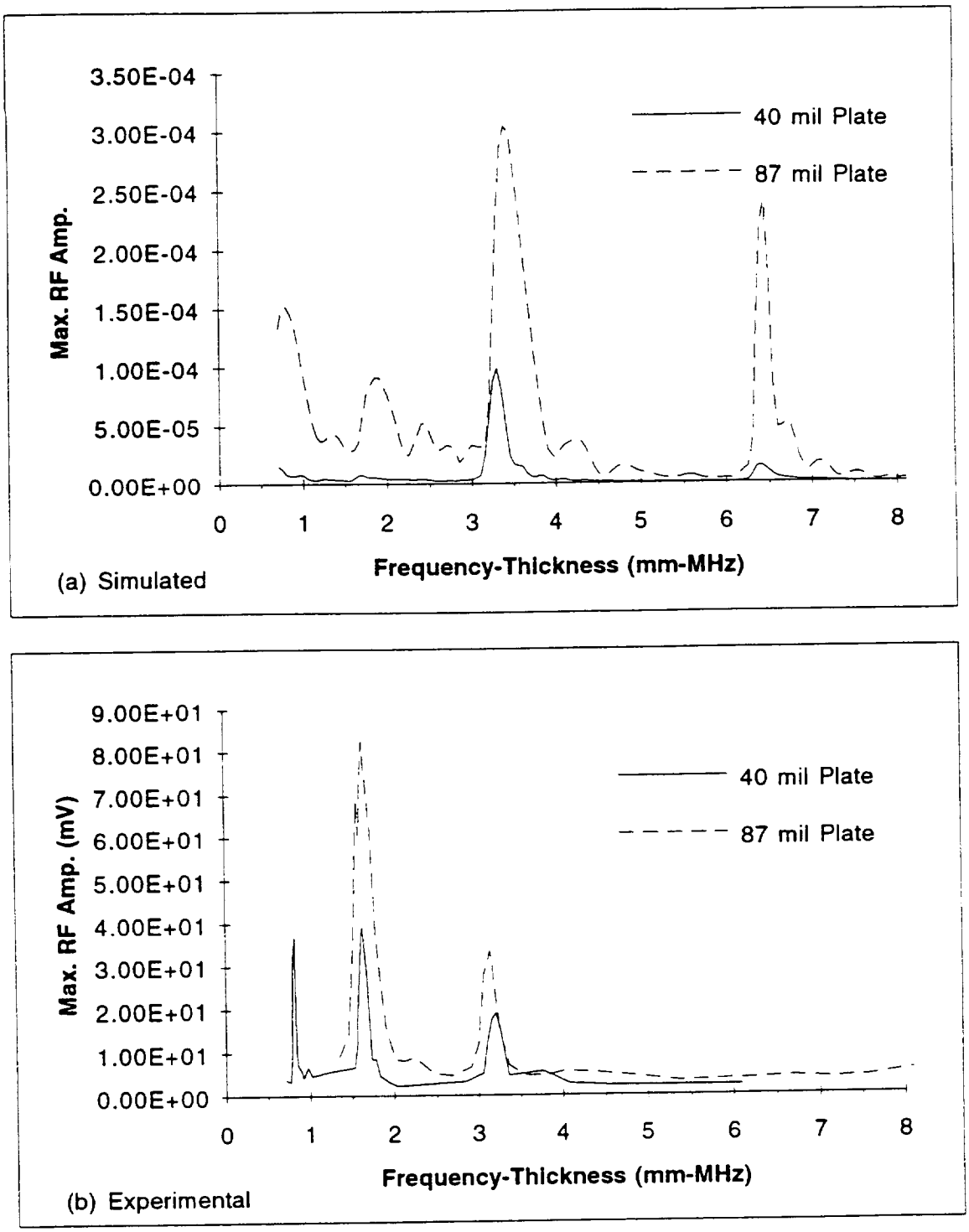

Figure 4.8 The (a) simulated and (b) experimental maximum RF amplitude profiles for two plate thicknesses (for a 12.7 mm parabolic source, 10 cycle sine-modulated signal, sampled two inches from the center of the transmitting transducer on an aluminum plate).

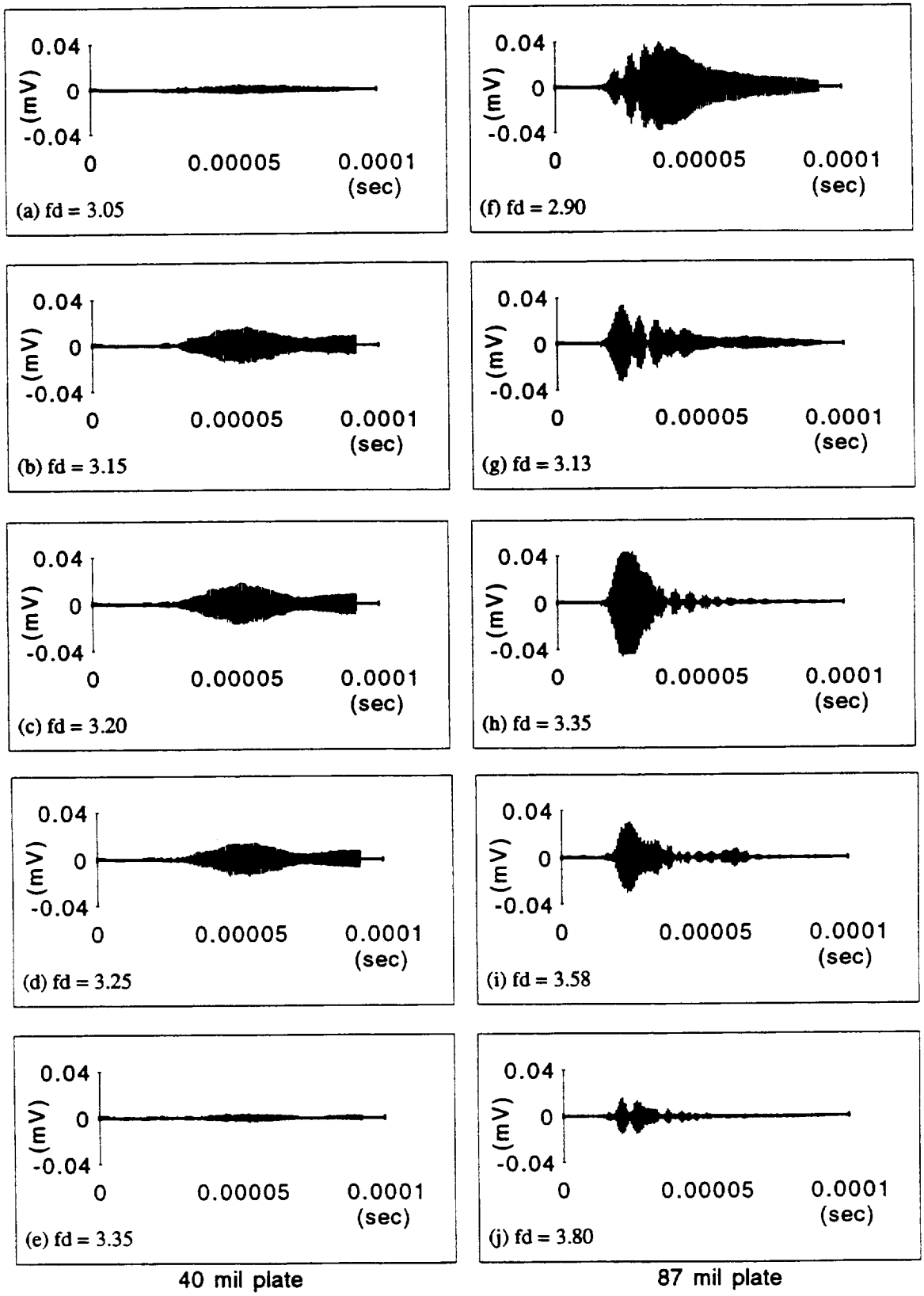

Figure 4.9 Sample experimental waveforms in the region around mode S2's cutoff frequency for two plate thicknesses, 40 mil (a-e) and 87 mil (f-j).

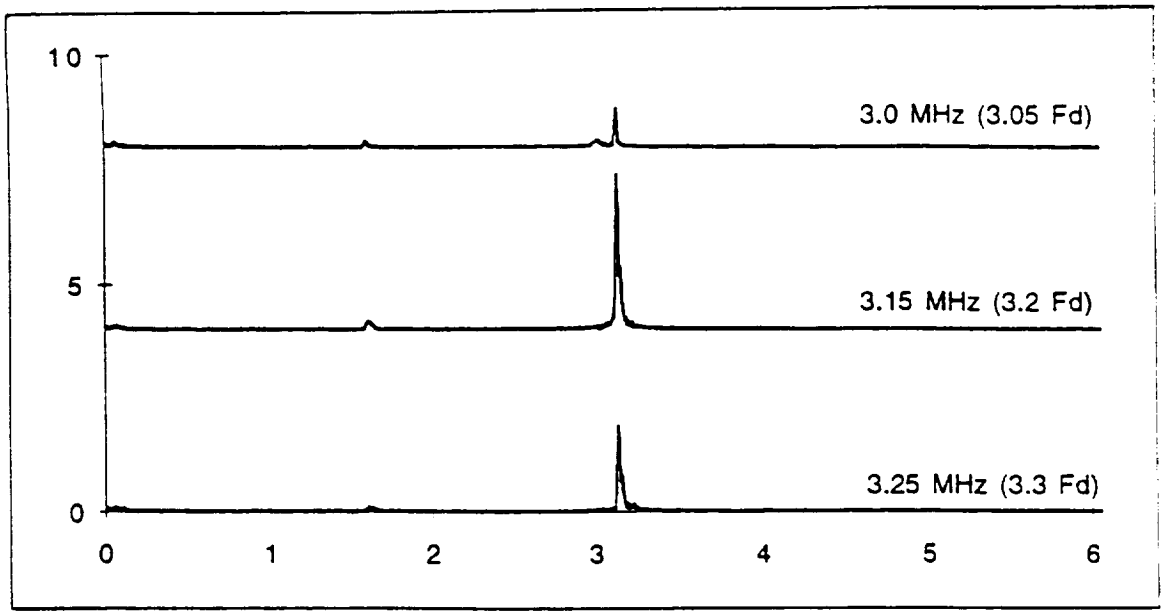

(a) 40 mil plate

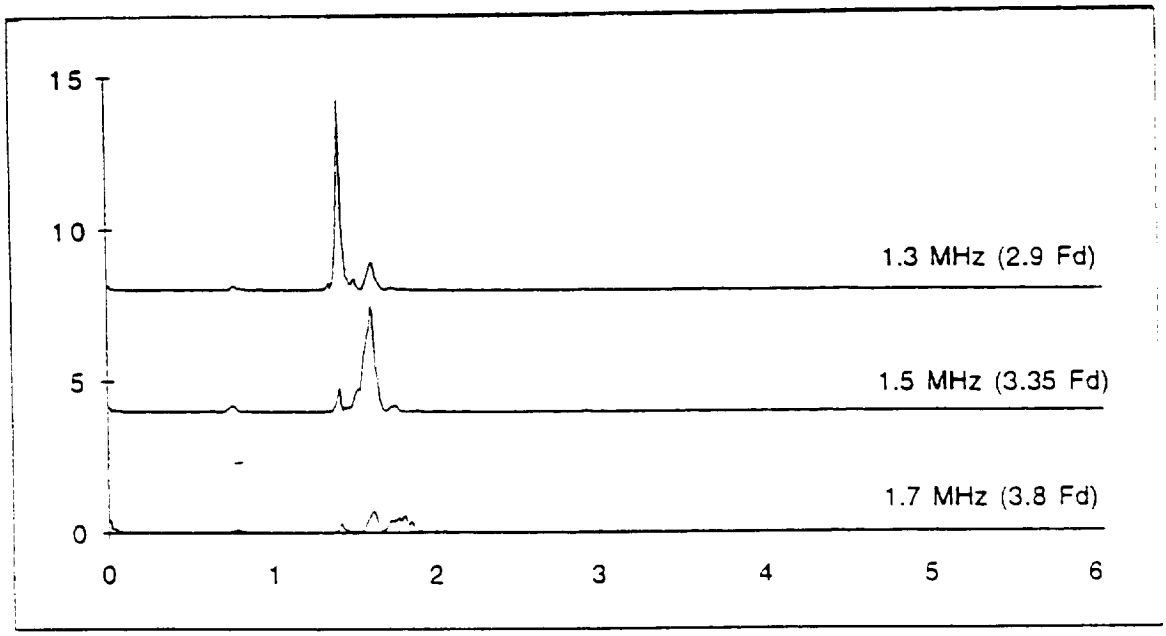

(b) 87 mil plate

Figure 4.10 Frequency spectrums of experimental waveforms sampled on two plate thicknesses, (a) 40 mil and (b) 87 mil, in the region near mode S2's cutoff frequency (fd = 3.2 mm-MHz). The results show that a larger range of frequencies is available for the thicker plate.

Chapter 5
Conclusions and Future Developments

Conclusions

This report explores the effects that a finite axisymmetric source has on wave propagation in Acousto-Ultrasonics. Although it also addresses the effects of the transducer pressure distribution and pulse shape, this work concentrates in two main areas:

- the effect of changing the transducer's diameter, and
- the effect of changing the plate's thickness.

The mathematics of the time harmonic wave propagation solution, the physical principles, and the practical considerations for AU wave generation are explained for both of these areas.

The transducer's diameter affects the phase velocity at which the wave is produced. In general, a larger source excites higher phase velocities. As a result, a larger diameter source narrows and shifts the frequency range over which a large RF amplitude is received especially for the Lamb wave modes that contain only normal displacements at their cutoff frequencies. Because it increases the phase velocity at which a mode is generated, a larger source excites the fundamental modes much less efficiently (and more erratically) than a smaller source. Recognizing this effect allows the size of the transducer to be adapted to optimize the desired application.

A finite source causes the wave solutions to become a function of frequency and thickness independently, instead of being a function of the frequency-thickness product (as they are if it is assumed that a plane wave is incident on the plate). Increasing the plate thickness affects the response in a similar way to reducing the size of transducer, indicating that the ratio of the

transducer diameter to the plate thickness can provide an easy way intuitively determining which phase velocities are preferred. This conclusion also implies that Stress Wave Factors cannot be accurately applied to different thickness specimens without retraining the system first.

Dispersion curves are very useful for indicating what wavestructures are possible in a plate; however, they do not tell the whole story. The source also has a large influence and this influence must be combined with the material response before the wave propagation characteristics and each mode's amplitude can be understood. Because Acousto-Ultrasonics employs the limiting case of normal incidence, the dispersion curves do not provide enough information. The wavestructure of each of the modes, the size and pressure distribution of the transducer, and the plate thickness take on a more important role than they do in angle beam techniques.

Areas Calling for Future Exploration

There are many questions that still need to be answered before Acousto-Ultrasonics can be quantitatively understood. The tools created as a part of this thesis can be used to begin this process.

Stress Wave Factor (SWF) Definitions

Many of the current definitions of the SWF have been created by trial and error, measuring such ambiguous quantities as the number of ringdown counts, the first moment of the frequency spectrum, or simply the ratio of the amplitude of the received signal to the input signal. Such empirical formulas may be significantly affected by parameters other than defects, although they may work well in a single class problem. By providing insight about AU wave propagation and modeling realistic situations, the research begun here should be able to help

create an improved definition of the SWF which is more precise and has a strong physical foundation or at least it will be able to evaluate the numerous SWFs that are used. This standardization and physical basis will allow AU to be expanded to new areas.

Some early ideas for this new definition include a weighted criteria which compares received mode amplitude ratios to those that were sent. Since modes convert as they interact with defect, this should allow for a detailed defect detection and characterization. This research on finite source generation will need to be combined with work on scattering, which is already being explored by researchers such as Alleyne (1992) and Rokhlin (1991), before this problem can be fully addressed.

Anisotropic Material

AU is most commonly used to evaluate composite materials, which can usually be modeled as anisotropic, homogeneous materials. Although the general wave propagation principles that are described in this thesis still apply in anisotropic materials, analytical solutions for anisotropic materials will be needed to study more complex effects, for example skew effects. However, the Hankel transform technique will no longer be able to be used, since it requires axisymmetric properties.

Dispersion Curve Shifts caused by a Finite Source

Wave excitation theory assumes that the Lamb wave dispersion curves are generated at single points on the dispersion curve. However, because all transducers have a finite size, modes are generated over a portion of their dispersion curve. This integration over a portion of the dispersion curve shifts the location of the effective, or experimental, dispersion curve and affects the wave

structure. These changes may turn out to be insignificant, but they definitely need to be studied.

Circular Comb Type Transducer

The Acousto-Ultrasonic technique cannot effectively generate modes at precise phase velocities. Phased array transducers or 'comb' type transducers (which have projections corresponding to the locations of the crests of a wave that is desired) combined with particular pressure distributions may make this possible. A particular mode could be chosen and generated very efficiently, gaining some of the advantages of the angle beam technique while keeping the simplicity of AU.

Laser Generated Ultrasound

Using lasers to generate ultrasonic waves opens up many new possibilities. Lenses can focus the energy into a very small radius or they can reshape the beam to create unusual pressure distributions. In addition, laser ultrasound can create transverse tractions in the plate, as opposed to contact transducers which tend to only create normal tractions. This will open the possibilities for even more modes to be generated.

Better Transducer Model

In this work, a transducer was modeled by an equivalent normal traction. This assumption is not valid for every ultrasonic transducer. A better model, which can adapt to different kinds of transducers, needs to be developed. Without doubt, there needs to be a better model for Laser generated ultrasound before it can be modeled by this technique.

Summary

Before Acousto-Ultrasonics can reach its full potential as a NDE tool, there must be a better understanding of the wave propagation principles that are involved. To address this need, this report studies the effect that the size of the transducer can have on the resulting ultrasonic signal. Many of the Stress Wave Factors that are currently used can be greatly affected by this size effect. This variation causes the results to be inconsisent if the size of the transducer or the thickness of the plate is changed.

Appendix A

The Time Harmonic Solution

In this appendix, the problem of normal incidence pressure loading of a linearly elastic, homogeneous, isotropic layer is studied. The loading is assumed to be time-harmonic and axisymmetric, applied over a circular region of radius a. The solution of this problem was taken from Ditri (1993a), but parts of it may be found elsewhere (for example Pursey (1957), Fulton and Sneddon (1958), Viktorov (1967), and Scott and Miklowitz (1969)).

Problem Formation

The goal of this work is to model the Acousto-Ultrasonic technique applied to in isotropic plates, so that the effects of the size and the pressure distribution of the modeled source can be studied.

Deriving the relevant equations of motion is the first step involved in solving this problem. Euler's equation of motion can be found by applying Newton's second law and the principle of conservation of mass to an arbitrary volume within the elastic solid. This leads to the following relation between the particle displacement field, $\mathbf{u}(\mathbf{r},t)$, and the stress dyadic, $\boldsymbol{\sigma}$,

$$\rho \frac{\partial^2 \mathbf{u}}{\partial t^2} = \nabla \cdot \boldsymbol{\sigma} \tag{A.1}$$

when mass density of the layer, ρ, is assumed to be constant, the material is assumed to be linearly elastic, and body forces (i.e. gravity) are neglected. The generalized Hooke's law then relates the stress dyadic, $\boldsymbol{\sigma}$, to the elastic constants of the material. The theory of elasticity shows that for a homogenous, isotropic material, the 81 possible components of the elastic stiffness tensor reduce to two

material constants, λ and μ, which are called the Lamé constants. In this case, Hooke's law simplifies to

$$\boldsymbol{\sigma} = \lambda \mathbf{I} \nabla \cdot \mathbf{u} + \mu(\nabla \mathbf{u} + \mathbf{u} \nabla) \tag{A.2}$$

Combining equations (A.1) and (A.2) leads to Navier's displacement equation of motion,

$$\mu \nabla \times (\nabla \times \mathbf{u}) + (\lambda + 2\mu) \nabla (\nabla \cdot \mathbf{u}) = \rho \frac{\partial^2 \mathbf{u}}{\partial t^2} \tag{A.3}$$

which is actually a coupled set of three homogeneous partial differential equations, one for each of the displacement field components.

Equations (A.1) - (A.3) describe the behavior of the wave in the bulk material. To model wave propagation in a plate of thickness, d, rectangular and polar cylindrical coordinates are defined as shown in figure A.1 with the mid-plane of the layer corresponding to $z = 0$.

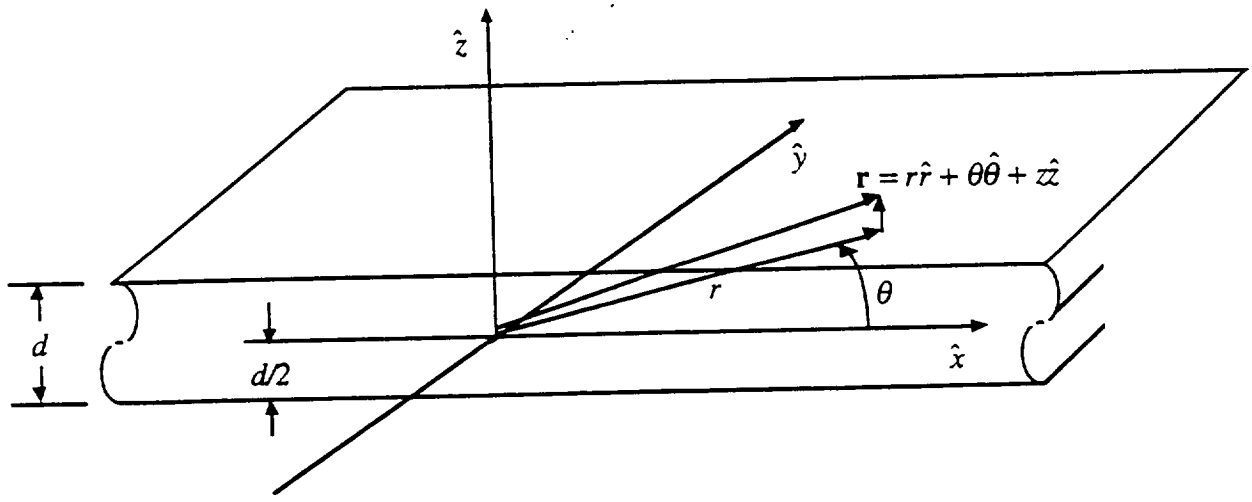

Figure A.1 Cartesian and polar cylindrical coordinates defined for an isotropic, homogeneous layer of thickness d.

This work only considers the case where the upper surface of a layer is subjected to a time-harmonic, axially symmetric traction loading in the circular region $r \equiv \sqrt{x^2 + y^2} < a$, as seen in figure A.2. Because of the axial symmetry of

the problem, the angular transverse traction, $\sigma_{z\theta}$, is identically zero. The boundary conditions on the other two stress components at the surface can be written:

$$\begin{aligned}
&\sigma_{zz}(r,z=d/2,t)=\begin{cases} f(r)e^{-i\omega t} & 0<r<a \\ 0 & r>a \end{cases} \\
&\sigma_{zz}(r,z=-d/2,t)\equiv 0 \\
&\sigma_{rz}(r,z=d/2,t)=\begin{cases} g(r)e^{-i\omega t} & 0<r<a \\ 0 & r>a \end{cases} \\
&\sigma_{rz}(r,z=-d/2,t)\equiv 0
\end{aligned} \tag{A.4}$$

where $f(r)$ is the axial distribution of normal tractions applied to the surface of the layer and $g(r)$ is the distribution of the transverse tractions in the radial direction.

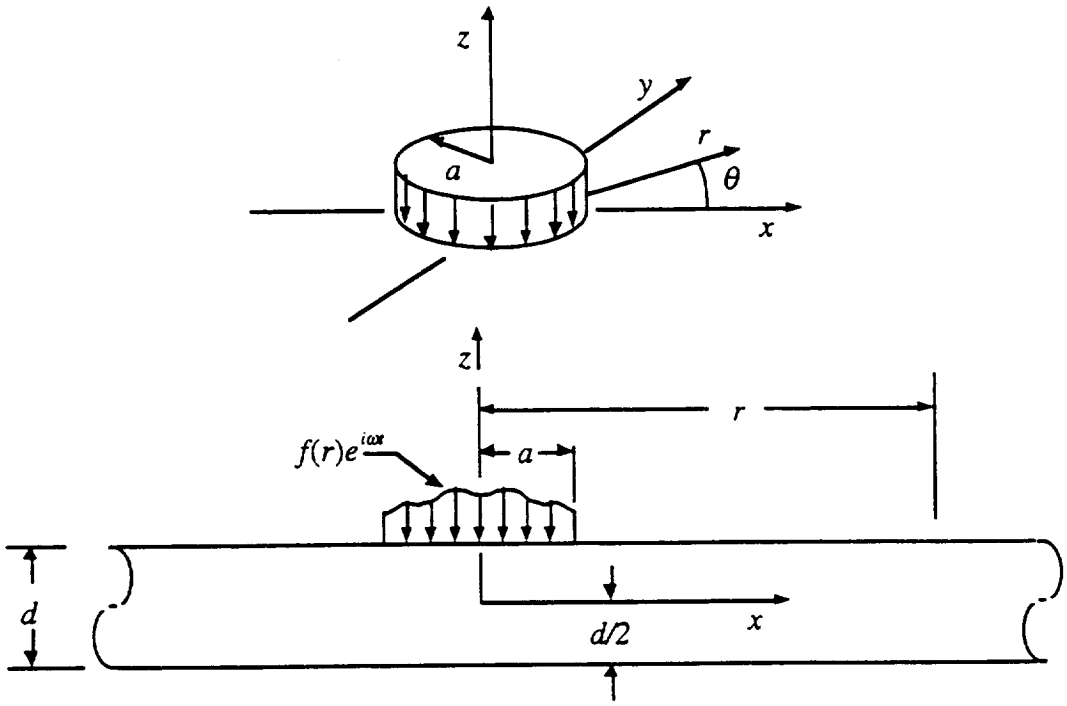

Figure A.2 Upper surface of the layer is subjected to a time-harmonic, axially symmetric traction loading in the circular region $r \equiv \sqrt{x^2+y^2} < a$.

Problem Solution

Uncoupling the Displacement Equations

The displacement field, $\mathbf{u}(\mathbf{r},t)$, can be uncoupled into irrotational and equivoluminal parts by using the Helmholtz decomposition of the elastic displacement field. Thus, the displacement is written

$$\mathbf{u} = \nabla\phi + \nabla \times \Psi, \qquad \nabla \cdot \Psi = 0 \tag{A.5}$$

where ϕ and Ψ are the scalar and vector Helmholtz potentials. Substituting equation (A.5) into Navier's equation of motion (A.3) , and separately taking the divergence and curl of the resulting equation results in the following two equations:

$$\nabla\left[(\lambda + 2\mu)\nabla^2\phi - \rho\frac{\partial^2\phi}{\partial t^2}\right] = 0 \tag{A.6a}$$

and

$$\nabla \times \left[-\mu\nabla \times (\nabla \times \Psi) - \rho\frac{\partial^2\Psi}{\partial t^2}\right] = 0 \tag{A.6b}$$

By requiring that these two equations be applicable for an arbitrary volume within the plate, and using the vector identity,

$$\nabla \times \nabla \times \Psi = \nabla^2\Psi + \nabla(\nabla \cdot \Psi) \tag{A.7}$$

these equations can be rewritten in the more convenient form

$$\nabla^2\phi = \frac{1}{c_L^2}\frac{\partial^2\phi}{\partial t^2} \quad , \quad c_L = \left(\frac{\lambda + 2\mu}{\rho}\right)^{1/2} \tag{A.8a}$$

and

$$\nabla^2\Psi = \frac{1}{c_T^2}\frac{\partial^2\Psi}{\partial t^2} \quad , \quad c_T = \left(\frac{\mu}{\rho}\right)^{1/2} \tag{A.8b}$$

where c_L and c_T represent the longitudinal and shear wave speeds in the bulk material.

Due to the axial symmetry, the displacement field will be independent of angle, θ, and the angular component of the displacement field, u_θ, will vanish. These requirements can be satisfied by setting the 'r' and 'θ' components of the

vector potential, Ψ, equal to zero. Thus, the vector potential can be reduced to a scalar field, $\psi = \psi_z$, the component in the 'z' direction,.

Assuming a harmonic time dependence of $e^{-i\omega t}$, equations (A.8) can be rewritten (in polar cylindrical coordinates),

$$\frac{\partial^2\phi}{\partial r^2}+\frac{1}{r}\frac{\partial\phi}{\partial r}+\frac{\partial^2\phi}{\partial z^2}+\frac{\omega^2}{c_L^2}\phi=0 \tag{A.9a}$$

and

$$\frac{\partial^2\psi}{\partial r^2}+\frac{1}{r}\frac{\partial\psi}{\partial r}-\frac{\psi}{r^2}+\frac{\partial^2\psi}{\partial z^2}+\frac{\omega^2}{c_T^2}\psi=0 \tag{A.9b}$$

Applying the Hankel Transform

Because of the axisymmetric nature of the problem, the Hankel transform provides a convenient way of obtaining a closed-form solution. The Hankel transform and the inverse Hankel transform of order n are defined (for an arbitrary function $b(r)$) as:

$$B^n \equiv \mathcal{H}_n\{b(r)\} = \int_0^\infty rb(r)J_n(\xi r)dr \tag{A.10a}$$

$$b(r) = \mathcal{H}_n^{-1}\left\{B^n(\xi)\right\} = \int_0^\infty \xi B^n(\xi)J_n(\xi r)d\xi \tag{A.10b}$$

where $J_n()$ represents the Bessel function of the first kind of order n. Through integration by parts, it can be shown that,

$$\mathcal{H}_o\left\{\frac{d^2g(r)}{dr^2}+\frac{1}{r}\frac{dg(r)}{dr}\right\} = -\xi^2 G^0(r) \tag{A.11a}$$

and

$$\mathcal{H}_1\left\{\frac{d^2g(r)}{dr^2}+\frac{1}{r}\frac{dg(r)}{dr}-\frac{g(r)}{r^2}\right\} = -\xi^2 G^1(r) \tag{A.11b}$$

as long as $b(r)$ and its derivatives with respect to r vanish at r=0 and in the limit as $r \to \infty$.

Taking advantage of the properties of the equations (A.11), the zero order Hankel transform applied to equation (A.9a) and the first order Hankel transform is applied to equation (A.9b), resulting in ordinary differential equations,

$$\frac{d^2\Phi^0}{dz^2} + \left(k_L^2 - \xi\right)\Phi^0 = 0 \qquad , \qquad k_L = \omega/c_L \tag{A.12a}$$

and

$$\frac{d^2\Psi^1}{dz^2} + \left(k_T^2 - \xi\right)\Psi^1 = 0 \qquad , \qquad k_L = \omega/c_L \tag{A.12b}$$

where ξ is the wavenumber (and the transform parameter) and k_L and k_T are the longitudinal and transverse wavenumbers respectively. The general solution to this set of equations (A.12) is

$$\Phi^0(\xi,z) = A(\xi)\cos(k_{tl}z) + B(\xi)\sin(k_{tl}z) \tag{A.13a}$$

and

$$\Psi^1(\xi,z) = C(\xi)\cos(k_{ts}z) + D(\xi)\sin(k_{ts}z) \tag{A.13b}$$

where $k_{tl}^2 \equiv \left(\omega/c_L\right)^2 - \xi^2$ and $k_{ts}^2 \equiv \left(\omega/c_T\right)^2 - \xi^2$ and A(ξ), B(ξ), C(ξ), and D(ξ) are arbitrary functions of the wavenumber, ξ.

Satisfying the Boundary Conditions

The amplitudes in the general equations (A.13) can be found by satisfying the boundary conditions (traction free except within a circular region of radius a).

The boundary conditions are imposed on the stress components at the surface of the plate and not on the displacement potentials, so the solutions must also be expressed in terms of the potentials. Using equations (A.2), (A.5), and (A.7a), the stress components that appear in the boundary conditions in equations (A.2) can be expressed in terms of the potentials,

$$\sigma_{zz}(r,z) = -\lambda k_L^2\phi + 2\mu\frac{\partial^2\phi}{\partial z^2} + \frac{2\mu}{r}\frac{\partial}{\partial r}\left(r\frac{d\psi}{dz}\right) \tag{A.14a}$$

$$\sigma_{rz}(r,z) = -\mu\left\{2\frac{\partial^2\phi}{\partial r\partial z} + \frac{\partial^2\psi}{\partial r^2} + \frac{1}{r}\frac{\partial\psi}{\partial r} - \frac{\psi}{r} - \frac{\partial^2\psi}{\partial z^2}\right\} \tag{A.14b}$$

Applying the zero order Hankel transform to the expression for σ_{zz} and the first order transform to the expression for σ_{rz} results in,

$$\Sigma_{zz}^{0}(\xi,z) \equiv H^{0}\{\sigma_{zz}\} = -\lambda k_L^2 \Phi^0 + 2\mu \frac{d^2\Phi^0}{dz^2} + 2\mu\xi \frac{d\Psi^1}{dz} \qquad \text{(A.15a)}$$

$$\Sigma_{rz}^{1}(\xi,z) \equiv H^{1}\{\sigma_{rz}\} = -\mu\left\{2\xi \frac{d\Phi^0}{dz} + \xi^2\Psi^1 + \frac{d^2\Psi^1}{dz^2}\right\} \qquad \text{(A.15b)}$$

Applying the same transforms to the boundary conditions (equations (A.4)), yields the following equations:

$$\Sigma_{zz}^{0}(\xi,d/2) = \mathcal{H}_0\{f(r)\} \equiv F^0(\xi) \qquad \text{(A.16a)}$$

$$\Sigma_{zz}^{0}(\xi,-d/2) \equiv 0 \qquad \text{(A.16b)}$$

and

$$\Sigma_{rz}^{1}(\xi,d/2) = \mathcal{H}_1\{g(r)\} \equiv G^1(\xi) \qquad \text{(A.16c)}$$

$$\Sigma_{rz}^{1}(\xi,-d/2) \equiv 0 \qquad \text{(A.16d)}$$

Substituting the general forms of the transformed potentials, equations (A.13), into the formulas for the transformed traction components, equations (A.15), and imposing the transformed boundary conditions, equations (A.16), on the resulting expressions, results in four linear homogeneous equations in the four unknown amplitudes, A(ξ), B(ξ), C(ξ), and D(ξ), which can be written in matrix form as,

$$[\mathcal{A}]\begin{bmatrix} A \\ B \\ C \\ D \end{bmatrix} = \begin{bmatrix} F^0 \\ 0 \\ G^1 \\ 0 \end{bmatrix} \qquad \text{(A.17a)}$$

where $[\mathcal{A}]$ is given by:

$$\begin{bmatrix} -\mu\left(k_{ts}^2-\xi^2\right)\cos(k_{tl}\,d/2) & -\mu\left(k_{ts}^2-\xi^2\right)\sin(k_{tl}\,d/2) & -2\mu\xi k_{ts}\sin(k_{ts}\,d/2) & 2\mu\xi k_{ts}\cos(k_{ts}\,d/2) \\ -\mu\left(k_{ts}^2-\xi^2\right)\cos(k_{tl}\,d/2) & \mu\left(k_{ts}^2-\xi^2\right)\sin(k_{tl}\,d/2) & 2\mu\xi k_{ts}\sin(k_{ts}\,d/2) & 2\mu\xi k_{ts}\cos(k_{ts}\,d/2) \\ 2\mu\xi k_{tl}\sin(k_{tl}\,d/2) & -2\mu\xi k_{tl}\cos(k_{tl}\,d/2) & \mu\left(k_{ts}^2-\xi^2\right)\cos(k_{ts}\,d/2) & \mu\left(k_{ts}^2-\xi^2\right)\sin(k_{ts}\,d/2) \\ -2\mu\xi k_{tl}\sin(k_{tl}\,d/2) & -2\mu\xi k_{tl}\cos(k_{tl}\,d/2) & \mu\left(k_{ts}^2-\xi^2\right)\cos(k_{ts}\,d/2) & -\mu\left(k_{ts}^2-\xi^2\right)\sin(k_{ts}\,d/2) \end{bmatrix} \qquad \text{(A.17b)}$$

The determinant of $[\mathcal{A}]$ can be expressed in the form,

$$\left\|[\mathcal{A}]\right\| = 4\mu^4 \Delta_a \Delta_s \tag{A.18}$$

where (using the relation $\lambda k_L^2 + 2\mu k_{tl}^2 = \mu\left(k_{ts}^2 - \xi^2\right)$),

$$\Delta_s \equiv \left(k_{ts}^2 - \xi^2\right)^2 \cos(k_{tl}\, d/2)\sin(k_{ts}\, d/2) + 4\xi^2 k_{tl} k_{ts} \sin(k_{tl}\, d/2)\cos(k_{ts}\, d/2) \tag{A.19}$$

represents the dispersion function for straight crested symmetric Lamb waves in a free layer, and

$$\Delta_a \equiv \left(k_{ts}^2 - \xi^2\right)^2 \sin(k_{tl}\, d/2)\cos(k_{ts}\, d/2) + 4\xi^2 k_{tl} k_{ts} \cos(k_{tl}\, d/2)\sin(k_{ts}\, d/2) \tag{A.20}$$

represents the dispersion function for straight crested anti-symmetric Lamb waves in a free layer. The dispersion curves can be generated by setting equations (A.19) and (A.20) equal to zero and solving for the real roots. Even though the plate contains circularly crested waves, straight crested Lamb wave dispersion equations are expected because the dispersion equations represent resonant effects across the thickness of the plate, in the 'z' coordinate, which is the same for both Cartesian or cylindrical coordinates systems.

The system of four equations (A.17) can be solved using Cramer's rule, leading to the following values for the unknown amplitudes:

$$A(\xi) = \frac{\mathcal{A}_{14}(\xi)G^1(\xi) - \mathcal{A}_{34}(\xi)F^o(\xi)}{2\mu^2 \Delta_s(\xi)} \tag{A.21a}$$

$$B(\xi) = \frac{\mathcal{A}_{13}(\xi)G^1(\xi) - \mathcal{A}_{33}(\xi)F^o(\xi)}{2\mu^2 \Delta_a(\xi)} \tag{A.21b}$$

$$C(\xi) = \frac{\mathcal{A}_{32}(\xi)F^o(\xi) - \mathcal{A}_{12}(\xi)G^1(\xi)}{2\mu^2 \Delta_a(\xi)} \tag{A.21c}$$

$$D(\xi) = \frac{\mathcal{A}_{31}(\xi)F^o(\xi) - \mathcal{A}_{11}(\xi)G^1(\xi)}{2\mu^2 \Delta_s(\xi)} \tag{A.21d}$$

where $\mathcal{A}_{ij}$ are the elements of the matrix, $\mathcal{A}$.

Applying the Inverse Hankel Transform

Substituting the calculated amplitudes for A, B, C, and D (equations (A.21)) into the transformed potentials, equations (A.15), and applying the inverse Hankel transforms of the appropriate orders, gives formal solutions for the two Helmholtz potentials,

$$\phi(r,z) = \int_0^\infty \frac{\mathcal{A}_{14}(\xi)G^1(\xi) - \mathcal{A}_{34}(\xi)F^o(\xi)}{2\mu^2\Delta_s(\xi)}\cos(k_{tl}z)J_0(\xi r)\xi d\xi + \int_0^\infty \frac{\mathcal{A}_{13}(\xi)G^1(\xi) - \mathcal{A}_{33}(\xi)F^o(\xi)}{2\mu^2\Delta_a(\xi)}\sin(k_{tl}z)J_0(\xi r)\xi d\xi \tag{A.22a}$$

and

$$\psi(r,z) = \int_0^\infty \frac{\mathcal{A}_{32}(\xi)F^o(\xi) - \mathcal{A}_{12}(\xi)G^1(\xi)}{2\mu^2\Delta_a(\xi)}\cos(k_{ts}z)J_1(\xi r)\xi d\xi + \int_0^\infty \frac{\mathcal{A}_{31}(\xi)F^o(\xi) - \mathcal{A}_{11}(\xi)G^1(\xi)}{2\mu^2\Delta_s(\xi)}\sin(k_{ts}z)J_1(\xi r)\xi d\xi \tag{A.22b}$$

The potentials in equations (A.22) can be broken into "symmetric" and "anti-symmetric" potentials,

$$\phi(r,z) = \phi^s(r,z) + \phi^a(r,z) \tag{A.23a}$$

$$\psi(r,z) = \psi^s(r,z) + \psi^a(r,z) \tag{A.23b}$$

The superscripts refer to whether the displacements associated with the potentials are symmetric (the integrals with $\Delta_s(\xi)$ in their denominator) or anti-symmetric (the integrals with $\Delta_a(\xi)$ in their denominator) with respect to the mid-plane of the layer.

The Helmholtz decomposition equation (A.5) can be used to express the particle displacements in terms of the potentials. These displacements can be broken into their in-plane, '*r*', and out-of-plane, '*z*', components,

$$u_r^{s,a}(r,z) = \frac{\partial\phi^{s,a}}{\partial r} - \frac{\partial\psi^{s,a}}{\partial z} \tag{A.24a}$$

$$u_z^{s,a}(r,z) = \frac{\partial\phi^{s,a}}{\partial z} + \frac{\psi^{s,a}}{r} + \frac{\partial\psi^{s,a}}{\partial r} \tag{A.24b}$$

After differentiating under the integrals in equations (A.22) and performing the necessary algebra, the following equations are found for the particle displacement fields:

$$u_r^s(r,z) = \int_0^\infty \frac{\Gamma_{rt}^s(k_{ts},k_{tl}\xi)G^1(\xi) + \Gamma_{rn}^s(k_{ts},k_{tl}\xi)F^0(\xi)}{2\mu\Delta_s(k_{ts},k_{tl}\xi)} J_1(\xi r)\xi d\xi$$

$$u_z^s(r,z) = \int_0^\infty \frac{\Gamma_{zt}^s(k_{ts},k_{tl}\xi)G^1(\xi) + \Gamma_{zn}^s(k_{ts},k_{tl}\xi)F^0(\xi)}{2\mu\Delta_s(k_{ts},k_{tl}\xi)} J_0(\xi r)\xi d\xi$$

$$u_r^a(r,z) = \int_0^\infty \frac{\Gamma_{rt}^a(k_{ts},k_{tl}\xi)G^1(\xi) + \Gamma_{rn}^a(k_{ts},k_{tl}\xi)F^0(\xi)}{2\mu\Delta_a(k_{ts},k_{tl}\xi)} J_1(\xi r)\xi d\xi \qquad \text{(A.25 a-d)}$$

$$u_z^a(r,z) = \int_0^\infty \frac{\Gamma_{zt}^a(k_{ts},k_{tl}\xi)G^1(\xi) + \Gamma_{zn}^a(k_{ts},k_{tl}\xi)F^0(\xi)}{2\mu\Delta_a(k_{ts},k_{tl}\xi)} J_0(\xi r)\xi d\xi$$

The $\Gamma_{\alpha\beta}^{s,a}$ functions are defined in both the appendix of Ditri (1993a) and in Appendix B of this thesis. The subscript alpha refers to whether the function belongs to the '*r*' or '*z*' components, and the beta refers to the whether the function relates the displacement to normal or transverse tractions.

Normal Pressure Loading

The Acousto-Ultrasonic technique generally uses normal incidence longitudinal wave transducers, which tend to apply only normal tractions to the plate surface because shear stresses cannot be transmitted across the oil film that AU typically uses as a couplant. As a result, although equation (A.25) is valid for both normal and transverse traction loading, only the normal case will be examined in detail.

One possible model of the pressure distribution is the "piston" example, which represents a uniform normal pressure distribution across the face of the transducer, thus

$$f(r) = \begin{cases} -P, & r < a \\ 0, & r > a \end{cases} \qquad \text{(A.26a)}$$

and

$$g(r) \equiv 0 \qquad \text{(A.26b)}$$

Taking the transforms of these loading functions results in

$$F^0(\xi) = -Pa\frac{J_1(\xi a)}{\xi} \tag{A.27a}$$

and

$$G^1(\xi) \equiv 0 \tag{A.27b}$$

Contour Integration

Through contour integration, residue calculus can be used to evaluate the infinite integrals in equation (A.25), provided the integrand vanishes as $\xi \to 0$ on the large semicircle enclosing the upper half plane, the function has an exponential component $e^{i\xi}$ and the equation is defined for all real ξ. As they are, equations (A.25) do not satisfy these requirements. However, if the substitutions,

$$J_0(z) = \tfrac{1}{2}\left[H_0^{(1)}(z) - H_0^{(1)}(z)(ze^{i\pi})\right] \tag{A.28a}$$

and

$$J_1(z) = \tfrac{1}{2}\left[H_1^{(1)}(z) + H_1^{(1)}(z)(ze^{i\pi})\right] \tag{A.28a}$$

are made, each of the integrals can be rewritten in one of two forms (after making the change of variable from -z to z where appropriate),

$$I_1 = \int_{-\infty}^{\infty} \chi_1(\xi) H_0^{(1)}(\xi r) d\xi \qquad I_2 = \int_{-\infty}^{\infty} \chi_2(\xi) H_1^{(1)}(\xi r) d\xi \tag{A.29}$$

where $H_n^{(1)}$ represents the Hankel function of the first kind of order $n.$, χ_1 is and odd function of ξ, and χ_2 is and even function of ξ..

With this substitution, coutour integration is now possible and the integrands behave as $e^{i\xi r}/\xi^2$ $\xi r >> 1$. However, the poles associated with propagating waves fall on the real axis, which leads to a standing wave solution since the solution physically consists of both incoming and outgoing waves. A small amount of material attenuation, which is set to zero after the integration, is added by allowing the wavenumber to become complex, $\xi = \sigma + i\tau$. Adding a small imaginary component, τ, to the wave number causes the location of the

poles to be shifted from the real axis, so that only incoming or outgoing waves are included in a half-plane contour. To ensure outgoing waves (for the $e^{-i\omega t}$ time dependence), the poles that were shifted from the negative real axis are chosen.

Except at $\xi_{s,a}$=0, all these poles are simple poles which simply occur at the roots of the Rayleigh-Lamb frequency equation, $\xi_{s,a}$. As cutoff frequencies are approached, the wavenumber tends to zero and the Hankel function tends to behave in the following manner:

$$H_0^{(1)} \approx i\frac{2}{\pi}\log(\xi r) \quad \text{and} \quad H_1^{(1)} \approx i\frac{2}{\pi}\left(\frac{2}{\xi r}\right) \qquad \text{(A.30a,b)}$$
$$\xi r \to 0 \qquad\qquad \xi r \to 0$$

indicating that the singularity as $\xi \to 0$ may not be a simple pole. However, further research is needed to determine the nature of the this singularity, so in this solution it is assumed that all of the singularities are simple poles, even at the mode's cut-off frequency (corresponding to $\xi = 0$). The summation of the residues of these single poles leads to the two following equations for the displacement fields:

$$u_r^{s,a}(r,z) = -i\frac{\pi}{2\mu}\sum_{\xi_{s,a}} Pa\frac{J_1(\xi_{s,a}a)}{\xi_{s,a}}\xi_{s,a}\frac{\Gamma_m^s(\xi_{s,a})}{\Delta'_{s,a}(\xi_{s,a})}H_1^{(1)}(\xi_{s,a}r) \qquad r > a \qquad \text{(A.31a)}$$

$$u_z^{s,a}(r,z) = -i\frac{\pi}{2\mu}\sum_{\xi_{s,a}} Pa\frac{J_1(\xi_{s,a}a)}{\xi_{s,a}}\xi_{s,a}\frac{\Gamma_m^s(\xi_{s,a})}{\Delta'_{s,a}(\xi_{s,a})}H_0^{(1)}(\xi_{s,a}r) \qquad r > a \qquad \text{(A.31b)}$$

where ξ_s and ξ_a are the roots of the dispersion equations (A.19) and (A.20), respectively.

Arbitrary Pressure Distribution

Examining the solutions (A.31) reveals that the transform of the normal loading function, F^0, (equation (A.27)), remains unchanged in by the inverse Hankel transform. Building on this simple concept, Ditri (1993a) shows the solution may be generalized to any arbitrary pressure distribution, which vanishes

identically for r greater than some value a^* by replacing $-PaJ_1(\xi a)/\xi$ by the zero order Hankel transform of the given pressure distribution, $F^0(\xi)$. For example, for a parabolic normal pressure distribution defined by,

$$f(r) = \begin{cases} -P\left[1-(r/a)^2\right], & r < a \\ 0, & r > a \end{cases} \tag{A.33a}$$

and

$$g(r) \equiv 0 \tag{A.33b}$$

the zero order Hankel transform is given by,

$$F^0_{para} = -2P\frac{J_2(\xi a)}{\xi^2} \tag{A.34a}$$

and

$$G^1_{para} \equiv 0 \tag{A.34b}$$

Appendix B

Summary of Final Functions and Symbols
Used in the Time-Harmonic Solution

This appendix lists the equations that are needed to obtain a numerical solution to the time-harmonic problem:

$$u_r^{s,a}(r,z) = i\frac{\pi}{2\mu}\sum_{\xi_{s,a}} F^0(\xi_{s,a},a)\xi_{s,a}\frac{\Gamma_{rn}^s(\xi_{s,a})}{\Delta_{s,a}'(\xi_{s,a})}H_1^{(1)}(\xi_{s,a}r) \qquad r>a \tag{A.31a}$$

$$u_z^{s,a}(r,z) = -i\frac{\pi}{2\mu}\sum_{\xi_{s,a}} F^0(\xi_{s,a},a)\xi_{s,a}\frac{\Gamma_{zn}^s(\xi_{s,a})}{\Delta_{s,a}'(\xi_{s,a})}H_0^{(1)}(\xi_{s,a}r) \qquad r>a \tag{A.31b}$$

where,

$$\Gamma_{rt}^s(k_{tl},k_{ts},\xi) = -k_{ts}\left[2\xi^2\cos(k_{ts}\,d/2)\cos(k_{tl}z)+\left(k_{ts}^2-\xi^2\right)\cos(k_{tl}\,d/2)\cos(k_{ts}z)\right] \tag{B.1}$$

$$\Gamma_{rn}^s(k_{tl},k_{ts},\xi) = \xi\left[-2k_{tl}k_{ts}\sin(k_{tl}\,d/2)\cos(k_{ts}z)+\left(k_{ts}^2-\xi^2\right)\sin(k_{ts}\,d/2)\cos(k_{tl}z)\right] \tag{B.2}$$

$$\Gamma_{zt}^s(k_{tl},k_{ts},\xi) = \xi\left[2k_{tl}k_{ts}\cos(k_{ts}\,d/2)\sin(k_{tl}z)+\left(k_{ts}^2-\xi^2\right)\cos(k_{tl}\,d/2)\sin(k_{ts}z)\right] \tag{B.3}$$

$$\Gamma_{zn}^s(k_{tl},k_{ts},\xi) = k_{tl}\left[2\xi^2\sin(k_{ts}\,d/2)\sin(k_{tl}z)+\left(k_{ts}^2-\xi^2\right)\sin(k_{ts}\,d/2)\sin(k_{tl}z)\right] \tag{B.4}$$

$$\Gamma_{rt}^a(k_{tl},k_{ts},\xi) = k_{ts}\left[2\xi^2\sin(k_{ts}\,d/2)\sin(k_{tl}z)+\left(k_{ts}^2-\xi^2\right)\sin(k_{tl}\,d/2)\sin(k_{ts}z)\right] \tag{B.5}$$

$$\Gamma_{rn}^a(k_{tl},k_{ts},\xi) = \xi\left[-2k_{tl}k_{ts}\cos(k_{tl}\,d/2)\sin(k_{ts}z)+\left(k_{ts}^2-\xi^2\right)\cos(k_{ts}\,d/2)\sin(k_{tl}z)\right] \tag{B.6}$$

$$\Gamma_{zt}^a(k_{tl},k_{ts},\xi) = \xi\left[-2k_{tl}k_{ts}\sin(k_{ts}\,d/2)\cos(k_{tl}z)+\left(k_{ts}^2-\xi^2\right)\sin(k_{tl}\,d/2)\cos(k_{ts}z)\right] \tag{B.7}$$

$$\Gamma_{zn}^s(k_{tl},k_{ts},\xi) = -k_{tl}\left[2\xi^2\cos(k_{tl}\,d/2)\cos(k_{ts}z)+\left(k_{ts}^2-\xi^2\right)\cos(k_{ts}\,d/2)\cos(k_{tl}z)\right] \tag{B.8}$$

$$\Delta_s \equiv \left(k_{ts}^2-\xi^2\right)^2\cos(k_{tl}\,d/2)\sin(k_{ts}\,d/2)+4\xi^2k_{tl}k_{ts}\sin(k_{tl}\,d/2)\cos(k_{ts}\,d/2) \tag{A.19}$$

$$\Delta_a \equiv \left(k_{ts}^2-\xi^2\right)^2\sin(k_{tl}\,d/2)\cos(k_{ts}\,d/2)+4\xi^2k_{tl}k_{ts}\cos(k_{tl}\,d/2)\sin(k_{ts}\,d/2) \tag{A.20}$$

$$F_{pist}^0(\xi) = -Pa\frac{J_1(\xi a)}{\xi} \tag{A.27a}$$

$$F_{para}^0(\xi) = -2P\frac{J_2(\xi a)}{\xi^2} \tag{A.34a}$$

List of Symbols Used in Time-Harmonic Solution

Symbol	Name	Defining Relation
$\mathcal{A}$	Coefficient Matrix used to satisfy boundary conditions	
$A(\xi)$	Amplitude for the symmetric part of the scalar Helmholtz potential, ϕ	
a	Transducer radius (finite circular region over which tractions are applied)	
$B(\xi)$	Amplitude for the anti-symmetric part of the scalar Helmholtz potential, ϕ	
$b(r)$, $B^n(\xi)$	Arbitrary function in r, and its Hankel transform of order n	
$C(\xi)$	Amplitude for the symmetric part of the vector Helmholtz potential, ψ	
c_L	Longitudinal bulk wave speed	$\left(\frac{\lambda+2\mu}{\rho}\right)^{1/2}$
c_T	Shear bulk wave speed	$\left(\frac{\mu}{\rho}\right)^{1/2}$
$D(\xi)$	Amplitude for the anti-symmetric part of the vector Helmholtz potential, ψ	
d	Plate thickness	
$f(r)$, $F^0(\xi)$	Radially axisymmetric normal traction distribution and its zero order Hankel transform	
$g(r)$, $G^0(\xi)$	Radially axisymmetric transverse traction distribution and its first order Hankel transform	
$H_n^{(1)}$	Hankel function of the first kind of order n	
$\mathbf{I}$	Identity Dyadic	
I_1, I_2	Integrals of odd and even functions in ξ	
J_n	Bessel function of order n	
$\mathcal{H}_n\{g(r)\}$	Hankel transform of order n of the function $g(r)$	$\int_0^\infty r g(r) J_n(\xi r) dr$
$\mathcal{H}_n^{-1}\{G^n(\xi)\}$	Inverse Hankel transform of order n of the transformed function $G^n(\xi)$	$\int_0^\infty \xi G^n(\xi) J_n(\xi r) d\xi$

Symbol	Name	Defining Relation
k_L	Longitudinal wavenumber	ω/c_L
k_T	Transverse wavenumber	ω/c_T
k_{tl}	Longitudinal wavenumber	$\sqrt{\left(\omega/c_L\right)^2 - \xi^2}$
k_{ts}	Transverse wavenumber	$\sqrt{\left(\omega/c_T\right)^2 - \xi^2}$
P	Maximum pressure/per area applied by the transducer on the plate	
$\mathbf{r}$	Position vector in space	$\mathbf{r} = \hat{r}r + \hat{\theta}\theta + \hat{z}z$
r	Radial distance in the x-y plane away from the center of the source	
t	Time variable	
$\mathbf{u}(\mathbf{r},t)$	Particle displacement field	$\rho\frac{\partial^2\mathbf{u}}{\partial t^2} = \nabla\cdot\boldsymbol{\sigma}$
$u_{r,z}^{s,a}$	Symmetric and anti-symmetric components of the in-plane and out-of-plane displacements	Eqn. (A.31)
z	Coordinate perpendicular to the plane of the plate. ($z = 0$ corresponds to the mid-plane of the plate)	
$\Gamma_{\alpha\beta}^{s,a}$	Coefficent functions	Eqn. (B.1)-(B.8)
Δ_s, Δ_s'	Dispersion function for straight crested symmetric Lamb waves in free layer	Eqn. (A.19)
Δ_a, Δ_a'	Dispersion function for straight crested anti-symmetric Lamb waves in free layer	Eqn. (A.20)
θ	Angle to the point $\mathbf{r}$ from the x axis in the x-y plane	
λ, μ	Lamé's constants	
χ_1, χ_2	Odd and even functions in ξ	
ξ	Wavenumber	
$\xi_{s,a}$	Roots of the Rayleigh-Lamb Dispersion Equations (A.19) and (A20)	

Symbol	Name	Defining Relation
ρ	Mass density	
$\boldsymbol{\sigma}$	Stress Dyadic	Hooke's Law $\boldsymbol{\sigma} = \lambda \mathbf{I} \nabla \cdot \mathbf{u} + \mu(\nabla \mathbf{u} + \mathbf{u} \nabla)$
$\sigma_{\theta z}$	Shear stress component perpendicular to the angular unit vector, $\hat{\theta}$, acting in the 'z' direction	
σ_{rz} , Σ^1_{rz}	Shear stress component perpendicular to the radial unit vector, acting in the 'z' direction and its Hankel transform	
σ_{zz}, Σ^0_{zz}	Normal stress component in the 'z' direction and its Hankel transform	
ϕ	Helmholtz scalar potential	$\mathbf{u} = \nabla\phi + \nabla \times \Psi, \quad \nabla \cdot \Psi = 0$
$\phi^{s,a}$	Symmetric and anti-symmetric parts of the Helmholtz scalar potential	
$\boldsymbol{\Psi}$	Helmholtz vector potential	$\mathbf{u} = \nabla\phi + \nabla \times \Psi, \quad \nabla \cdot \Psi = 0$
Ψ, Ψ_z	'z' component of the Helmholtz vector potential	
$\Psi^{s,a}$	Symmetric and anti-symmetric parts of the 'z' component of the Helmholtz vector potential	
ω	Circular frequency	

References

Abramowitz, M. and Stegun, I.A., *Handbook of Mathematical Functions with Formulas, Graphs, and Mathematical Tables*, New York: Dover Publications Inc. (1972).

Alleyne, D.N. and Cawley, P., "The Interaction of Lamb Waves with Defects," *IEEE Transactions on Ultrasonics, Ferroelectrics, and Frequency Control*, Vol. 39, no. 3, pp. 381-397, May (1992).

Alleyne, D.N. and Cawley, P., "A Two-dimensional Fourier Transform Method for the Measurement of Propagating Multimode Signals," *J. Acoust. Soc. Amer.*, Vol. 89, pp. 1159-1168, (1991).

Auld, B.A., *Acoustic Fields and Waves in Solids*, Vol. II, 2nd ed., Malabor, FL: Kreiger Publishing Co. (1990).

Bartos, A.L., "Acousto-Ultrasonic Pattern Analysis of Impact-Damaged Composite Panels," *Proceedings of the Second International Conference on Acousto-Ultrasonics*, June 24-25, (1993), Atlanta, GA, pp. 133-142. Alex Vary, Ed. ASNT, Columbus, OH.

Ditri, J.J., Pilarski, A., Rose, J.L., and Pavlakovic, B., "Generation of Guided Waves in a Plate by Axisymmetric Normal Surface Loading," Presented at QNDE Conference in Brunswick, Maine, August, (1993a). *To be published in the proceedings.*

Ditri, J.J. and Rose, J.L., "Excitation of Guided Waves in Generally Anisotropic Layers Using Finite Sources," *Journal of Applied Mechanics*, submitted (1993b).

Ditri, J.J., "Some Theoretical and Experimental Aspects of the Generation of Guided Elastic Waves using Finite Sources," Ph.D. Thesis, Drexel University, Philadelphia, PA, (1992).

Fulton, J. and Sneddon, I.N., "The Dynamical Stresses Produced in a Thick Plate by the Action of Surface Forces," *Proc. Glasg. Math. Assn.*, Vol. 3, pp. 153-163, (1958).

Graff, K.F., *Wave Motion in Elastic Solids*, New York: Dover Publications Inc. (1975).

Hilton, Y.L., "Application of Pattern Recognition Techniques to Acousto-Ultrasonic Testing of Kevlar™ Composite Panels," *Proceedings of the Second International Conference on Acousto-Ultrasonics*, June 24-25, (1993), Atlanta, GA, pp. 125-132. Alex Vary, Ed. ASNT, Columbus, OH.

Holden, A.N., "Longitudinal Modes of Elastic Waves in Isotropic Cylinders and Slabs," *Bell Systems Technical Journal*, Vol. 30, pp. 956-969, (1951).

Horne, M.R., and Duke, J.C., "Methods for Implementation of the AU Method / Approach," *Proceedings of the Second International Conference on*

Acousto-Ultrasonics, June 24-25, (1993), Atlanta, GA, pp. 13-20. Alex Vary, Ed. ASNT, Columbus, OH.

Kautz, H.E., and Lerch, B.A., "Preliminary Investigation of Acousto-Ultrasonic Evaluation of Metal-Matrix Composite Specimens," *Mater. Eval.*, Vol. 49, pp. 607-612, (1991).

Kautz, H.E., "Ultrasonic Evaluation of Mechanical Properties of Thick, Multilayered, Filament-Wound Composites," *Mater. Eval.*, Vol. 45, pp. 1401-1412, (1987).

Kolsky, H., *Stress Waves in Solids,* New York: Dover Publications Inc. (1963).

Lamb, H., "On the Flexure of an Elastic Plate," *Proc. Lond. Math. Soc.*, Vol. 21, pp. 70-90, (1889-1890).

Lamb, H., "On Waves in an Elastic Plate," *Proc. Roy. Soc. Lond. A*, Vol. 93, pp. 114-128, (1917).

Lyon, R.H., "Response of an Elastic Plate to Localized Driving Forces," *J. Acoust. Soc. Amer.*, Vol. 41, pp. 1449-52, (1955).

Meeker, T.R. and Meitzler, A.H., "Guided Wave Propagation in Elongated Cylinders and Plates," *Physical Acoustics*, 1, Part A, pp. 111-167, (1964).

Miklowitz, J., *Theory of Elastic Waves and Waveguides*, New York: North Holland Publishing Co. (1978).

Mindlin, R.D., "Waves and Vibrations in Isotropic, Elastic Plates." New York: Pergamon Press, (1960) pp. 199-232. reprinted in Deresiewicz, H., et al., eds., *The Collected Papers of Raymond D. Mindlin* Vol. 1. New York: Springer-Verlag, 1971. pp. 425-457.

Mindlin, R.D., *An Introduction to the Mathematical Theory of Vibrations of Elastic Plates,* Fort Monmouth, NJ: U. S. Army Signal Corps Engineering Laboratories, (1955).

Mindlin, R.D., "Thickness-Shear and Flexural Vibrations of Crystal Plates," *J. Appl. Phys.*, no. 22, p. 316, (1951).

Nikiforov, L.A. and Kharitonov, A.V., "Parameters of Longitudinal Subsurface Waves Excited by Angle Beam Transducers." *Defektoskopiya*, Vol. 6, pp. 80-85, June (1981).

Onoe, M, "A Study of the Branches of the Velocity-Dispersion Equations of Elastic Plates and Rods," Report of Joint Committee on Ultrasonics of The Institute of Electrical Communications Engineers and the Acoustical Society of Japan, (1955).

Pilarski, A., Ditri, J. J., Rose, J.L., "Remarks on symmetric Lamb waves with dominate longitudinal displacements," *J. Acoust. Soc. Amer.*, Vol. 93, no. 4, Pt. 1, pp. 2228-2230, April (1993).

Pursey, H., "The Launching and Propagation of Elastic Waves in a Plates," *Quarterly Journal of Mechanics and Applied Mechanics*, Vol. X, no. 1, pp. 45-62, (1957).

Rayleigh, Lord, "On the Free Vibrations of an Infinite Plate of Homogeneous Isotropic Elastic Matter," *Proc. London Math. Soc.*, Vol. 20, pp. 225-234, (1889-1889).

Reis, H., "Nondestructive Evaluation of Porosity in Polymer Matrix Composites," *Proceedings of the Second International Conference on Acousto-Ultrasonics*, June 24-25, (1993), Atlanta, GA, pp. 107-116. Alex Vary, Ed. ASNT, Columbus, OH.

Rokhlin, S.I., "Lamb Wave Interaction with Lap-Shear Adhesive Joints: Theory and Experiment," *J. Acoust. Soc. Amer.*, Vol. 89, no. 6, pp. 2758-2765, (1991).

Rose, J.L., Rajana., K., Pilarski, A., "Ultrasonic Guided Waves for NDE of Adhesively Bonded Joints in Aging Aircraft," *Proceedings of Adhesion Society Meeting*, Orlando, FL, Feb. 20-24, (1994).

Rose, J.L., Ditri, J.J., Pilarski, A., "Source Influences on the Excitation of Guided Waves in Anisotropic Layers," *Proceedings of the ICCM/9* - Madrid, Spain 12-16 July, (1993a), Vol. 6, pp. 811-818.

Rose, J.L., Ditri, J.J., Pilarski, A., "Wave Mechanics Principles in Acousto-Ultrasonic NDE." *Proceedings of the Second International Conference on Acousto-Ultrasonics*, June 24-25, (1993b), Atlanta, GA, pp. 21-28. Alex Vary, Ed. ASNT, Columbus, OH.

Scott, R.A., and Miklowitz, J., "Transient Non-axisymmetric Wave Propagation in an Infinite Isotropic Elastic Plate," *Int. J. Solids Structures*, Vol. 5, pp. 65-79, (1969).

Tang, B., and Henneke, E.G., "Lamb-Wave Monitoring of Axial Stiffness Reduction of Laminated Composite Plates," *Mater. Eval.*, Vol. 47, pp. 928-934.

Thomsen, J.J., and Lund, K., "Quality Control of Composite Materials by Neural Network Analysis of Ultrasonic Power Spectra," *Mater. Eval.*, Vol. 49, pp. 594-600, (1991).

Vary, A., "Acousto-Ultrasonics. An update." ASTM Special Technical Publications n. 1077, pp. 95-104, (1991).

Vary, A., "Review of Acousto-Ultrasonics NDE for Composites," *NASA Conference Publication* n. 3091, p. 33, (1990).

Viktorov, I.A., *Rayleigh and Lamb Waves, Physical Theory and Applications*, New York: Plenum Press, (1967).

REPORT DOCUMENTATION PAGE

Form Approved
OMB No. 0704-0188

1. AGENCY USE ONLY (*Leave blank*)	2. REPORT DATE	3. REPORT TYPE AND DATES COVERED
	August 1994	Final Contractor Report

4. TITLE AND SUBTITLE
The Influence of Finite-Size Sources in Acousto-Ultrasonics

5. FUNDING NUMBERS
WU–505–90–51
C–NAG3–1365

6. AUTHOR(S)
Brian N. Pavlakovic and Joseph L. Rose

7. PERFORMING ORGANIZATION NAME(S) AND ADDRESS(ES)
The Pennsylvania State University
Department of Engineering Science and Mechanics
114 Hallowel Building
University Park, Pennsylvania

8. PERFORMING ORGANIZATION REPORT NUMBER
E–9061

9. SPONSORING/MONITORING AGENCY NAME(S) AND ADDRESS(ES)
National Aeronautics and Space Administration
Lewis Research Center
Cleveland, Ohio 44135–3191

10. SPONSORING/MONITORING AGENCY REPORT NUMBER
NASA CR–195374

11. SUPPLEMENTARY NOTES
Project Manager Alex Vary, Structures Division, Lewis Research Center, organization code 5250, (216) 433-6019.

12a. DISTRIBUTION/AVAILABILITY STATEMENT
Unclassified - Unlimited
Subject Category 38

12b. DISTRIBUTION CODE

13. ABSTRACT ***(Maximum 200 words)***

This work explores the effects that the *finite* normal axisymmetric traction loading of an infinite isotropic plate have on wave propagation in Acousto-Ultrasonics (AU), in which guided waves are created using two normal incidence transducers. Although the work also addresses the effects of the transducer pressure distribution and pulse shape, this thesis concentrates on two main questions: how does the transducer's diameter control the phase velocity and frequency spectrum of the response?, and how does the plate thickness relate to the plate's excitability? The mathematics of the time-harmonic solution and the physical principles and the practical considerations for AU wave generation are explained. Transient sources are modeled by the linear superposition of the time-harmonic solutions found using the Hankel transform and they are then compared to experimental data to provide insight into the relation between the size of the transducer and the preferred phase velocity.

14. SUBJECT TERMS
Nondestructive testing (NDT); Nondestructive evaluation (NDE); Ultrasonics; Plate waves; Lamb waves; Composites

15. NUMBER OF PAGES
107

16. PRICE CODE
A06

17. SECURITY CLASSIFICATION OF REPORT	18. SECURITY CLASSIFICATION OF THIS PAGE	19. SECURITY CLASSIFICATION OF ABSTRACT	20. LIMITATION OF ABSTRACT
Unclassified	Unclassified	Unclassified	